Chem Soc Rev

Long phosphorescent phosphors: From fundamentals to applications

Journal:	*Chemical Society Reviews*
Manuscript ID	CS-SYN-07-2015-000582.R2
Article Type:	Review Article
Date Submitted by the Author:	15-Jan-2016
Complete List of Authors:	Li, Yang; State Key Laboratory of Luminescent Materials and Devices, Institute of Optical Communication Materials, South China University of Technology, Gecevicius, Mindaugas; State Key Laboratory of Luminescent Materials and Devices, Institute of Optical Communication Materials, South China University of Technology, Qiu, Jianrong; South China University of Technology,

Long persistent phosphors

----from fundamentals to applications

Yang Li[1,2], Mindaugas Gecevicius[1], Jianrong Qiu[1,*]

[1] State Key Laboratory of Luminescent Materials and Devices, School of Materials Science and Technology, South China University of Technology, Guangzhou, China

[2] School of Chemistry and Chemical Engineering, South China University of Technology, Guangzhou, China

*corresponding author: qjr@scut.edu.cn; msliyang@scut.edu.cn

Abstract

Due to the unique mechanism of photoelectron storage and release, long persistent phosphorescence, also called long persistent luminescence or long lasting afterglow/phosphorescence plays a pivotal role in the areas of spectroscopy, photochemistry, photonics and materials science. In recent years, more researches have focused on the manipulation of morphology, operational wavebands and persistent duration of long persistent phosphors (LPPs). These desired achievements stimulated the growing interests of designing bio-labels, photocatalysts, optical sensors, detectors and photonic devices. In this review, we present a multidisciplinary research on synthetic methods, afterglow mechanisms, characterization techniques, materials system, and applications of LPPs. At first we introduce the recent developments in LPPs for the synthesis of nanoparticles from the aspects of particle sizes, monodispersity and homogeneity based on the urgent application of bio-imaging. In the later sections, we present the possible mechanisms, which involve the variation of trap distribution during the trapping and de-trapping process, complicated photo-ionization reaction of trap site levels and impurity centers together with their corresponding migration kinetics of carriers. Meanwhile, we emphasize on the characterization techniques of defects, used to qualitatively or quantitatively describe the types, concentrations and depths of the traps. This review article also highlights the recent advances in suggested LPPs materials with focus on the LPPs' hosts and optically active centers as well as their control, tuning and intrinsic links. We further discuss the classification of LPPs based on the different emission and excitation wavebands from ultraviolet to near-infrared region along with an overview of activation mode of afterglow. Afterwards, we provide an exhibition of new products towards diverse application fields including solar energy utilization, bio-imaging and diagnosis, and photocatalysts. Finally, we summarize the current achievements, and discuss the problems and suggestions for potential future directions in the aforementioned parts.

1. Introduction

Long phosphorescent phosphors/long persistent phosphors (LPPs) continuously stimulate the extensive research interest of materials scientists, chemists, physicists, even biologists because of their mysterious optical phenomenon and the wide spread application. Especially after recent decades of development, the applications of LPPs have spread from the initial civil use i.e. decoration, safety displays, dials, *etc*. to a wide range of advanced scientific application fields such as life sciences, biomedicine, clinical medicine, energy and environmental engineering.[1-49] The corresponding overwhelming contributions have been made to the development of near-infrared (NIR) LPPs or nano-scale LPPs, with the advent of new material system, design methodology as well as synthesizing and functionalization route. Furthermore, physicists have proposed many theoretical and experimental models to understand the trapping-detrapping process along with the capture, migration and release kinetics of charge carriers.[11, 50-73] Up to now, the related researches have made great progress, thus we think it is just the right time to provide this review for further stimulating the motivation of developing novel LPPs and opening up new applications of LPPs.

In this review article, we focus on the recent progress in the aspects of synthetic techniques, characterizations, afterglow mechanisms, applications and new materials of LPPs with emphasis specifically on:

(1) **Afterglow mechanisms**. Long persistent phosphorescence (LPP) is a phenomenon in which a material emits in the ultraviolet (UV), visible (VIS) or NIR spectral regions for minutes, hours or even days after ceasing the excitation irradiation. Sometimes it is simply called as afterglow. Relatively long fluorescent lifetime (millisecond to second magnitude) of inorganic luminescent materials is due to the forbidden transitions within the luminescent–center, while the long phosphorescent duration of organic compounds is related to the triplet-to-singlet transitions. The mechanism of LPP is different from that of fluorescence and phosphorescence. LPP can be divided into four parts: (a) **Excitation of charged carriers**. Upon effective optical charging (UV, VIS or NIR light), electronic implantation (electron beam) or high-energy-ray irradiation (X-ray, beta ray or gamma radiation *etc*.), charge carriers (electrons or holes) are generated, with the delocalization and migration of charge carriers; (b) **Storage of charged carriers**. The excited carriers are firmly captured on the trapping states, while the storage capacity of trapping states strongly depend on the types and numbers of carriers and defects; (c) **Release of charged carriers**. Captured carriers escape from the traps. In addition to the depths of traps in hosts, releasing rate of carriers captured in traps also can be influenced by the disturbance in the external fields (thermal, optical or mechanical disturbance), giving a control of persistent duration; (d) **Recombination process of charged carriers**.

Though charge carrier traps play a crucial role in all the suggested afterglow mechanisms, there is still no universal way to describe the properties of traps for a given persistent phosphor. Main features of trap types (whether the defects effectively participate in the captured process of charge carrier), concentrations (the number of effective traps), and depths (the releasing rate of the carriers captured by the traps) should be considered. Various in-depth research of afterglow mechanisms including hole model, electron model, energy band gap model and quantum tunneling model have been commenced with a special focus on the types of charge carrier, the possible valence variation of dopants and co-dopants as well as the routes of electronic migration.

(2) **Defects characterizations**. To assist in precisely describing the trap properties and modeling the afterglow mechanism, we discuss the importance of defects characterization technique and the relevant frontier research fields. These techniques are believed to offer the supplement and improvement for the older afterglow mode even access the possibility to build new and generally accepted afterglow model, for example, electron spin resonance are used to probe the species of traps, not only referring to the attribution of electron/hole traps, nut also indicating what these traps are. The newly proposed multidisciplinary measurements also include photoconduction (used to detect the species of traps as well as excitation, migration, and release kinetics of carriers), positron annihilation lifetime spectroscopy (used to calculate the concentration of traps), X-ray absorption spectroscopy (used to identify whether valence variation of dopants

occurs during trapping and detrapping process, also referring to the excitation, migration, and release kinetics of carriers), and thermoluminescence and its excitation spectra (used to calculate the depth of traps, then potentially getting the releasing rate of the carriers). In fact, prior to defects characterization, it is also necessary to carry out the spectroscopic and structural measurements, which are also proved to be able to get more qualitative and quantitative information of host, activators and defects.

(3) **Applications**. Initially, this phenomenon is concentrated on the application of displays and safety signage. Shortly afterwards, other applications of optical storage, sensor and detector are proposed towards the utilization of the characteristic of trapping-storage-releasing. Past few years, the development of optical bio-imaging proposed LPPs as the new generation bio-labels to take full advantage of their distinctive features of low auto fluorescence, high signal-to-noise ratio, and deep tissue penetration in cells, tissues and other complex systems. In addition to optical imaging, LPPs also have been found to be applied in diverse bioassays, drug delivery and therapy. Other in-depth investigations on LPPs are necessary to be conducted for their potential applications in high performance photocatalysis and photonic devices by embedding LPPs into the intrinsical system and realizing the functional scheme.

(4) **Synthetic techniques**. New applications spontaneously set more requirements on design-methodology, morphology and functionalization of LPPs. To satisfactorily meet these demands, more and more synthetic routes are suggested to prepare small-size, homogeneous and persistent phosphorescent nanomaterials. In this part, we outline the proposed synthesis routes of nanoparticles with LPP. Substantial progresses have been made from 2009 to now, for their size/morphology/homogeneity control, functionalization design, as well as afterglow property optimization. This emerging research trend follows two main directions: wet-chemical reaction including sol-gel procedure, combustion synthesis, hydro(solvo)thermal route, coprecipitation, microwave synthesis, template method *etc.*, and physical route (i.e. laser ablation and electron beam process *etc.*).

(5) **New materials**. New applications also promote the development of new materials. On the one hand, the researches pay close attention to synthesize new LPPs with the different activators, hosts and emission/excitation bands (UV-VIS-NIR) to meet the practical demands. On the other hand, the researches do their best to define the fundamental design-methodology of LPPs from the aspects of coordination configuration, band theory, and redox, *etc*. In this review, the reported LPPs exhibit the violet-to-red range and even near-infrared emission wavebands, which can be excited by a wide range of excitation source, ranging from high energy rays, to UV-VIS-NIR light. Notably, long-wavelength-emitting LPPs become the interesting newcomers to the world of LPPs. Referred strategies of extending the emission wavebands to biological tissue window include varying the activators, modulating the crystal field and transferring the persistent energy from one activator to another. In addition, we also review here recent progress of hosts and activators of LPPs. The involving hosts correspond to oxides (aluminates, silicates, stannates, phosphates, gallates, germinates *etc*.), non-oxides (sulfides, nitrides *etc*.), and organic carbons nanostructure, while the activators refer to rare earth ions (Eu, Ce, Pr, Sm, Tb, Dy, Tm, Yb), transition metal ions (Cr, Mn, *etc*.) and main group elements (Bi, *etc.*). Furthermore, the concept of VIS-NIR light excitation involving the different excitation mode is proposed to better meet the unique needs of *in vivo* imaging.

(6) **Perspectives**. At the end of this review, we discuss the main challenges, the research directions into the origin of the unique optical phenomenon, and provide the systematic perspectives of the plausible design methodology.

In the beginning, we give a brief discussion on the history of LPPs. This unique phenomenon of LPPs has been known for nearly a thousand years. The main development of LPPs may be divided into 4 stages.

(1) In some ancient Chinese legends, the paintings or so called “luminous pearl” were found the lasting visible light during the night by mixing the colors with a special kind of pearl shell. The first well-documented description about LPP could be traced back to the beginning of the 17^{th} century. LPP certainly became the best documented kind of luminescence because of the discovery of the famous Bologna Stone. It was finally speculated that a lot of different impurities played an important role during the persistent emission and the host materials were barium sulfide, not barium sulfate. Fortunius demonstrated the responsibility of natural

impurities for the long persistent duration in barium sulfide.[74]

(2) After the discovery of BaS, researches of LPPs were concentrated on the sulfides, but only few reports were available. At the end of the 20th century, a series of different sulfide materials, such as ZnS: Cu or Co, were reported. The first commercial applications came with ZnS: Cu about 100 years ago. The emission was modified with the partial substitution of Zn with Cd. Similar materials CaS: Eu (Ca, Sr)S: Bi *etc.* appeared later. They were applied in safety signage, dials, displays and decoration. However, LPP of these materials was too weak and short to satisfactorily meet the demand of practical purposes. Their utility was also hampered by their extreme sensitivity to moisture.[75, 76]

(3) The boom in the researches and applications of LPPs came in mid 1990s with the introduction of efficient Eu^{2+}, R^{3+} co-doped aluminates–$CaAl_2O_4$: Eu^{2+}, Nd^{3+} and $SrAl_2O_4$: Eu^{2+}, Dy^{3+} emitting in the blue and green, respectively. Matsuzawa *et al.* discovered the green-emitting phosphor $SrAl_2O_4$: Eu^{2+}, Dy^{3+}. By co-doping Dy^{3+}, the green LPPs demonstrated a far higher initial intensity and a much longer lifetime (hours after ceasing the excitation) compared to the commercially used ZnS: Cu, Co (Victor first showed the long-lasting afterglow of Eu^{2+} singly doped $SrAl_2O_4$ LPPs in 1971). Today, different hosts (aluminates, silicates, stannate, *etc.*) and activators (Tb^{3+}, Mn^{2+}, *etc.*) have been proposed to enrich the family of green LPPs. Meanwhile, each of the main colors of blue, green, and red are also developed to fulfill the requirements of practical purposes except NIR LPP. The number of NIR LPPs was still low, limiting their applications in some advanced application fields, such as night-vision surveillance or *in vivo* medical imaging.[77]

(4) Now there is an increasing interest in the use of NIR LPP in the biologically transparent window to drive the photonic bio-labels for tracing the cancer cells, since the long emission lifetime of LPPs can effectively increase signal-to-noise ratio and decrease photon-induced deterioration of analytes. In 2012, Pan *et al*. published an article that paved path-breaking directions in this field by using gallates as the system, thereby realizing the super-long NIR afterglow-emission of 360 h in $Zn_3Ga_2Ge_2O_{10}$: Cr^{3+} phosphor, and firmly establishing an extra edge in the choice of gallates as the preferred material system for the fabrication of Cr^{3+}-activated NIR LPPs. This shockwave encouraged researchers to turn their attention to the research for remarkable NIR LPPs with different host (stannates, *etc*.) and activators (Bi^{2+}, Yb^{3+}, Mn^{4+}, *etc*.), as well as the nanocrystallization, functionalization and biotechnological application of NIR LPPs.[78-80]

2. Synthesis Methods

Synthesis method of LPPs plays a significant role in determining the features of microstructure, afterglow properties, fluorescent quantum efficiency and the distribution of defects. It is also strongly associated with the field of LPPs application. Conventional method to synthesize LPPs is a solid-state reaction, during which powdered raw materials are considered as the starting materials. Due to their relatively rough grains, these phosphors require high sintering temperature to obtain the LPP with designed compositions, but high sintering temperature can lead to a heterogeneous distribution and larger size of crystalline grain. In recent years, there is an increasing interest in the use of LPPs as the bio-labels and photocatalysts. These applications require high homogeneity, monodispersity and small clusters size of LPPs. Conventional synthesis conditions seemingly propose a conflict between the optimized morphology and afterglow time, i.e. a high synthesis temperature is beneficial to improve the persistent duration, but lead to the agglomerated products with irregular morphologies.[81, 82]

The emerging research trend of high-quality nanoparticles with controlled crystalline phases, shapes, and sizes as well as long persistent duration follows two main directions:

(1) First, synthesizing the nano-materials and then activating the LPP;

(2) First, preparing the LPPs and then improving the morphology and particle size.

For the first direction, the common routes correspond to many wet chemical methods, including sol-gel procedure, combustion synthesis, hydro(solvo) thermal route, coprecipitation, microwave synthesis and template method, *etc.* As a final step, post-treatment temperature can be raised until the appearance of size limitation and the collapse of nanostructure. In contrast, some researchers suggest another distinctive way of preparing nanoparticles with persistent phosphorescence (NPPs) via the laser ablation method. By choosing

the correct parameters of laser source (wavelength, repetition rate, peak power, intensity, irradiation time *etc.*), it is possible to obtain the desired nanoparticles with different morphology and size.

Table 1 gives a comparison of synthesis methods in terms of particle size, required temperature, homogeneity, morphology, and afterglow time. Although significant progress has been achieved, it is still a challenge to improve the monodispersity and size distribution undergoing a high synthesis temperature. Here we give a systematic discussion on the influence of different synthesis methods on afterglow properties and morphology of NPPs.

Table 1. Comparison of synthesis methods of LPPs in terms of the particle size, homogeneity, morphology control, synthesis temperature, and afterglow time.

Synthesis methods	Particle size	Homogeneity	Morphology	Synthesis temperatures (° C)	Afterglow time	Reference
Solid-solid reaction	Micrometer-scale	Bad	Bad	>1000	Long	83, 84
Sol-gel method	Nano to micrometer-scale	Medium	Bad	≤1000	Medium	2, 85
Combustion method	Nano to micrometer-scale	Medium	Medium	>1000	Short	86, 87
Hydrothermal method	Nano to micrometer-scale	Good	Medium	<1000	Short	11, 29
Co-precipitation	Nano to micrometer-scale	Good	Medium	>1000	Short	16
Template method	Nano to micrometer-scale	Good	Good	<1000	Short	56, 88
Electrospinning	Nano to micrometer-scale	Medium	Medium	>1000	Short	89
Laser technique	Nano to micrometer-scale	Medium	Medium	none	Medium	90
Electron beam irradiation	Nano to micrometer-scale	Medium	Medium	none	Medium	91

2.1 Solid-state reaction

Solid-solid reaction, which occurs between powders in the solid state, has been the most widely used approach for the preparation of LPPs including oxides, (oxy)sulfide and (oxy)nitrides, because it is comparatively simple, very suitable for mass production, and easy to obtain a long persistent duration. In fact, high temperature sintering is the essential for activating the afterglow, because a higher sintering temperature can generally increase the population of intrinsic thermal defects. These lattice defects and distortions corresponding to cation vacancy, anion vacancy, interstitial *etc.* (i.e. Schottky imperfections, Anti-Schottky imperfections and Frenkel imperfections *etc.* of the point defects), could improve the afterglow properties. Though solid-state method has many advantages in synthesizing the LLPs with remarkable afterglow property, it still has the inevitable shortcoming. The grain size of phosphor powders prepared by this method is several tens of micrometers. High calcination temperature leads to a poor homogeneity and morphology control. These disadvantages have greatly limited the development and application of nano-scale LPPs in the area of biomedicine, bioscience, energy engineering and environmental sciences.[92, 93]

2.2 Chemical synthesis-Liquid phase reaction

2.2.1 Sol-gel method

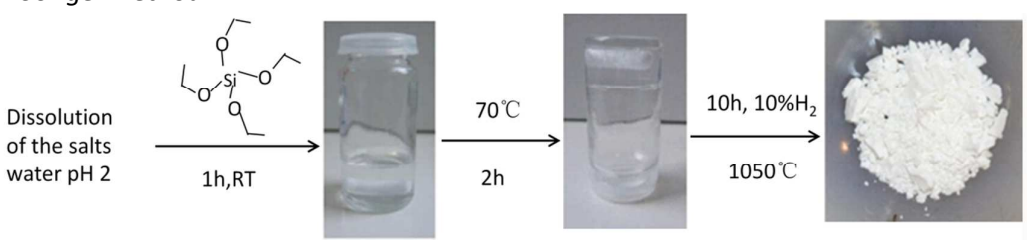

Fig. 1 Sol-Gel synthesis of persistent phosphorescent phosphors (reproduced with permission from ref. 85, copyright 2013, Proceedings of the National Academy of Sciences).

Sol-gel process has attracted much attention in synthesizing inorganic nanoparticles. The main procedures include sol-gel route (based on the hydrolysis and condensation of molecular precursors), gelation route (based on concentration of aqueous solutions containing metal-chelates) and polymerizable complex

route. Generally, this process uses metal salts or alkoxide as precursors, citric acid as a chelating ligand, and alcohol as a cross-linking agent to form a polymeric resin on the molecular level. Sol-gel technology is useful as the preferred preparation route of NPPs, since it requires a heat treatment. During this process small nanocrystallines are packed into the discrete space offered by complexing agent, thereby limiting the growth of nanocrystallines under a higher synthesis temperature, which is beneficial to improve the afterglow property. Much attention has been directed to the inorganic-salt-based sol-gel approach in aluminate and silicate-based phosphorescent materials.[94, 95] The representative syntheses process is illustrated in Fig. 1.

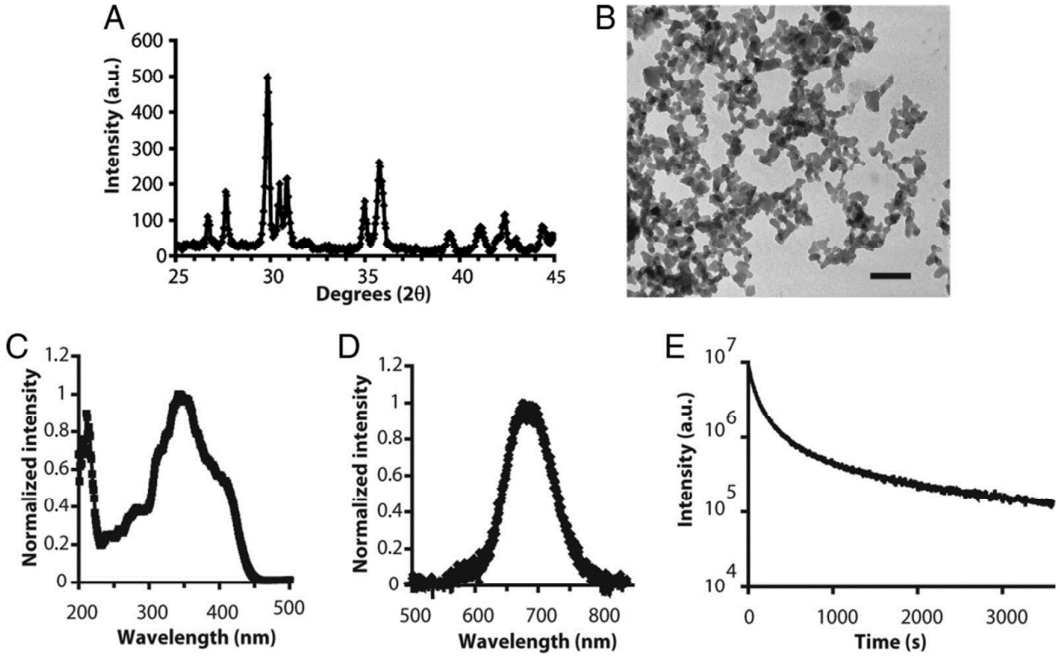

Fig. 2 Physical characteristics of long afterglow nanoparticles (A) NPPs showed a clinoenstatite-like structure. (B) Transmission electronic microscopy images of the synthesized NPPs. (Scale bar: 200 nm.) (C) Excitation spectrum. (D) Long afterglow emission spectrum. (E) Time dependence of the luminescence intensity of the NPPs. NPPs (10 mg) was put in 96-well plates under direct exposure to a 6-W UV lamp for 5 min. The luminous decay data were fit by a power law function for time >100 s (reproduced with permission from ref. 85, copyright 2007, Proceedings of the National Academy of Sciences).

Chermont *et al.* first proposed a bio-imaging method by using NIR NPPs, $Ca_{0.2}Zn_{0.9}Mg_{0.9}Si_2O_6$: Eu^{2+}, Dy^{3+}, Mn^{2+} prepared via sol-gel method as the bio-labels.[85] They chose chloride, nitrate, and tetraethoxysilane (TEOS) as the raw materials. All of the salts were dissolved in deionized water acidified at pH 2 by addition of concentrate nitric acid. Citric acid was then added rapidly as the complexant. Electronic microscopy analysis showed that the NPPs exhibit a quite narrow distribution in size, with particles diameter ranging from 50 to 200 nm (Fig. 2). Gradually, many publications about NPPs with different hosts (aluminate, silicate, oxysulfide, *etc*.) and activation centers prepared by sol-gel technique were reported, such as $Zn_3Ga_2Ge_3O_{10}$: Cr, Pr,[2] $ZnSiO_4$: Mn,[96] $CaMgSi_2O_6$: Mn,[97] *etc*. In addition to the size distribution, sol-gel method also provides an opportunity to control the morphology (nanosphere,[98] nanowire,[99] *etc.*) of as-prepared materials by varying the synthesis condition, including precursors, solvents, ligands, PH value, treatment temperature, *etc.* Fu *et al.* synthesized the $LiGa_5O_8$: Cr nanoparticles (NPPs) by a typical sol-gel method. They investigated the influence of synthesis temperature (700-800-900-1100 °C) on the morphology and size distribution of $LiGa_5O_8$: Cr nanoparticles, and demonstrated the distribution variation of particle size from 50 nm to 300 nm with the increase of synthesis temperature.[100]

To better inhibit the growth of nanocrystallites, some compositional approaches are proposed to develop NPPs, such as, sol-gel-microwave route,[101] sol-gel-combustion processing[102] and sol-gel-template technology (discussed on the part 2.2.5), *etc.* Red $Sr_3Al_2O_6$: Eu^{2+}, Dy^{3+} nanorods with width of about 80 nm were synthesized by using sol-gel-microwave method. The advantage of microwave irradiation is that it can effectively shorten the reaction time, accordingly decreasing the particle size. In sol-gel-combustion processing of synthesizing $SrAl_2O_4$: Eu^{2+}, Dy^{3+}, raw materials were dissolved in concentrated nitric acid. After the mixed

solution was heated (up to 90 °C), a little amount of ethanol was slowly dropped into the solution until no rufous gases (NO_2) evaporated out. Finally, spontaneous ignition occurred and underwent combustion with enormous swelling. Electronic microscopy analysis showed that the nanoparticles exhibit a size distribution with the diameter ranging from 90 to 250 nm.

2.2.2 Hydrothermal method

Hydrothermal synthesis refers to the preparation by chemical reaction of a substance in a sealed heated solution above ambient temperature and pressure. Different from sol-gel and co-precipitation methods, hydrothermal synthesis is usually carried out within specialized reaction vessels defined as autoclaves that are used to provide a high-pressure and sealed environment and thus to promote reactions between solid precursors. As a result, this approach enables the synthesis of high crystalline nanomaterials under relatively mild conditions when compared to other synthesis routes. Hydrothermal method is a promising method which can be better-controlled from the molecular precursor to the reaction parameters, such as the reaction time and temperature, to give highly homogeneous products. In a typical hydrothermal synthesis procedure for synthesizing NPPs, some organic additives and/or surfactants with specific functional groups like oleic acid OA, polyethylenimine (PEI), EDTA, and cetyltrimethylammonium bromide (CTAB) are generally added along with the reaction precursors to achieve simultaneous control over the crystalline phases, sizes and morphologies. Finally, a high treat temperature is indispensable to form the target NPPs.[103, 104]

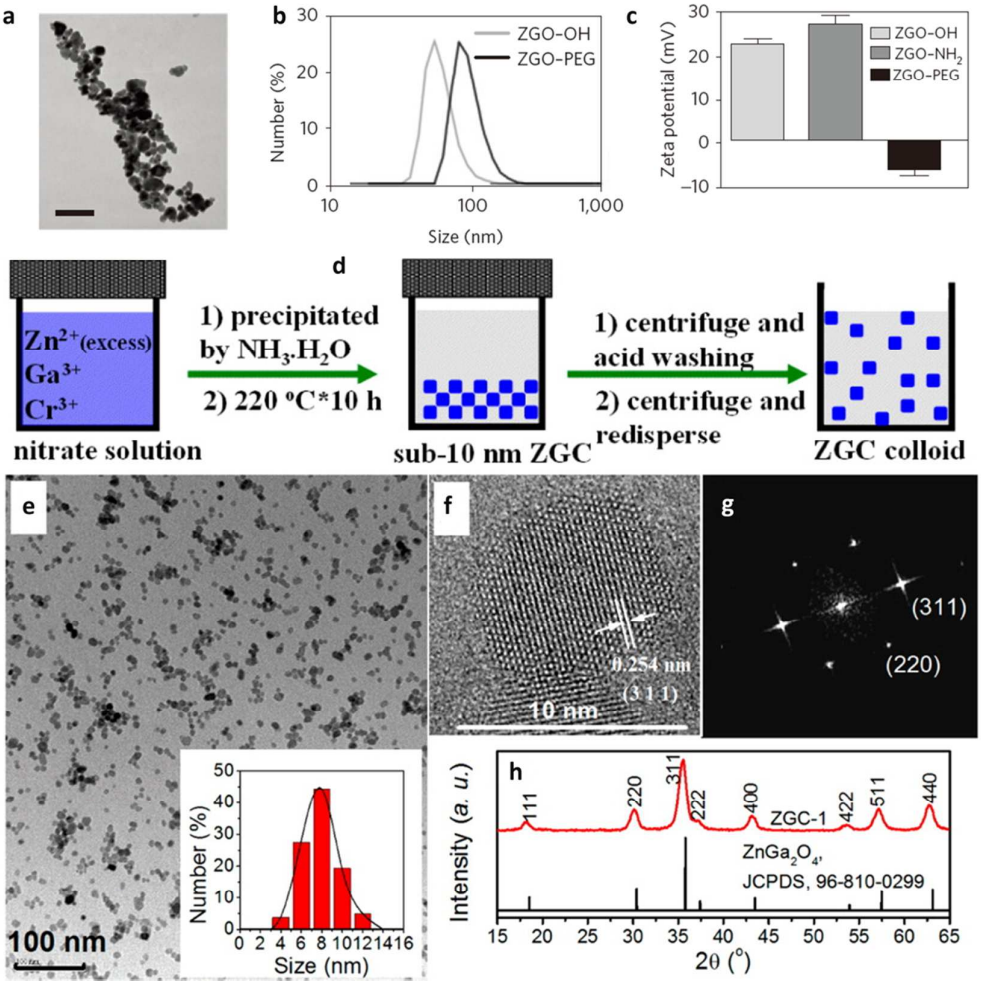

Fig .3 (a) A transmission electron micrograph of $ZnGa_{1.995}O_4$: 0.5%Cr nanoparticles. Scale bar, 100 nm. (b) The hydrodynamic diameter measured by dynamic light scattering in 5% glucose before and after PEG coverage. (c) The evolution of zeta potential as a function of surface coverage (reproduced with permission from ref. 11, copyright 2014, Nature Publication Group). (d) Schematic illustration of the synthesis of $ZnGa_2O_4$: 0.4%Cr^{3+} NPPs. (e) TEM image and size distribution of $ZnGa_2O_4$: 0.4%Cr^{3+} NPPs. (f) HR-TEM image of $ZnGa_2O_4$: 0.4%Cr^{3+} NPPs. (g) SAED. (h) X-ray diffraction pattern of $ZnGa_2O_4$: 0.4%Cr^{3+} NPPs. (reproduced with permission from ref. 29, copyright 2015, American Chemical Society).

Several reports about the different morphology are available on the synthesis of NPPs, such as $SrAl_2O_4$:

Eu^{2+},Dy^{3+} nanosheets,[105] Y_2O_2S: Eu^{3+} M^{2+} (M = Mg, Ca, Sr, Ba), Ti^{4+} nanotubes[106] *etc.* The most successful example for hydrothermal synthesis of NPPs was demonstrated by Thomas Maldiney and co-workers.[11] They synthesized $ZnGa_{1.995}O_4$: 0.5%Cr NPPs with size of 50-100 nm by hydrothermal method. Their experimental results showed the critical factors for the pure products are dependent on the pH value, the initial composition, and the reaction temperature (Fig. 3a-c). Recently, Li *et al*. report on hydrothermal chemical synthesis route to $ZnGa_2O_4$: 0.4%Cr^{3+} NPPs. The specific solution-phase reaction procedure was outlined in Fig. 3d, and this method leaded to monodisperse NPPs s as small as ca. 8 nm. They demonstrated that such sub-10 nm nanocrystals were readily dispersed and functionalized, and can form stable colloidal solutions in aqueous solution (Fig. 3e-h).[29]

2.2.3 *Template method*

Template method is another well-developed synthesis method to fabricate the NPPs.[107] An important strategy is to deposit the long phosphorescent phosphor layer on the surface of mesoporous silica nanospheres (MSNs) resulting in the formation of the MSNs@LPPs composite material (Fig. 4A).[56] This material, which combines the mesoporous structure of MSNs and the phosphorescent property can be used as a novel duel-functional bio-labels and drug delivery system. Up to now, MSNs have found applications as templates on the synthesis of many luminescent materials, such as noble metals, metal oxides, carbon materials, phosphors, *etc.*[56] Following this method, and adding a process of high temperature treatment, template method is seemingly the most promising candidate of synthesizing high-quality NPPs. Zhang and Han *et al.* recently developed the convenient template method to synthesize the persistent phosphorescent nanospheres (SiO_2/$SrMgSi_2O_6$: Eu, Dy, SiO_2/$ZnGa_2O_4$: Cr, SiO_2/$CaMgSi_2O_6$: Eu, Pr, Mn, $CaTiO_3$: Pr) with a narrow size distribution (Fig. 4B-C).[56, 108-110] Firstly, metal ions were impregnated into the mesopores of MSNs templates by immersing MSNs into an aqueous solution of metal ions. Then ion impregnated MSNs were annealed under certain conditions to form phosphorescent nanomaterials with a narrow size distribution. The key feature of this method was that mesoporous silica nanoparticles were not only as the silicon source, but also as hard templates to control the morphology and the size of nanoparticles (50-100nm).[56]

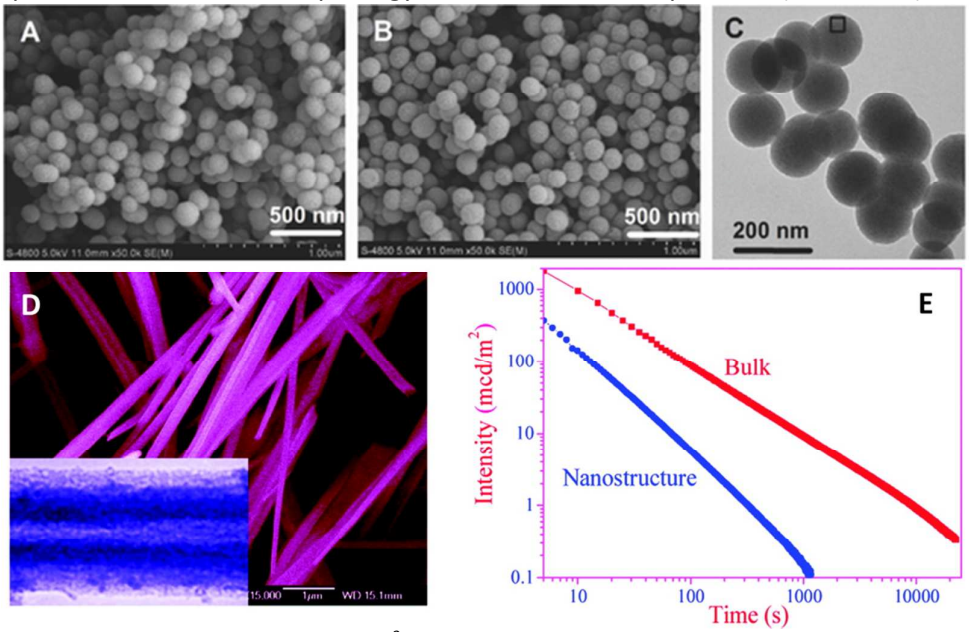

Fig. 4 FESEM images of (A) SiO_2 and (B) SiO_2/$ZnGa_2O_4$: Cr^{3+} prepared by template method. (C) TEM of SiO_2/$ZnGa_2O_4$: Cr (reproduced with permission from ref. 56, copyright 2015, Wiley). (D) FESEM images of $BaAl_2O_4$: Eu^{2+}, Dy^{3+} synthesized by Co-precipitation method. (E) Long persistent duration of bulk-form and nano-$BaAl_2O_4$: Eu^{2+}, Dy^{3+} phosphor (reproduced with permission from ref. 16, copyright 2011, American Chemical Society).

2.2.4 *Co-precipitation*

Co-precipitation is carried by a precipitate of substances normally soluble under the conditions employed. All the raw materials are dissolved in solutions and all the cations are co-precipitated by adding some certain reagent. The precipitates are separated, heat-treated to decompose the precursor and finally annealed to

crystallize the powder. Such approach is an efficient technique for the preparation of the inorganic nanomaterials due to the good mixing of starting materials, which provide a good interspersion of the elements in the precursor, and result in more homogeneous products. Now this technology has also been used to fabricate fluoride-based and oxide-based luminescent nanoparticles. After a higher temperature treatment, this modified co-precipitation technology certainly can be extensively adopted by the researches to prepare the NPPs, such as $(Y_{1-x}Gd_x)_2O_3$: Eu^{3+}, Sm^{3+}, Si^{4+}, Mg^{2+},[111] *etc.* Cheng *et al.* synthesized the hexagonal $SrAl_2O_4$: Eu^{2+}, Dy^{3+} and $BaAl_2O_4$: Eu^{2+}, Dy^{3+}polynary complex nanotubes with LPP by a co-precipitation method, followed by heat treatment in a reducing atmosphere. Their TEM results demonstrated that a great quantity of nanotubes, with about 30-60 nm wall thickness and about 80-200 nm diameter, exist in the sample. But it is pity that tube-form nanomaterials are not suitable as the bio-labels applied in optical imaging (Fig. 4D-E).[16, 112]

2.2.5 Combustion method

Another popular synthesis technique for the preparation of NPPs is combustion method. This technique is based on exothermic redox reactions that undergo self-sustaining combustion. Mixtures of metal nitrates (oxidizers) and a fuel (reducer; e.g., urea, citric acid or glycine) undergo spontaneous combustion under heating, and the chemical energy from the exothermic reaction heats the precursor mixture to high temperatures. The detailed synthesis process can be found in Fig. 5.[86]

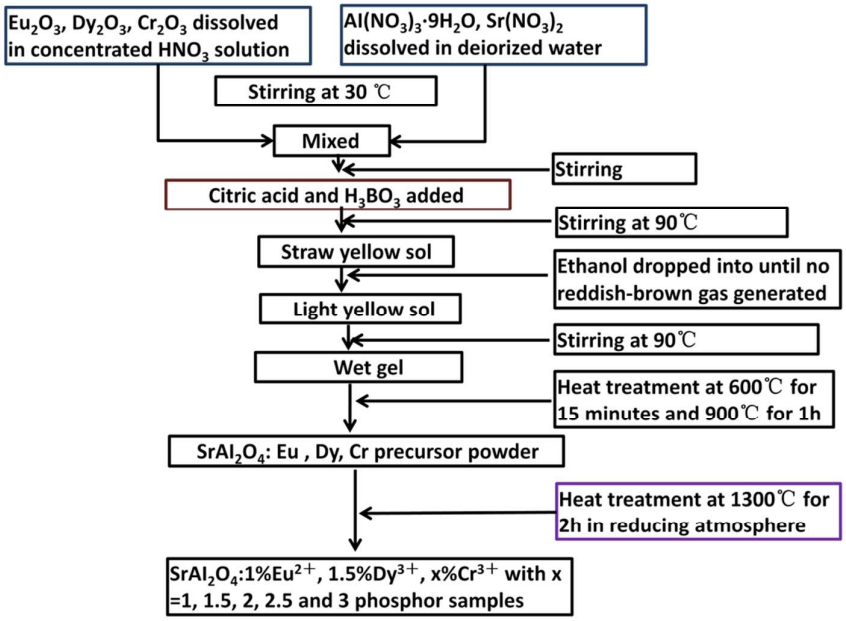

Fig .5 Synthesis process of $SrAl_2O_4$: Eu^{2+}, Dy^{3+}, Cr^{3+} samples via a combustion method.

A high temperature treatment is necessary after getting the precursors. Such a high temperature leads to the formation and crystallization of NPPs. By careful adjustment of experimental variables (like nature of solvents, concentration of precursors, reaction temperature and time), the NPPs with narrow size distribution, good crystallinity, and afterglow properties can be obtained. Cheng *et al.* investigated the influence of organic fuel and post-annealing temperature on the variation of morphology and crystallographic structure.[87] They demonstrated that triethanolamine (TEA) can not only be used as an organic fuel, but also could control the morphology of nanostructured combustion products. With an increase of post-annealing temperature, their morphology transformed from nanosheets into semi-curled nanobelts due to the crystal growth, whose transition presented the following rule: amorphous/hexagonal β-$SrAl_2O_4$ (1000 °C)/monoclinic $SrAl_4O_7$ (1100 °C)/orthorhombic $Sr_4Al_{14}O_{25}$ (1300 °C). In fact, for the synthesis of main aluminium-based NPPs, this method has been widely accepted nowadays. Several reports are available on the synthesis of other NPPs, such as $SrAl_2O_4$: Eu, Dy, Er,[113] Y_2O_2S: Sm,[114] *etc.* using a high temperature combustion technique.

2.2.6 Others

While high-temperature co-precipitation, hydrothermal syntheses, combustion, template method as well as sol-gel are currently well established for the fabrication of monodisperse NPPs, quite a few groups also attempted to develop other synthesized strategies like solvothermal,[115] electrospinning,[89, 107] hydrothermal

ion exchange reaction,[6] microwave synthesis[116] *etc.*

Our group successfully in situ synthesized the red $CaTiO_3$: Pr^{3+}, green $SrAl_2O_4$: Eu^{2+}, Dy^{3+} and blue $CaAl_2Si_2O_8$: Eu^{2+}, Dy^{3+} nanofibers by electrospinning (Fig. 6d-f).[89] The schematic diagram of electrospinning equipment was illustrated in Fig. 6a. By randomly choosing a total number of ten nanofibers in the SEM image, the average diameter was estimated to be 800 nm (Fig. 6b-c). When the as-prepared nanofibers were calcined at 1100 °C, the size of nanofibers decreased due to the degradation and combustion of PVP polymer and organic solvents. We further pointed out that by controlling the electrospinning parameters (the concentration of emission activator, the feeding rate of the solution, the dielectric constant of the precursor solution, *etc.*), the relative emission intensity of $CaTiO_3$: Pr^{3+}, $SrAl_2O_4$: Eu^{2+}, Dy^{3+} and $CaAl_2Si_2O_8$: Eu^{2+}, Dy^{3+} nanofibers can be easily controlled. Consequently, the integrated emitting color of microstructural fibers can be widely tuned in the white triangle region (Fig. 6g).

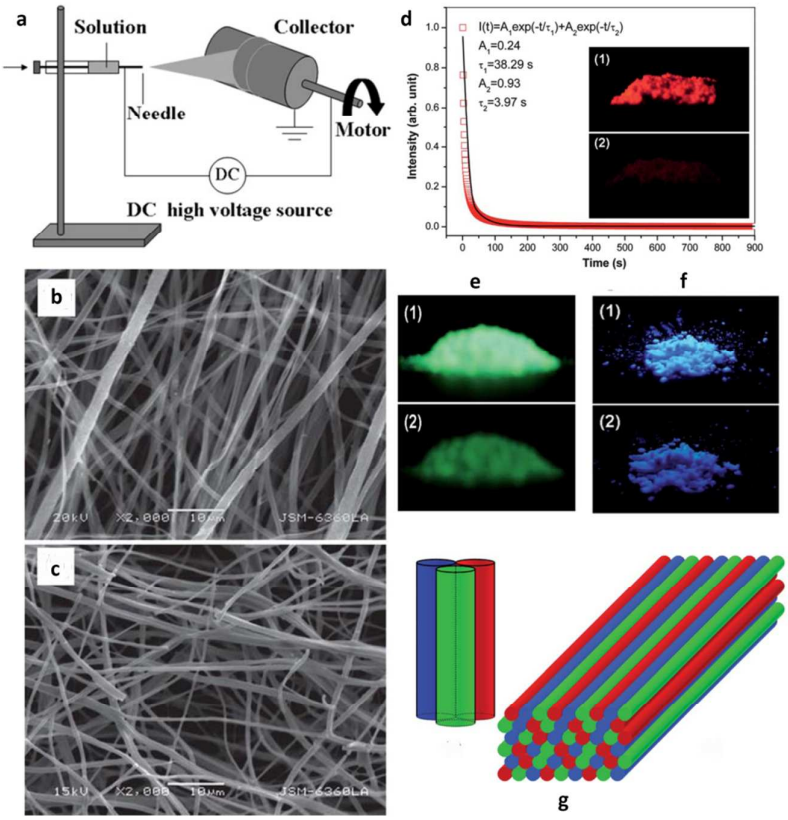

Fig. 6 (a) Schematic diagram of the electrospinning equipment. (b) SEM images of $CaTiO_3$: Pr^{3+} electrospun nanofibers calcined at 1100 ° C. (c) SEM images of $SrAl_2O_4$: Eu^{2+}, Dy^{3+} electrospun nanofibers calcined at 1100 ° C. (d) Afterglow decay curve for the 615 nm emission of $CaTiO_3$: Pr^{3+} electrospun nanofibers. Inset shows the digital photographs of electrospun nanofibers (after grinding) taken (1) upon irradiation with a 365 nm LED, (2) 1 min after the removal of irradiating light. (e) The digital photographs of $SrAl_2O_4$: Eu^{2+}, Dy^{3+} electrospun nanofibers (after grinding) taken (1) upon irradiation with a 365 nm LED, (2) 1 min after the removal of irradiating light. (f) The digital photographs of $CaAl_2Si_2O_8$: Eu^{2+}, Dy^{3+} electrospun nanofibers (after grinding) taken (1) upon irradiation with a 365 nm LED, (2) 1 min after the removal of irradiating light. (g) Schematic diagrams of microstructural fibers and array.

Yan *et al.* synthesized the zinc gallogermanate by hydrothermal ion exchange reaction.[6] The precursor, $K_{0.9}Ga_{0.9}Ge_{0.1}O_2$, was first prepared by solid state reaction, and dispersed in water to form a colloidal suspension. After Zn^{2+} from $Zn(CH_3COO)_2$ aqueous solution was introduced into the $K_{0.9}Ga_{0.9}Ge_{0.1}O_2$ colloidal suspension, hydrothermal treatment was carried out to obtain the zinc gallogermanate. They also indicated that the cubic zinc gallogermanate formed via the ion exchange reaction of 10 $K_{0.9}Ga_{0.9}Ge_{0.1}O_2$+6.5 $Zn(CH_3COO)_2 \rightarrow 4.5(ZnGa_2O_4):(Zn_2GeO_4)+9CH_3COOK+4CH_3COOH$ via the ion exchange reaction. The high resolution TEM image showed that the microstructure resulted from aggregation of the nanocrystals with a particle size of about 10 nm.

Microwave heating technique also is a powerful method to synthesize a wide variety of homogeneous nanoparticles. It presents several advantages over conventional heating techniques, such as: rate

enhancement fast synthesis, no grinding process, less time, homogeneous heating, selective heating, indirect contact between the heating source and the reactants and/or solvents, and improved reproducibility. Microwave chemistry definitely fulfils the promise of being a fast synthesis technique. These early applications of microwave radiation have been applied to the synthesis of modern, advanced materials such as nano-materials, thin films, and porous ceramics. This new method, allows the synthesis of $SrAl_2O_4$: Eu: Dy, $CaTiO_3$: Pr, *etc.* in less time by using microwave-assisted.[116]

2.3 Physical process

2.3.1 Laser technique (ablation/deposition)

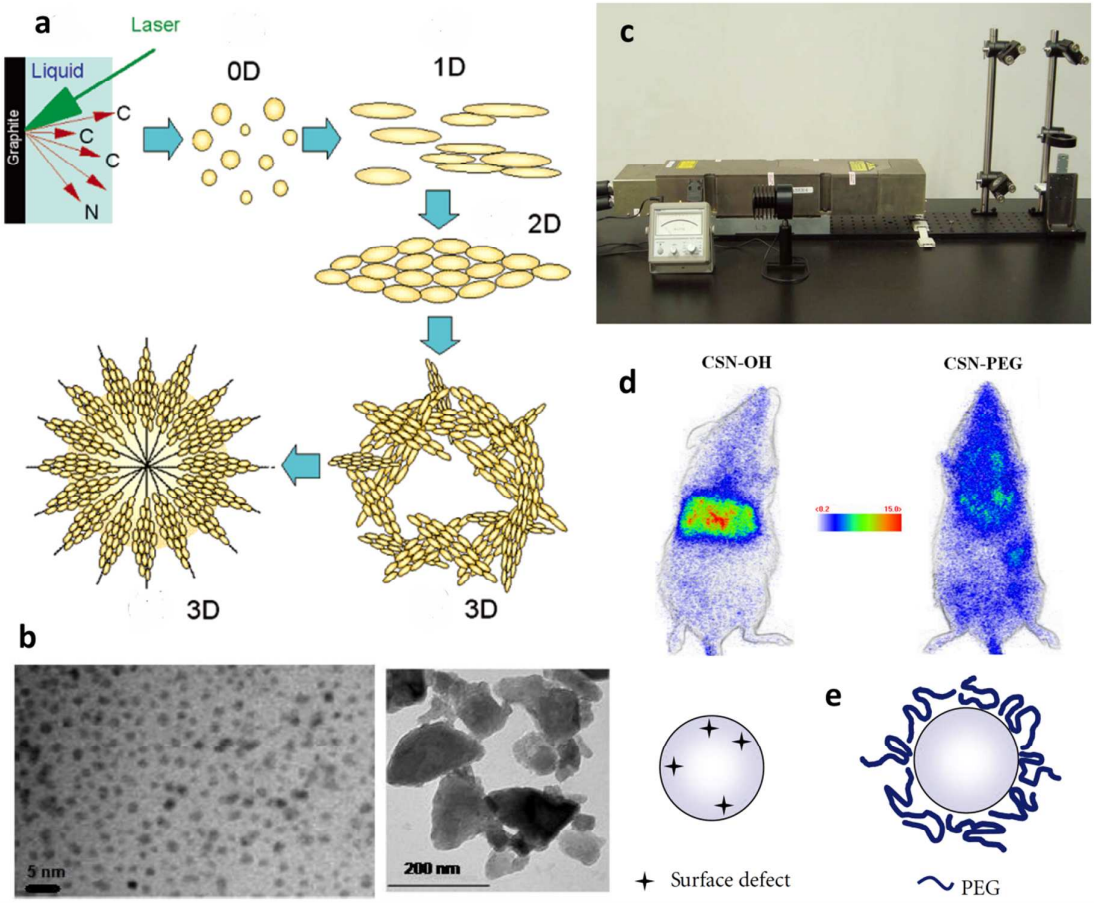

Fig. 7 (a) Proposed sequential growth pathway model involving structural and morphology modifications by using laser ablation (reproduced with permission from ref. 117, copyright 2006, American Chemical Society). (b) Transmission electron micrograph (TEM) of the obtained nanoparticles from the laser ablation technique (reproduced with permission from ref. 118, copyright 2012, American Optical Society). (c) Equipment for laser ablation in liquid (reproduced with permission from ref. 90, copyright 2011, Elsevier). (d) Biodistribution of $Ca_2Si_5N_8$: Eu^{2+}, Tm^{3+}-OH and $Ca_2Si_5N_8$: Eu^{2+}, Tm^{3+}-PEG, 15 minutes after tail vain injection (reproduced with permission from ref. 118, copyright 2012, American Optical Society). (e) Schematic of an afterglow nanoparticle and of PEG molecules. An afterglow nanoparticle without the addition of PEG. An afterglow nanoparticle capped with PEG molecules at a high PEG concentration (reproduced with permission from ref. 90 copyright 2011, Elsevier).

The route of firstly preparing the LPPs and then improving the morphology and particle size refers to plasma etching process and laser ablation/deposition, where the phosphors are formed or “broken off” from a larger structure (Fig. 7a).[117] Laser ablation seems to combine many advantages compared to other synthesis techniques, with respect to size distributions of the nanoparticles. In fact, the processing of various nanomaterials has already been reported by using this method, such as noble metal nanoparticles, semiconductor, etc. The representative equipment used for laser ablation in liquid is shown in Fig. 7c. The target is first placed in a cell filled with water or ethyl alcohol, and then irradiated with a focused laser beam. By controlling parameters of the laser source (wavelength, repetition rate, peak power, focusing conditions and irradiation) it is easy to obtain the desired nanoparticles with different morphology and size.

Fumitaka Yoshimura *et al.* prepared the $Sr_2MgSi_2O_7$: Eu^{2+}, Dy^{3+} NPPs by using this technique.[90] They

demonstrated the size of nanoparticles could be controlled by the energy density of laser. During this process, some by-products were also produced, depending on the liquid used. The amount of by-product was reduced by a decrease in the energy density, which also decreased the particle size of the nanoparticles. To improve the quantum yield and biocompatibility more suitable for the application in bio-imaging, they added PEG as the auxiliary. An increase in the amount of PEG increased the quantum yield of the nanoparticles and improved the afterglow property at the same time (Fig. 7e). Thus it can be seen that this technique is a good candidate of synthesizing high-quality NPPs, in the case of ignoring the cost.

Thomas Maldiney *et al.* further demonstrated the main three synthesis of $Ca_2Si_5N_8$: Eu^{2+}, Tm^{3+} bio-label with LPP: first preparing the bulk-form LPPs, second synthesizing nanoparticles with the pulsed laser ablation method in liquid and finally the surface modification (Fig. 7b). Meanwhile, they revealed the influence of surface functionalization on the biodistribution of bio-maker after systematic injection and discussed the potential application in *in vivo* imaging of these functionalized nanoparticles (Fig. 7d).[118]

2.3.2 Swift heavy ion irradiation and electron beam bombardment

In fact, the third strategy of synchronously activating afterglow and limiting the size of nanoparticles is more ideal. But it is very hard to realize this goal. Swift heavy ion (SHI) irradiation and other electron beam bombardment *etc.* have a wide variety of applications in many fields such as biology, medicine, physics, and material science.[40, 119] They are always used to evaporate materials which are hard to evaporate by thermal evaporation due to high melting points of these materials. The intense energy deposition in the target material is several orders of magnitude higher than that of conventional ionizing radiation processes, thus making loss of some atoms and leading to vacancy defects formation during the process. The formation of defects has been observed in many materials, including semiconductors, insulators and various metals. Therefore, SHI irradiation or electron beam bombardment is a strong candidate for the synthesis of NPPs through the formation of suitable lattice defects. Xu *et al.* presented a approach for improving the afterglow of long-lasting phosphors with swift heavy ion irradiation. The afterglow time of famous $SrAl_2O_4$: Eu^{2+} NPPs was dramatically enhanced with swift heavy ion irradiation.[120] P. Smet *et al.* found that electron-beam annealing was a viable option to reduce the europium ions in $CaAl_2O_4$: Eu, Nd LPPs and it leaded to well-crystallized nanoparticles, having a long and bright afterglow. Though this method was highly efficient, energy saving, very low contamination, and uses or produces no hazardous byproduct, it also had to face the stringent requirement of high cost.[91]

2.4 Brief summary

In summary, up to now, there is still no perfect synthesis technology to prepare the nanoparticles with longer afterglow time, smaller particle size, higher homogeneity, and highly controllable morphology. Solid-state reaction, with its highest synthetic temperature, is certainly beneficial for improving the persistent duration, but lead to the micro-grade products. Liquid phase reaction is more suitable for synthesizing the nanomaterials, but the smaller particle size, higher homogeneity, and highly controllable morphology are only obtained without high temperature treatment or under a lower sintering temperature. Meanwhile, such condition certainly leads to a shorter persistent time. Therefore liquid phase reaction used to synthesize NPPs is a technology, which first synthesizes the nano-materials and then activates the long persistent phosphorescence, while the related physical process is followed a reverse order, i.e. first preparing the LPPs and then reducing the particle size. The post-processing of physical method has already partly improved the size distribution and the monodispersity, but the morphology of as-papered nanoparticles is uncontrollable. More notably, this physical irradiation requires the advanced equipment and the high cost, which limit its more wide application. Therefore, it is necessary to develop a new technology of synthesizing the nanoparticles with longer persistent duration, smaller particle size, higher homogeneity, and highly controllable morphology.

3. Mechanisms

As discussed above, for the trapping and de-trapping process of a given persistent phosphor, usually three important issues should be considered, i.e. trap types, concentrations and depths.[121-123]

(1) **The type of effective traps**. Generally speaking, the involved traps correspond to some lattice defects, i.e. intrinsic defects, intentionally introduced defects or both. There are essentially four processes by which crystal defects can be formed: (a) as the result of thermal dissociation and disorder, when the material is heated to a high temperature; (b) by exposing the material to an excess pressure of one of its constituents, usually at an elevated temperature; (c) by bombarding with electron beam, high-energy rays, nuclear particles or high intensity laser; and (d) by incorporating impurities which require a simultaneous formation of crystal defects to permit their incorporation. Even if the traps can be formed during the above conditions, it is still not easy to identify the species of traps. Moreover, it is also very hard to accurately predict which defect is authentically responsible for the capture of carriers.

(2) **The concentration of effective traps**, i.e. the number of traps who have the ability of capturing carriers. Introducing more effective traps is beneficial to capturing more electrons. Increasing the capacity of electron reservoir is a considerable issue for improving the persistent duration.

(3) **The depth of effective traps**, i.e. the release rate of the carriers captured in traps, which determines the phosphorescent intensity and afterglow time. Shallow traps are fast emptied at room temperature, and a high release rate is beneficial to get a strong phosphorescent intensity. Deep traps with the slower release rate, on the other hand, are hardly emptied at room temperature. Parts of carriers are even stored in deep traps under the room temperature. Such slow release rate leads to a weaker phosphorescent intensity and long persistent duration.

Though different mechanisms have been suggested, ranging from the basic theoretical models to complex experimental models, there is still controversy in explaining the trapping and de-trapping process of carriers. In this part, we review three most widely accepted models, i.e. conduction band (CB)-valence band (VB) model, quantum tunneling model, and oxygen vacancy model.

3.1 Conduction band-valence band model

Trapping is a fundamental process for energy storage in LPPs. This energy storage is accomplished by the spatial localization of the excited carriers near to CB/VB. When the trapped electron or hole is released into CB/VB, it is free to move until captured by a recombination center or by another trap. This model is proposed based on the fact that the CB or VB has participated into the excitation, capture, migration and release process of carriers, and the involved traps should be near to CB/VB. The main CB-VB models include hole model, electron model and energy-band engineering model, *etc.*

3.1.1 Hole model

Matsuzawa *et al.* explained the origin of the extraordinary LPP of $SrAl_2O_4$: Eu^{2+}, Dy^{3+} LPPs (Fig. 8a).[124] In their model, holes were assumed to be the main charge carriers. Abbruscato *et al.* supported this assumption, *i.e.* holes in the valence band had to be the main charge carriers based on earlier measurements of $SrAl_2O_4$: Eu^{2+}, which also showed a weak afterglow. Matsuzawa *et al.* subsequently performed a photoconductivity measurements to support the hole model.[125] They further pointed out that when a Eu^{2+} ion was excited by photon, there was a possibility that a hole escaped to the VB, thereby leaving behind Eu^{+} ion. The hole was then captured by a trivalent rare earth ion, such as Dy^{3+}, thus creating a Dy^{4+} ion. After a while, thermal energy caused the trapped hole to be released into the VB again. From there it moved back to a Eu^{+} ion, allowing it to return to the Eu^{2+} ground state with emission of a photon.

3.1.2 Electron model

In 2003, Aitasalo proposed that electrons were excited directly from the VB into trap levels of unspecified origin (Fig. 8b).[126] Since the CB was located too high above the energy level of the oxygen vacancy trap to enable a thermally assisted transition to the CB, they assumed that the energy released on recombination of the electron and the hole was delivered directly to the Eu ions, by means of energy transfer. Electron model also successfully elaborated the doping influence of trivalent rare earth co-dopants. But they disagreed with the existence of Eu^{+} and Dy^{4+} in aluminate or silicate compounds. They pointed out that the reduction of Eu^{2+} to Eu^{+} and the oxidation of Dy^{3+} to Dy^{4+} would result in chemically unstable ions. They suggested that trivalent rare earth co-dopants increased the number of lattice defects, because they occupied the divalent alkaline earth sites, leading to spontaneous defect creation for charge compensation.[127]

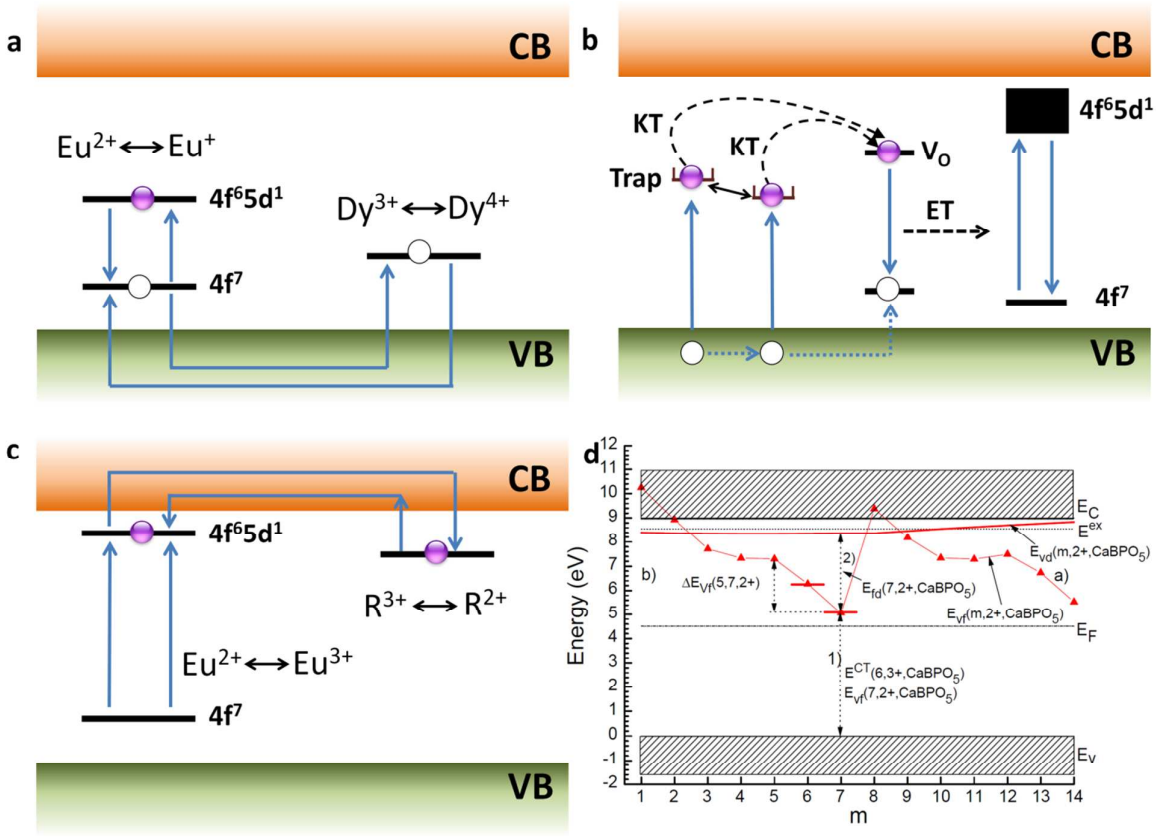

Fig. 8 (a) Hole model: Afterglow mechanism proposed by Matsuzawa *et al.* for $SrAl_2O_4$: Eu^{2+}, Dy^{3+}; (b) Electron model: Afterglow mechanism proposed by Aitasalo *et al.* for $CaAl_2O_4$:Eu^{2+},Dy^{3+}; (c) Persistent phosphorescence mechanism proposed by Dorenbos *et al.* for aluminate and silicate compounds; (d) Energy level scheme of the divalent lanthanides in $CaBPO_5$.

(reproduced with permission from ref. 130, copyright 2005, Electrochemical Society).

Holsa *et al.* also agreed that Eu^{+} species were unstable in aluminate.[126] They proposed that the co-doping of R^{3+} ions, such as Dy^{3+} maybe only serve as the trap centers to modulate the trap distribution via charge compensation. They also prepared the additional $SrAl_2O_4$: Eu, Sm LPPs, and found the adding Sm^{3+} into $SrAl_2O_4$: Eu was detrimental for the persistent duration. The reason was that Sm^{3+} ions were easily reduced to Sm^{2+} in the N_2-H_2 atmosphere, thus leading to a lower concentration of traps. Based on this assumption, they gave a plausible mechanism for LPP of $CaAl_2O_4$: Eu, Nd and ZrO_2: Ti. In their investigation, their employed EPR, XPS, and XANES techniques, indicating the facts that except for the $Eu^{2+} \rightarrow Eu^{3+}$ oxidation during excitation, no change in the co-dopants' valence were observed experimentally during the persistent duration. In fact, some phosphors with co-dopant e.g. $Sr_2MgSi_2O_7$: Eu, Dy and $SrAl_2O_4$: Eu, Dy *etc.* show intense and longer persistent phosphorescence compared with single-doped phosphors. The reason is that the introduced co-dopant Dy^{3+} is just used to regulate the trap parameters.[94]

Clabau *et al.* also did not accept the Matsuzawa model. EPR measurements presented a decrease in the Eu^{2+} concentration during excitation, followed by an increase as soon as the excitation was terminated, continuing until the afterglow ended. Thus they suggested Eu^{2+} participated in the trapping and de-trapping process, which contradicted the idea of energy transfer to Eu^{2+} after the trapping, as suggested by Aitasalo.[128]

3.1.3 Energy band engineering model

Dorenbos *et al.* agreed with Aitasalo model, further they pointed out that the suggested carriers on the ground state of Eu^{2+} after excitation was based on faulty reasoning (Fig. 8c).[129] The energy levels of lanthanides were localized, in contrast to the delocalized Bloch states of the valence and conduction band. He revised the electron model, and suggested a different model in 2005.[130] In this model, another obvious distinction was that electrons were excited from divalent europium ions, but valence band. Since 5d level of divalent europium located very close to the conduction band, these excited electrons were easily released into the CB and subsequently caught by a trivalent rare earth ion. This revised electron model also didn't explain the

existence of LPP in Eu^{2+} singly doped $SrAl_2O_4$ phosphors.

Further, they offered some strategies and methods to quantitatively calculate the lanthanide energy levels of different LPPs.[103, 131] The involved factors include (i) the energy level positions of the R^{2+} and R^{3+} ions, (ii) the band gap energy of hosts, and (iii) the trap level positions with respect to the bottom of the conduction band of hosts. Diffuse reflection spectra gave the data of band gap energy of hosts, while the trap level positions could be evaluated by the measurement of thermoluminescence spectra as will be discussed later. A big problem was getting the energy level positions of the R^{2+} and R^{3+} ions. Holsa *et al.* provided a route of estimating the ground level and excitation level energies for R^{2+} and R^{3+} ions in the host band structure using $CdSiO_3$: Tb^{3+} as an example.[23, 30, 132] They pointed out that (a) a previous empirical model was based on the idea that the trends in ground state energies for both R^{2+} and R^{3+} ions were independent of the host. This meant that once the energy of ground level for a R^{3+} ion in one host was found, these data for any other R^{3+} ion were easily obtained according to Dorenbos model (Fig.8d). For instance, the level position of Tb^{3+} ($^7F_6$) ground level could be thus estimated using the corresponding data for the Eu^{3+} ($^7F_0$) ground level in $CdSiO_3$, even though only the energy level of Eu^{3+} ($^7F_0$) in $CdSiO_3$ could be identified via the experimental data. (b) Transition intensity of different excitation peaks need to be considered in order to give an accurate judgment of afterglow excitation bands. Such as, the intensity of $4f^8 \rightarrow 4f^7 5d^1$ (or $4f^1 \rightarrow 5d^1$) transitions in the excitation spectra of Tb^{3+} was suppressed when the $4f^7 5d^1$ levels were in the host's conduction band.

Based on the above method, they investigated the ground energy level positions for the R^{2+} and R^{3+} ions in $Sr_2MgSi_2O_7$ materials, and pointed out the best candidates for afterglow centers were (in this order) Eu^{2+}, Ce^{3+}, Tb^{3+} and Pr^{3+}. First of all, all these ions were known to be strong emitters with weak tendency to lose the excitation energy in cross relaxation or multiphonon de-excitation processes. As for LPP, most present day applications preferred the excitation (daylight or artificial lighting) with visible light or, if not possible, with UV radiation having energy as low as possible. The Eu^{2+}, Ce^{3+}, Tb^{3+} and Pr^{3+} had the lowest 5d energies known in the rare earth series ensuring the low excitation energies. Further, the overlap between the excited 5d levels and the host's CB was required and achieved by these ions for efficient electron transfer through CB to traps. Though the excitation of the trivalent ions (Ce^{3+}, Tb^{3+} and Pr^{3+}) usually requires the use of UV radiation, Eu^{2+} can be excited in many hosts by the blue light, as well. [133-135]

Thermoluminescence (TL) measurement is usually considered as a powerful tool to calculate the trap level positions. The calculated data from TL peak corresponds to trap level positions. Bos *et al.* and Zych *et al.* independently measured glow curves of YPO_4: Ce^{3+}, R^{3+} (R=Nd, Sm, Dy, Ho, Er and Tm) phosphors and YPO_4: Pr^{3+}, R^{3+} (R=Nd, Dy, Ho and Er) phosphors, respectively.[27, 136] It was noticed that TL peaks of YPO_4: Pr^{3+}, R^{3+} were exactly matched to the corresponding TL peaks in YPO_4: Ce^{3+}, R^{3+}. There are some similar values of activation energies for electron detrapping from R^{2+} for both Pr^{3+}-doped and Ce^{3+}-doped YPO_4. Although this was not a typical Eu^{2+}-based compound, these results seemingly confirmed that the codopant indeed played the role of traps in some materials.

3.2 Quantum tunneling model

Quantum tunnelling refers to the quantum mechanical phenomenon where a particle tunnels through a barrier that classically could not surmount. This process may occur between the traps and near excited state level of activators. In contrast to CB-VB model, this model doesn't require a physical proximity of traps' level position and CB/VB. That means such model is mainly used to explain the afterglow mechanism related to deep traps. Hoogeustraten *et al.* first proposed the existence of quantum tunneling in sulfide.[137] After then Tanabe *et al.* presented the similar model related to $SrAl_2O_4$:Eu^{2+}, Dy^{3+} LPPs.[138] They found most of the 5d levels of Eu^{2+} at the Sr site with weak crystal field were located within the conduction band by measuring photocurrent excitation spectra. Based on this discovery, they suggested the effective path for trapping and de-trapping is found to be achieved by quantum tunneling path not through the conduction or valance band.

Pan *et al.* reported a series of Cr^{3+}-doped zinc gallogermanate NIR LPPs that exhibit strong emission at 650–1000 nm and with a super-long afterglow of more than 360 h.[12] The effective activation of afterglow by ultraviolet light revealed that the approximate energy of the ionization threshold level in the $Zn_3Ga_2Ge_2O_{10}$ host was near the conduction band. This was consistent with the CB-VB model (process 2, 3 in Fig. 9a and

process 2, 4 in Fig 9b).However, the fact that low-energy visible light (400-630 nm), whose energy was below the ionization threshold, could still produce weak but super long persistent phosphorescence. They thus proposed another mechanism involving the electron trapping and detrapping processes, i.e. quantum tunneling process (process 4, 6, 7 in Fig. 9a and process 5 in Fig 9b). Under low-energy visible-light excitation, the ground state electrons of Cr^{3+} ions were promoted to energy levels of deep traps below the ionization threshold and the traps were filled through the tunneling process from the energy-matched Cr^{3+} energy levels. The reverse tunneling recombination produced weak but super long afterglow. Subsequently they reported the similar phenomenon from a Cr^{3+}-doped $LiGa_5O_8$ NIR persistent phosphor, which exhibits a longer persistent duration of more than 1000 h.[139]

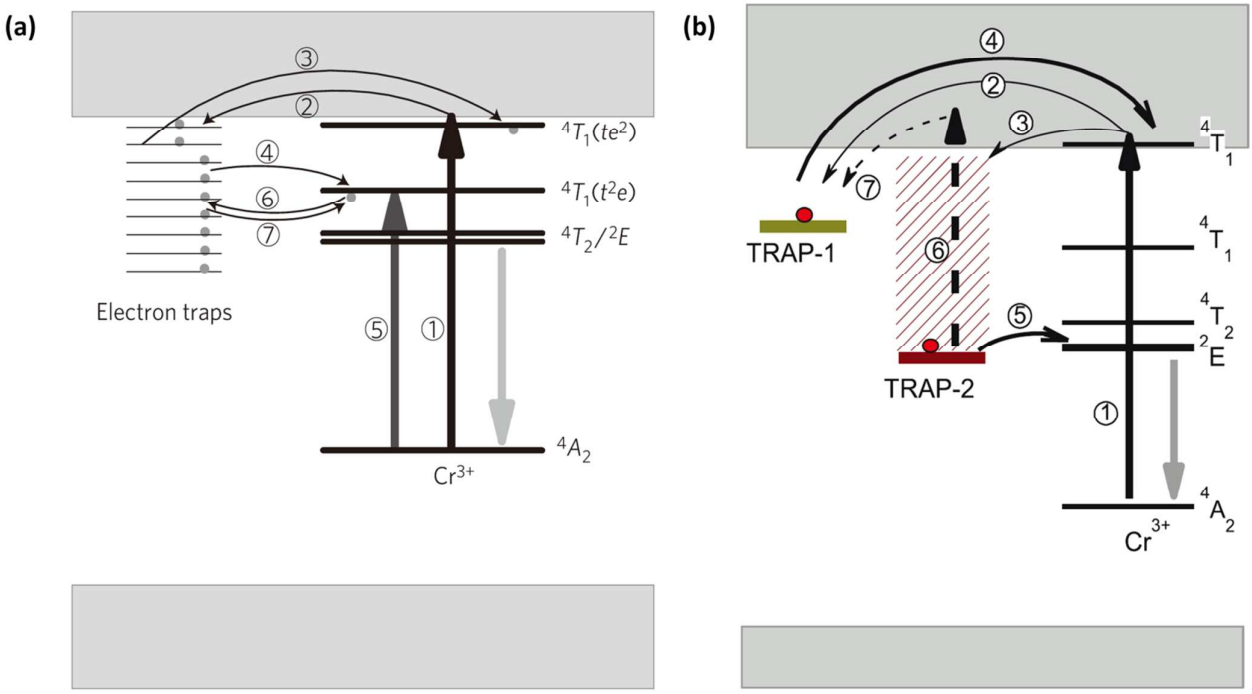

Fig. 9 (a) Schematic representation of persistent NIR luminescence mechanism. The straight-line arrows and curved-line arrows represent optical transitions and electron transfer processes, respectively (reproduced with permission from ref. 12 copyright 2012, Nature Publication Group). (b) Representation of the NIR persistent phosphorescence and photo stimulated NIR persistent phosphorescence mechanisms (reproduced with permission from ref. 139, copyright 2013, Nature Publication Group).

3.3 Oxygen vacancy model

Our group discovered the photo stimulated luminescence from Eu^{2+}-doped fluoroaluminate glasses,[140] Eu^{2+}-doped strontium aluminosilicate glasses,[141] Ce^{3+}-doped alkali borate and silicate glasses,[142] as well as gold nanoparticles-doped glasses,[143] *etc*. We proposed an afterglow model, oxygen vacancy model, to explain the trapping and de-trapping progress by analyzing the EPR spectra. Oxygen vacancy model was oxygen vacancy as the electron trap to capture the electron, which is universally suitable for analyzing the afterglow mechanism of oxide-based LPPs. Such model was built based on the identification and confirmation of trap types, other than CB-VB and quantum tunnelling model. In earlier research, Aitasalo *et al.* suggested an oxygen vacancy as the important electron trap in their electron model. Clabau *et al.* also agreed that oxygen vacancies acted as an efficient electron trap in $SrAl_2O_4$: Eu^{2+},Dy^{3+}. By comparing glow curves of Eu^{2+} singly doped $SrAl_2O_4$ and Eu^{2+}/Dy^{3+} co-doped $SrAl_2O_4$, they found that two TL peaks were differed in size and location, but were very similar in shape. From this, they concluded that the chemical nature of traps was not influenced by co-doping, and only oxygen vacancies still worked for the store and release of electrons in all the phosphors. In fact, point defects existed extensively within oxide-based materials. Lim *et al.* studied the afterglow properties of Ti-doped spinel phosphor powders. From their investigation, the observed 620 nm red emission should be ascribed to Mg^{2+} and O^{2-} vacancies, because a pure spinel was reported to have many intrinsic defects, such as Mg^{2+} and O^{2-} vacancies and they often appeared in pair, known as Schottky defects.[92]

3.4 Brief summary

Until now the suggested models still probably failed to satisfactorily explain all of the observed phenomena. Model about energy level schemes was a major breakthrough. At least it made possible to predict the following: 1) charge carriers' species of the trapping and detrapping process; 2) identification of the most probable centers for persistent phosphorescence; 3) the role of (rare earth) co-dopants, *i.e.* traps capturing electrons in the conduction band; 4) to predict the afterglow excitation band. Now it allows designing an efficient long phosphorescent phosphor via a comprehensive consideration on the band gap energy of hosts and energy level structure of luminescence centers. Though some experimental difficulties still exist, the relationship between two now can be partly controlled. The biggest problem of the research in afterglow mechanism needing to be faced is an all-sided understanding of trap type, trap concentration and de-trapping probability of captured electrons. The physicist or material scientist need to answer three questions: what are the efficient traps who have the ability of capturing the excited electrons; what is the concentration of such traps; and what is the released ratio of stored electrons.

4. Characterizations

In an optical material, the luminescent and phosphorescent properties should be firstly performed with spectrophotometer in order to identify which activator is taking part in this optical process. The related measurements include photoluminescent/phosphorescent spectra, photoluminescent/phosphorescent excitation spectra, and decay curves in UV-VIS-NIR wavelength ranges. When multiple peaks or bands are presented in photoluminescence (PL) or PL excitation (PLE) spectrum, the corresponding emission and excitation spectra for each peak or band should be measured. Not only PL and PLE spectra during excitation, but also afterglow spectrum needs to be investigated. In this way, it is clear which activators are taking part in the persistent phosphorescence and which do not. If the afterglow emission spectrum changes over time, it might be valuable to show the spectrum at different time intervals after the excitation, since different defects have different trapping time. Another important consideration is structural characterization, such as, X-ray diffraction (XRD), thermal analysis, scanning electron microscopy (SEM), transmission electron microscopy (TEM), Raman spectrum, or X-ray photoelectron spectroscopy (XPS) *etc*.[9, 144, 145]

Comparing to structural characterization, the nature of traps as well as trapping and de-trapping process is more important for understanding the afterglow mechanism, since crystal defects can play an important role as traps in determining the optical, electrical, and photoconductivity properties of materials. In this part, characterizations for the investigation of trapping and de-trapping processes are discussed. These methods include both spectroscopy techniques and special measurements (electron spin resonance, photocurrent and positron annihilation lifetime spectroscopy). The related spectroscopy studies refer to UV-VUV synchrotron radiation emission and excitation spectroscopy, thermoluminescence (or, thermally stimulated luminescence, TL) and its excitation spectra, X-ray absorption spectroscopy as well as afterglow kinetics curves. With these methods we are able to get some important qualitative and quantitative information of defect parameters. A targeted collection for characterization methods of long phosphorescent phosphors is beneficial to identify the trap types, concentrations and depths, and set up the accurate afterglow model.

4.1 Electron spin resonance

Electron paramagnetic resonance (EPR), also called as electron spin resonance (ESR), deals with the interaction between electromagnetic radiation and magnetic moments of electrons. It is a technique applicable to systems in a paramagnetic state. The species exists either in a paramagnetic ground state or may be temporarily excited into a paramagnetic excited state, for instance, by irradiation. Typical systems that have been studied include:

1) Free Radicals in the solid, liquid or gaseous phases. A free radical is herein defined as an atom, molecule or ion containing one unpaired electron.

2) Transition ions including actinide Ions.

3) Various point defects (localized imperfections, with electron spin distributed over relatively few atoms) in solids. Best known in this class is the F center, an electron trapped at a negative-ion vacancy in crystals and

glasses. Deficiency of an electron (a 'positive hole') may also give rise to a paramagnetic entity.

4) Systems with more than one unpaired electron. Excluding ions in category 2, these include: triplet-state systems, biradicals and multiradicals.

An EPR spectrum is observed making the magnetic field vary (abscissa of the spectrum) and recording the absorption of the microwave irradiation. This EPR signal appears at the resonant field where the energy between the two electronic spin sublevels created by the magnetic field (gβH, where g is the lande factor, β the Bohr magneton and H the magnetic field applied to the sample containing radicals with spin S=1/2 for instance) is equal to the energy of the fixed microwave (hν, where h is the Planck constant and ν the microwave frequency).This equality is the fundamental equation in EPR: hν=gβH.

EPR has proved to be an important tool in the study of semiconductors, particularly in identifying and elucidating the structure of point defects and impurity ions. And now many researchers are trying to explore the species of traps in LPPs by using EPR. Here we focus primarily on solids containing independent unpaired-electron species, limited to relatively few atoms in each center. Depending on the anisotropy, some important classes of paramagnetic systems mainly include free radicals, transition ions surrounded by ligands, and point defects. Table 2 lists the investigations about the parameters of X-band EPR spectra of different LPPs. EPR signals of LPPs are all in correlation with various point defects or doping ions (transition metal and rare earth). It should be specially mentioned that if the g value of the new EPR signal is smaller than that of the g factor of free electron, which is 2.0023, the signal is due to the trapped electron. However, if the g value is bigger than 2.0023, the new signal is ascribed to the trapped holes.

Table 2. Parameters of X-band EPR spectra of different LPPs.

Phosphor	G-factors	Attribution	Reference
$CaYAl_3O_7$: Ce^{3+}	2.002	an electron is trapped at an oxygen vacancy	146
	2.012	a hole is self-trapped around a single Al^{3+} ion	
$ZnGa_2O_4$: Cr^{3+}	1.976	Cr^{3+}-Cr^{3+} pairs	49, 147
$Ca_{10.43}Mn_{0.07}(PO_4)_7$	2	Mn^{2+} ions located in octahedral sites	148
$CaMgSi_2O_6$: Mn^{2+}	2	typical hyperfine sextet of Mn^{2+}	149
$Zn_2P_2O_7$: Tm^{3+}, Mn^{2+}	2.031	holes trapped by V'_{Zn}	150
	1.997	electrons captured by $Tm^{\bullet}_{Zn}$	
$Zn_3Ga_2SnO_8$: Cr^{3+}	2.004	defect agglomerate composed by single ionized Zn interstitial and the Zn vacancy capturing an electron	62
	2.08	Cr^{3+}–Cr^{3+}exchange-coupled pairs or small clusters of several exchange-coupled pairs	
	2.45	isolated Cr^{3+} centers at strongly-distorted octahedral sites	

Our group has done a lot of work in explaining the nature of defects in Cr^{3+} and Mn^{4+}-doped LPPs ($Zn_3Ga_2SnO_8$: Cr, $Zn_3Ga_2GeO_8$: Cr, $Zn_3Ga_2Ge_2O_{10}$: Cr, $LaAlO_3$: Mn, $GdAlO_3$: Mn), and BCNO (BN-based phosphor containing impurity of carbon and oxygen).[62, 151, 152] EPR spectra of $Zn_3Ga_2SnO_8$: 0.5 Cr^{3+} powders at different time intervals (30 min, 6 h, 24 h and 96 h) after they were irradiated by a Xenon lamp for 10 min, were measured (Fig. 10a). Signals with *g*=2.004, *g*=2.08 and *g*=2.45 could be detected before and after the irradiation. Signals with *g*=2.08, and *g*=2.45 remained unchanged at different time intervals, only the signal intensity with *g*=2.004 was seen to decrease. ESR signal with *g*=2.45 in $Li_2B_4O_7$: Cr^{3+} glass belonged to isolated Cr^{3+} centers at strongly-distorted octahedral sites. The signal with *g*=2.08 was attributed to the Cr^{3+}–Cr^{3+}exchange-coupled pairs or small clusters of several exchange-coupled pairs. Line in the ESR spectra at *g*=2.0024 was attributed to the Zn vacancy in zinc oxide, ESR signals due to singly negatively charged Zn vacancy (V_{Zn}) and zinc vacancy interstitial zinc complex (V_{Zn}: Zn_i) were with a *g* value very close to 2 in zinc oxide phosphor. Signal with *g*=2.0046 may be assigned to single ionized Zn interstitial (Zn_i, monovalent Zn or Zn^+) in Zn_2GeO_4phosphor.To sum up, considering the point that the value of signal with *g*=2.004 was close to the *g*-factor (*g*=2) of single electron ion, it should be attributed to the defect agglomerate composed by single ionized Zn interstitial and the Zn vacancy capturing an electron.[62]

In addition to the EPR singles of Cr^{3+} ion, we also investigated the Mn-related EPR singles (Fig. 10b). We obtained the EPR signals of Mn^{2+} in Mn^{4+}/Ge^{4+} -co-doped $MAlO_3$ (M=La, Gd). The typical hyperfine sextet arising from the Mn^{2+} ion remained the same at the different time intervals, verifying that the Mn^{2+} center were detained indeed in the phosphor, but it was not the efficient defect center and did not work at all for the afterglow emitting. Unfortunately, no any EPR single of Mn^{4+} was observed.[151]

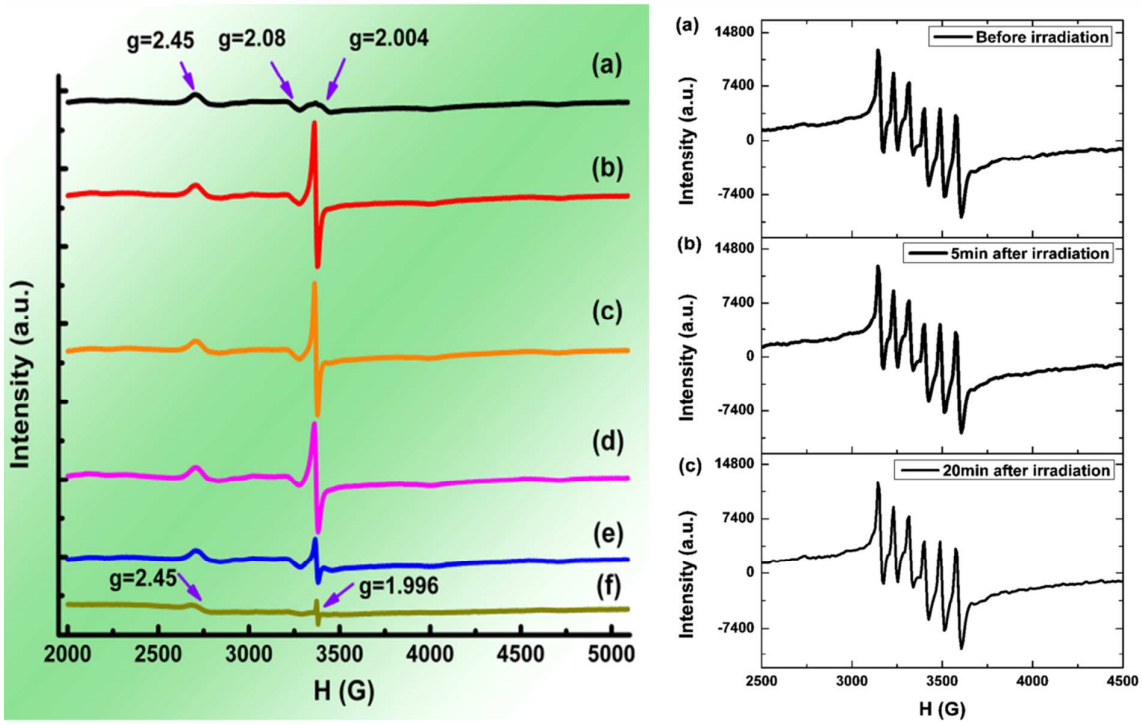

Fig. 10 (left) Electron spin resonance spectra of $Zn_3Ga_2SnO_8$: 0.5 Cr^{3+} (a-e) and $Zn_3Ga_2GeO_8$: 0.5 Cr^{3+} (f) powders measured at 100 K, (a) Before irradiation, (b-e) 0.5, 6, 24, 96 h after the stoppage of irradiation, (f) 96 h after the stoppage of irradiation. Two phosphors were pre-irradiated by a Xenon lamp for 5 min. (right) Electron spin resonance spectra of sample $LaAlO_3$: Mn^{4+} measured at 100 K: (a) before irradiation, and (b) 5, (c) 20 after the stoppage of irradiation; the samples were pre-irradiated by a xenon lamp for 10 min.

French scientists from UPMC laboratory also made a great effort to develop the afterglow mechanism by investigating the EPR signals of transition metal ions, (Cr^{3+}, Mn^{2+}, *etc.*)[49, 147-149]. EPR spectra of NIR $CaMgSi_2O_6$: Mn diopsides displayed a central set of 6 hyperfine lines (g=2) corresponding to the Mn^{2+}.[149] Subsequently, they investigated the experimental X-band (9.4 GHz) EPR spectra of Cr-doped $ZnGa_2O_4$ phosphors. They pointed out that g-factors, g=1.976 should be ascribed to the Cr^{3+}-Cr^{3+} pairs (a transition between effective Ms = ±1/2 states in the $^4A_2$ ground state of Cr^{3+} ions with C_3 crystal field axis perpendicular to the magnetic field).[147]

Su *et al*. observed the long lasting phosphorescence in Eu^{2+}-activated MO-B_2O_3 (M=Ca, Sr, and Ba) glasses. They showed that a new light-induced EPR signal was brought after the excitation, and the value of the g-factor (2.0013, 1.9947, and 2.0022, respectively) are smaller than 2.0023. Therefore, they assigned the EPR signals in Eu^{2+}-activated glasses to the electron-trapping center.[153] They also investigated the EPR spectra of $Zn_2P_2O_7$: Tm^{3+}, Mn^{2+} phosphors. Two weak EPR signals at g=2.031 and g=1.997 are assigned to holes trapped by V'_{Zn} and electrons captured by $Tm^{\bullet}_{Zn}$, respectively.[150]

4.2 Photocurrent/ photoconductivity

Photoconductivity is an optical and electrical phenomenon in which a material becomes more electrically conductive due to the absorption of electromagnetic radiation such as visible light, ultraviolet light, infrared light, or gamma radiation. When light is absorbed by a material, the number of free electrons and holes increases and raises its electrical conductivity. To cause excitation, the light that strikes the semiconductor must have enough energy to raise electrons across the band gap, or to excite the impurities within the band gap. Photocurrent is the electric current that flows as a result of a photoconductivity or a photovoltaic effect.

The photocurrent discussed here is not related to the photovoltaic effect, but concern the generation, migration and recombination of free carriers in conduction band and valence band, i.e. photoconductivity.

Photoconducting materials could be divided into two classes: idiochromatic and allochromatic (Fig. 11a). Idiochromatic materials are those which show photoconductivity when are in a pure condition, the photoconductivity being associated directly with the intrinsic properties of the material itself. Such materials exhibit photoconductivity when energy is absorbed by the atoms of the crystal, but in general show a maximum photosensitivity at the wavelength corresponding to the minimum energy required producing a free electron (the intrinsic absorption edge). Allochromatic materials are those in which the photoconductivity is associated directly with impurities or with crystal imperfections such as vacancies. The photoconductivity associated with absorption in the characteristic band of the F center in alkali halides is typical of allochromatic behavior. The absorption band and the corresponding photoconductivity excitation spectra are very similar to each other.

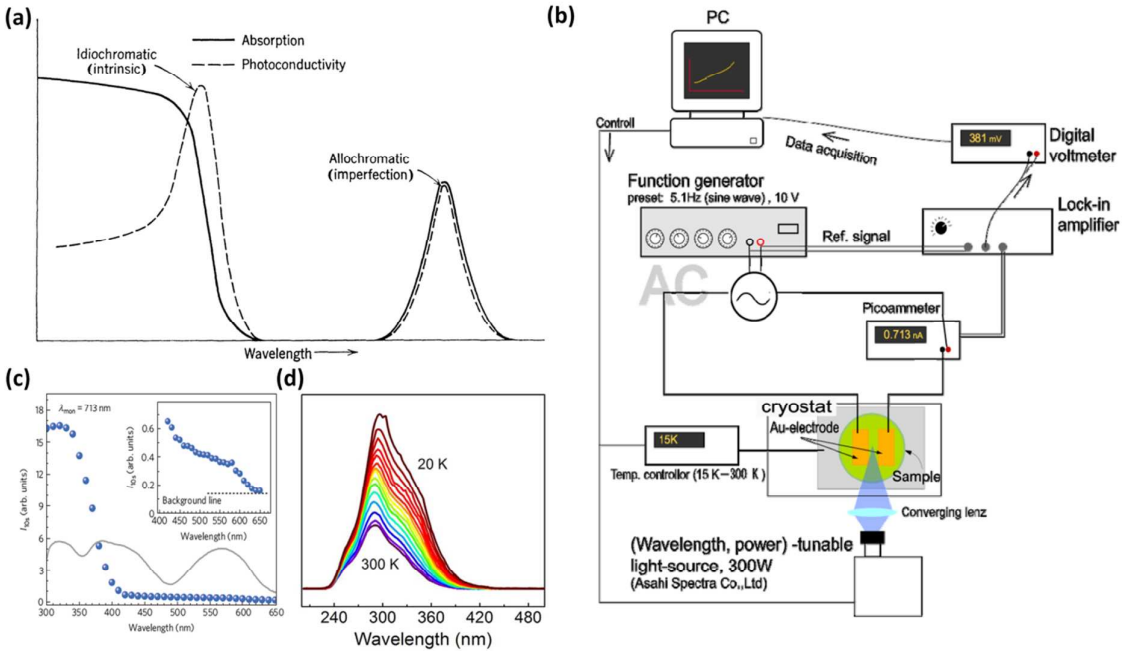

Fig. 11 (a) Wavelength dependence of absorption and photoconductivity for an idiochromatic effect (intrinsic) or an allochromatic effect (imperfection). (b) Schematic diagram of photocurrent measurement system as functions of temperature and excitation wavelength. All the equipments were controlled by the PC program automatically. (c) Afterglow intensity I_{10s} monitored at 713nm of $Zn_3Ga_2Ge_2O_{10}$: Cr as a function of the excitation wavelengths over the 300–650nm spectral range. The inset shows an enlargement of the 400 to 650nm region. The grey line shows the excitation spectrum monitored at 713 nm (reproduced with permission from ref. 12, copyright 2012, Nature Publication Group). (d) Temperature-dependent photocurrent excitation spectra of $Zn_3Ga_2Ge_2O_{10}$: Cr for the range of 20-300K.

The incorporation of defects in a photoconductor crystal may have one or more of the following effects: (1) Change the conductivity; (2) Change the photosensitivity, imperfections which act as efficient recombination centers decreasing the sensitivity; (3) Change the speed of response (imperfections which act as trapping centers, or which increase the sensitivity, decrease the speed of response); (4) Extend the spectral response. Quantitatively the location and density of defect levels may be determined by one or more of the following experimental measurements: (1) The variation of free-carrier density with temperature; (2) The appearance of new absorption, associated with direct absorption by the imperfection centers; (3) The appearance of new photoconductivity excitation bands, associated with direct ionization of imperfection centers; (4) The appearance of new luminescence emission bands, corresponding to radiative recombination transitions involving the imperfection centers; (5) The appearance of new luminescence excitation bands, associated with direct excitation of imperfection centers; (6) The dependence of the measured carrier lifetime on carrier density, when the imperfection centers act as recombination centers; (7) The appearance of new peaks in curves of thermally stimulated current (TSC), or TL emission. The increased conductivity or luminescence emission obtained when a pre-excited crystal is heated release trapped carriers can be used to

determine the ionization energies of the trapping centers.

Photoconductivity curves (or photoconductivity excitation curves) could be used to identify the traps species and the possible trapping and detrapping process. Prof S. Tanabe and co-workers from Kyoto University developed an automatic measurement system of photoconductivity in inorganic phosphors. Through this system, the wavelength and temperature-dependence of photocurrents could be measured automatically (Fig. 11b).[17] The numerical value of photocurrents were measured and recorded as a function of temperature and excitation-wavelength automatically. They investigated the photocurrent features of $SrAl_2O_4$: Eu^{2+}, $SrAl_2O_4$: Eu^{2+}, Dy^{3+} and $CaTiO_3$: Pr^{3+}, *etc.*[154, 155] Excitation wavelength dependence of photocurrent showed a similar profile to the PLE spectrum of Eu^{2+}. The result clearly indicated the interaction between 5d level of Eu^{2+} with the conduction band. The activation energy of photocurrent was evaluated from its temperature dependence for each wavelength. While most of 5d levels of Eu^{2+} at the Sr site with weak crystal field were located within the conduction band, only 5d levels of Eu^{2+} above 3.1 eV (400nm) at the Sr site with strong crystal field were located within the conduction band.[156]

NIR long phosphorescent phosphor, $Zn_3Ga_2Ge_2O_{10}$: Cr^{3+}, could be excited by ultraviolet and visible light, revealing that some shallow traps are near the CB while some ones are far away from the CB (Fig.11c).[12] The corresponding photocurrent excitation spectra were provided in Figure. 11d. Depending on distance between the traps and conduction band, only one excitation peak responsible for the electrons released from the shallow traps near the conduction band could be observed in the photocurrent excitation spectra. The photocurrent single maybe correspond to the intrinsic defects in $Zn_3Ga_2Ge_2O_{10}$: Cr^{3+}.[15]

4.3 Positron annihilation lifetime spectroscopy

Up to now, there have been few reports on an accurate description for trap concentrations. It is explored that positron annihilation lifetime spectroscopy has a tremendous potential as a powerful tool for quantifying the types and densities of defects in solids. Positron lifetime τ is a function of the electron density at the annihilation site. Positron lifetime τ is inversely proportional to the local electron density at the site of positron annihilation. Positrons are trapped in open-volume defects, such as in vacancies and their agglomerates, the positron lifetime τ can increase with respect to the defect-free sample; owing to the locally reduced electron density of the defect. Thus, a longer lifetime component, which is a measure of the size of the open volume, appears. The strength of this component, i.e. its intensity, is directly related to the defect concentration. In principle, both items of information, i.e. the kind and concentration of the defect under investigation, can be obtained independently by a single measurement. This is the major advantage of positron lifetime spectroscopy compared with angular correlation of annihilation radiation or Doppler-broadening spectroscopy with respect to defect issues.

Time-dependent positron decay spectrum M(t) is given by:

$$M(t) = \sum_{i=1}^{k+1} I_i \exp\left(-\frac{t}{\tau_i}\right) \quad (1)$$

$$\kappa = \mu C \quad (2)$$

Where, τ_i is the lifetime of every component after decomposing the positron decay spectrum using an analysis program, *Ii* the strengths with the different components, *C* the concentrations of defects and κ the annihilation probability of the positron in one defect. Thus, τ_i gives information on the types of defect. The strength of this component *Ii*, and the captured probability κ are in direct proportion to the defect concentration.

Table 3. Parameters of positron annihilation lifetime spectroscopy.

Composition	τ_1 (ns)	τ_2 (ns)	I_1 (%)	I_2 (%)	κ (ns^{-1})
GZG	0.324	1.7	80.05	15.95	3.086
SZG	0.38	1.964	65	35	17.241

Our group systematically investigated the trap concentrations of Cr-doped gallates ($Zn_3Ga_2GeO_8$: Cr, SZG and $Zn_3Ga_2SnO_8$: Cr, GZG) by the measurement of positron annihilation lifetime spectroscopy.[62] The decomposition results of SZG and GZG powders were shown in Table 3. Short lifetime component τ_1 reflected the characteristics of free-state annihilation for the perfect crystal lattice. Long lifetime component τ_2 was attributed to combined effect of positrons annihilating in vacancy-type defects, mainly including the cationic deficiency, oxygen vacancy and interfaces. Inconspicuous variations in the lifetime components τ_1 and τ_2 between two phosphors further provided a proof of similarity in traps. But the intensity I_2 and the captured probability κ of SZG powders were both superior to those of GZG powders, showing the total concentration of vacancies in SZG powders is higher than those in GZG powders.

4.4 X-ray Absorption Spectroscopy

X-ray absorption spectroscopy (XAS) is a widely used technique for determining the local geometric and electronic structure of matter. The experiment is usually performed with synchrotron radiation sources, which provide intense and tunable X-ray beams. XAS data are obtained by tuning the photons' energy to a range where core electrons can be excited. X-ray absorption spectra are especially sensitive to the formal oxidation state, coordination chemistry and distances, coordination number and species of the atoms surrounding the selected element. XAS includes both "Extended X-Ray Absorption Fine Structure" (EXAFS) and "X-ray Absorption Near Edge Structure" (XANES). Generally speaking, XANES spectra include three parts: pre-edge, edge and near-edge (Fig. 12a). EXAFS spectra are displayed as graphs of the absorption coefficient of a given material versus energy, typically in a 150-1000eV range beginning before an absorption edge of an element in the sample. This region usually shows the largest variations in the x-ray absorption coefficient and is often dominated by intense, narrow resonances. It is notable that XANES is strongly sensitive to formal oxidation state and coordination chemistry (e.g., octahedral, tetrahedral coordination) of the absorbing atom, while the EXAFS is used to determine the distances, coordination number, and species of the neighbors of the absorbing atom.

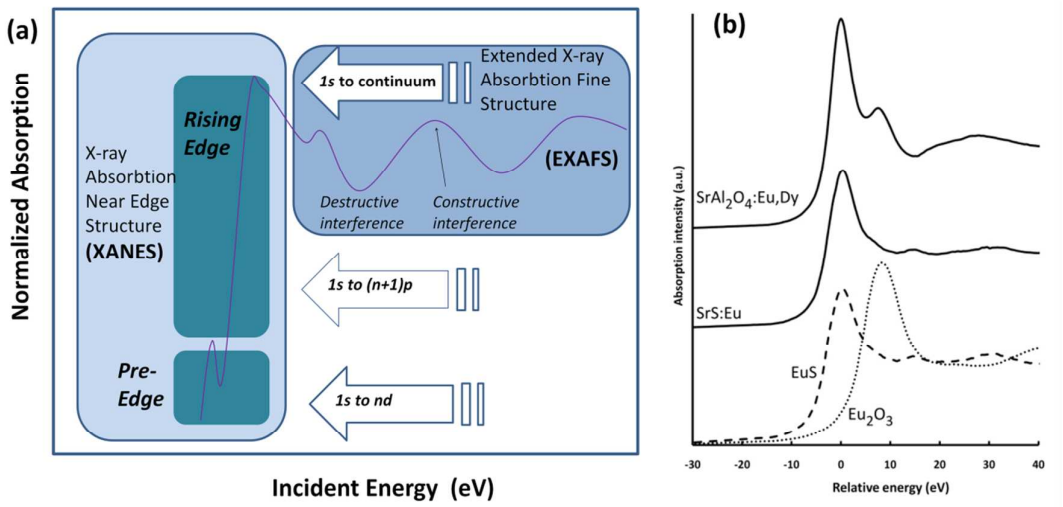

Fig. 12 (a) Three regions of XAS data. (b) Eu L_{III} XANES spectra of $SrAl_2O_4$: Eu, Dy at 120 K and SrS: Eu. EuS and Eu_2O_3 were measured as reference compounds. The spectra are shifted vertically for clarity (reproduced with permission from ref. 66, copyright 2011, American Physical Society).

The interpretation of XANES is complicated due to the fact that there is not simple analytic description of XANES. Still, there is much chemical information from the XANES region, notably formal valence (very difficult to experimentally determine in a nondestructive way) and coordination environment. Though the lack of a simple analytic expression complicates XANES interpretation, XANES can be described qualitatively (and nearly quantitatively) in terms of (a) Coordination chemistry: regular, distorted octahedral, tetrahedral coordination, as for Cr, Fe, Ti, *etc*. (b) Molecular orbitals: p−d orbital hybridization, crystal-field theory, and so on. (c) Band-structure: the density of available electronic states. (d) Multiple-scattering: multiple bounces of the photo-electron.

An important and common application of XANES is to use the shift of the edge position to determine the valence state (Fig. 12b). For ions with unfilled d-electrons bands, the orbit hybridization is dramatically altered depending on the coordination environment, which much stronger hybridization for tetrahedral coordination than for octahedral coordination. Prof. Holsa from university of Turku and co-workers has the experience in identifying the transient species in the charging and discharging persistent phosphorescence process by using this technique (Fig. 13a).[30] They explained the task of emission center (Eu^{2+}, *etc.*) and the other co-doping R ions ($R^{2+}/R^{3+}/R^{4+}$) in the mechanism of persistent phosphorescence of different LPPs, such as, $CdSiO_3$: R^{3+} (R=La–Lu, excluding Pm),[23] ZrO_2: Yb^{3+}, Er^{3+},[157] $M_2MgSi_2O_7$: Eu^{2+}, R^{3+} (M= Ca, Sr and Ba, R= Ce, Dy and Yb),[158] $SrAl_2O_4$: Eu^{2+}, R^{3+} (R= La, Ce, Nd, Sm and Yb),[158] $BaAl_2O_4$: :Eu^{2+},R^{3+},[159] by employing XANES. In line with the experimental observations of $CdSiO_3$: R^{3+} (R=La–Lu, excluding Pm), the in situ synchrotron radiation XANES spectra indicated the presence of only the trivalent Pr^{3+} and Tb^{3+} species thus excluding the direct $R^{3+}\rightarrow R^{4+}$ oxidation during the charging process of persistent phosphorescence.[23]

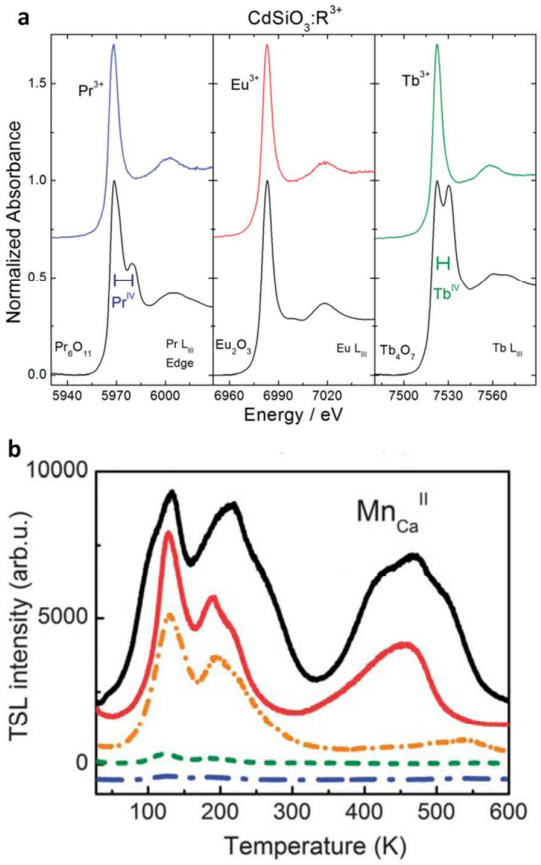

Fig. 13 (a) Rare earth L_{III} edge XANES spectra of $CdSiO_3$ doped with selected R^{3+} (reproduced with permission from ref. 23, copyright 2014, Royal Society of Chemistry). (b) Emission of Mn^{II}_{Mg} at 685 nm and (b) emission of Mn^{II}_{Ca} at 585 nm. s (reproduced with permission from ref. 149, copyright 2012, Royal Society Of Chemistry).

For Eu^{2+}-activated LPPs, XANES results at room temperature showed different results about the valence state of emission centers. Both Eu^{2+} and Eu^{3+} were presented in the XANES spectra of Eu singly doped and co-doped $Ca_2MgSi_2O_7$: Eu^{2+}, R^{3+}, $Sr_2MgSi_2O_7$: Eu^{2+}, R^{3+}, as well as $SrAl_2O_4$: Eu^{2+}, R^{3+} phosphors. But for $CaAl_2O_4$: Eu^{2+}, R^{3+}, the co-doped phosphors all contained Eu^{2+} and Eu^{3+} species, while Eu singly doped material only had Eu^{2+} in their XANES spectra. On the other hand, XANES results also offered some important information on the valence state of co-dopants. XANES measurements of $BaAl_2O_4$: Eu^{2+}, R^{3+}, confirmed the presence of only the trivalent form of the co-dopants R^{3+}.[158, 159] Dy and other co-dopants in Eu^{2+}-activated LPPs were considered only as trivalence, suggesting that no change in the co-dopant valences occured during persistent phosphorescence. P. F. Smet demonstrated the similar result by analyzing XANES results, that is, parts of the europium ions ionized from Eu^{2+} to Eu^{3+} during the charging process, and immediately Eu^{3+} turned back to Eu^{2+} after ceasing the excitation. While no any reduction or oxidation of Dy^{3+} ions were detected, indicating that

the electrons or holes could not be captured by co-dopant ions.[66] EXAFS and XANES were also employed to evidence the existence of actual defects in $CaMgSi_2O_6$: Mn^{2+} phosphors. Distinct features within the five manganese-doped diopsides were extracted from Ca K-edge and Mn K-edge EXAFS/XANES investigation. Several converging results from Ca EXAFS/XANES and Mn EXAFS evidenced the formation of oxygen vacancies, which were not in the first neighboring position with respect to manganese ions (Fig. 13b).[149]

4.5 Thermo-luminescence and its excitation spectra

Thermo-luminescence (TL) techniques are usually employed to give an estimate for the trap depth. TL is defined as the emission of light during heating of a solid following the previous absorption of energy during irradiation. The alternative radiation source is high energy ray (X-ray, gamma-ray), ultraviolet-visible-infrared light and electron beam. In fact, this radiation is the store of energy; whereas the heating is just a trigger to help release the absorbed energy. Irradiation source, irradiation duration, interval after ceasing the irradiation and environmental temperature all influence the electrons distribution in different traps (from shallow traps to deep traps).[160, 161]

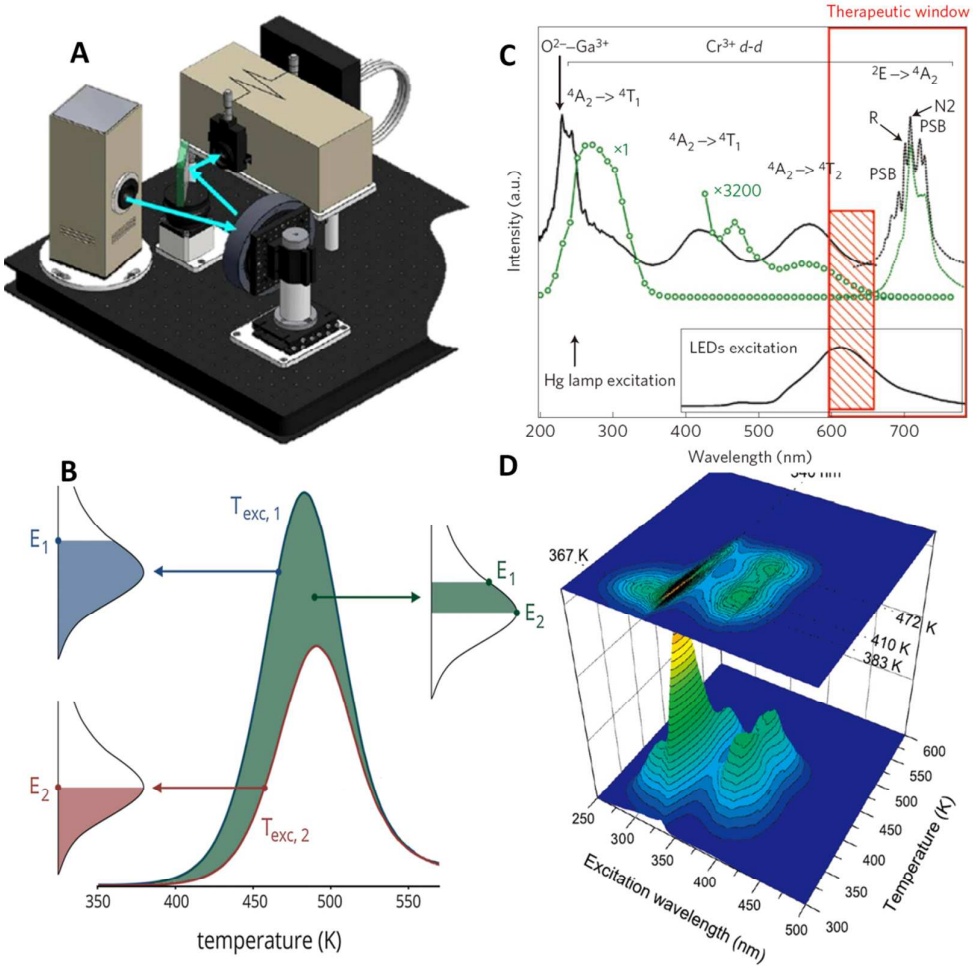

Fig. 14 (A) 3D drawing of the TL excitation part of the set-up with the Xe-lamp, focusing mirrors, monochromator, shutter, and optical fiber (reproduced with permission from ref. 162, copyright 2011, Elsevier). (B) The density of the continuous trap depth distribution at a certain depth can be estimated from the difference between the integrated intensities at two different excitation temperatures. (reproduced with permission from ref. 166, copyright 2013, American Physical Society). (C) PL excitation (black solid line) and emission (black dotted line) spectra, compared with TSL excitation (green open points) and emission (green dotted lines) spectra of Cr^{3+} doped n-$ZnGa_2O_4$. (reproduced with permission from ref. 11, copyright 2014, Nature Publication Group). (D) TL intensity of ZnS: Cu^+ as a function of excitation wavelength and temperature as contour plot (top) and in 3D representation (bottom) (reproduced with permission from ref. 162, copyright 2011, Elsevier).

By performing a series of TL experiments with varying excitation duration and at varying excitation temperature, and employing the initial rise analysis method, the depth and shape of trap distribution can be estimated (Fig. 14B).[163] Smet *et al.* pointed out that the main steps should be taken for such a trap depth

probing: (a) Measuring the thermal quenching of the sample in order to properly correct the TL data. (b) Measuring the dose dependence of the TL glow curves to verify the presence of higher order kinetics. (c) Measuring the TL glow curves after exciting at various temperatures (T). The initial rise analysis can be performed to estimate the trap depths. An estimated trap depth which varies continuously as a function of T is a strong indication for the presence of a continuous trap depth distribution. (d) If the trapping process is not thermally activated, the area under the glow curves obtained in (c) can be used to estimate the shape of the continuous trap depth distribution. If thermal activation of the trapping is seen, the areas should first be corrected for this.[164-166]

Apart from TL spectra, if we plot the integrated TL signal intensity as a function of excitation wavelength, we will get a TL excitation (TLE) spectrum (Fig. 14D). Adrie J.J. Bos *et al.* presented their TLE facility (Fig. 14A).[162, 167] In detailed, the tunable monochromatic UV-VIS light was used to excite the electrons into the conduction band. The created free electrons would be captured in intrinsical or introduced trapping centers of the sample. Traps were subsequently read out by heating the sample while the TL was recorded. By varying the monochromatic wavelength, repeating the TL read-out, and displaying the temperature integrated TL yielded as a function of the subsequent wavelengths, the TLE spectrum was obtained.

Bessiere *et al*. showed a distinctive application of TLE spectra, i.e. analyzing the attribution of PLE band by the comparison of TLE spectra and PLE spectra. The total area of each glow curve was reported as well as TSL excitation intensity of Cr^{3+}-doped $ZnGa_2O_4$ phosphors (red open circles in Fig. 14C). TSL excitation spectrum was divided into five wavelength ranges. By comparing the PLE and TLE spectra, the former four ranges should be assigned to the $^4A_2 \rightarrow {}^4T_2(4F)$ of Cr^{3+}, the $^4A_2 \rightarrow {}^4T_1(4F)$ transitions of Cr^{3+}, the $^4A_2 \rightarrow {}^4T_1(4P)$ transitions of Cr^{3+}, band-to-band transition, respectively.[11]

In addition to PLE band, TLE measurements also could be used to identify the afterglow excitation band. For example, the broad 320-380nm TLE band corresponded to $5d_2$ and $5d_3$ bands of Ce^{3+} by analyzing the TLE spectra of $Sr_{2.98}Al_{0.02}Si_{0.98}O_5$: $0.01Ce^{3+}$, $0.01Dy^{3+}$.[131] Figure 15 showed a representative 3D TLE spectra (the TL excitation contour plots for $M_2Si_5N_8$: Eu (M=Ca, Sr, Ba) phosphors.[164] TLE band located round 260 nm, which also corresponded to the most effective afterglow excitation band. Now, this technique have been widely applied in the study of afterglow excitation band of LPPs, such as Lu_2SiO_5: Ce^{3+}, $SrAl_2O_4$: Eu^{2+}, Dy^{3+}, $Sr_4Al_{14}O_{25}$: Eu^{2+}, Dy^{3+},$CaAl_2O_4$: Eu^{2+}, Nd^{3+}, $M_2Si_5N_8$: Eu (M=Ca, Sr, Ba) and the classical ZnS: Cu^+ LPPs. The $SrAl_2O_4$: Eu^{2+}, Dy^{3+}, $Sr_4Al_{14}O_{25}$: Eu^{2+}, Dy^{3+}, $CaAl_2O_4$: Eu^{2+}, Nd^{3+}, and ZnS: Cu^+ phosphors exhibit the TLE spectra with maxima at 300-360 nm, 380-420 nm, 300-400 nm, 330 nm in accordance with the previous reports about the PLE and diffuse reflection spectra.[27, 131, 150, 168-170]

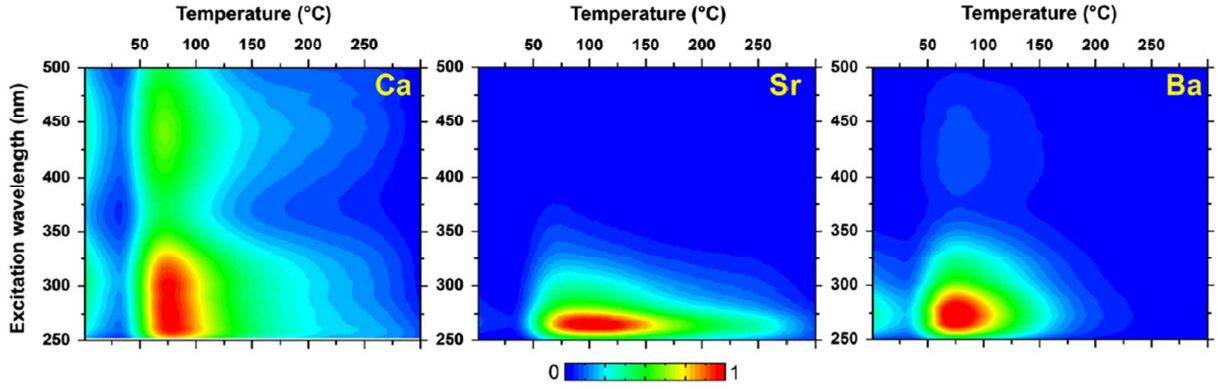

Fig.15 Normalized TL excitation contour plots for $M_2Si_5N_8$: Eu (M=Ca, Sr, Ba) excited at room temperature (reproduced with permission from ref. 164, copyright 2012, Elsevier).

4.6 UV-VUV synchrotron radiation emission and excitation spectroscopy

Vacuum ultraviolet-ultraviolet (UV-VUV) synchrotron radiation emission and excitation spectroscopy is a powerful tool in investigating the relationships between energy levels of (co-)dopants and electronic host band structure. By using this route, the f-d transition and charge transfer energy of rare earth ions, and the relation with the band gap of compounds can be identified. Holsa *et al.* estimated the band gap of non-doped $CdSiO_3$

materials by using UV-VUV synchrotron radiation excitation spectroscopy. In this excitation spectrum, a sharp edge was observed at 230 nm (5.4 eV).[23] Since $CdSiO_3$ host did not contain any emitting ion, this edge could only be the excitation from the top of the VB to the bottom of CB, i.e. the band gap energy. The similar method is also used to estimate the band gap of non-doped hosts in $SrAl_2O_4$: Eu^{2+} (6.6eV), $Sr_2MgSi_2O_7$: Eu^{2+} (7.1eV), ZrO_2: Yb^{3+}, Er^{3+} (5.3eV), $BaAl_2O_4$: Eu^{2+}, Dy^{3+} (6.5 eV), $CaAl_2O_4$ (6.84 eV), $CaAl_2O_4$: Eu^{2+} (6.74 eV) LPPs.[30, 132, 159, 171]

5. Classifications

In this part we review the recent developments of LPPs and discuss the classification of LPPs. Such developments follow two directions: materials and operational wavebands. First we make a full list of most popular LPPs in Table 4 to 14. With few exceptions, the fabrication of most of these listed LPPs is reported after 2009, the year when the new NIR LPPs are synthesized and *in vivo* imaging method using phosphorescent nanoparticles as the bio-labels is proposed. The number of related activators and hosts is expected to highly increase in the coming years. In addition to materials, another important research direction is extending the emission and excitation waveband to longer-wavelength region. Especially for the emission waveband, this subject is a critical issue, to promote the development of bio-labels with LPP. The related strategies about realizing the goal of longer-wavelength emitting also discussed. That is, varying the activators, modulating the crystal field and transferring the persistent energy from one activator to another.

Table 4. Binary oxide-based long phosphorescent phosphors. “ET” means the energy transfer; “CE” means the coherent excitation; “ICE” means the incoherent excitation; “HR” means the excitation of High Energy Rays; “UV” means ultraviolet excitation; “Vis” means visible excitation; “NIR” means near-infrared excitation; “E” means “observed by eye”; “M” means “the detection intensity reach to 0.032mcd/m^2”; “R” means “response of spectrometer’ detector ”.

Host Materials	Activator	Co-dopant	Afterglow (band)/[peak] (color) (nm)	Excitation band/[peak] (nm)	Afterglow duration (E,M,R)	Reference
CaO	Eu^{3+}		[594, 616] (reddish orange)	[254] (UV) <ICE>	[2h] R	172
Lu_2O_3	Eu^{3+}		[528, 611] (reddish orange)	[X-ray] (HR) <HR>	[60min] R	173
SnO_2	Sm^{3+}	Zr^{4+}	(550-700) (red)	[254] (UV) <ICE>	[900s] R	104
ZrO_2	Sm^{3+}	Sn^{4+}	(550-700) (red)	[254] (UV) <ICE>	[900s] R	161
Lu_2O_3	Pr^{3+}	Hf^{2+}	[610, 631] (red)	[X-ray] (HR) <HR>	[200s] R	169, 174
Lu_2O_3	Tb^{3+}	Ca^{2+}, Sr^{2+},	[543] (green)	[270] (UV) <ICE>	[20-30h] E	175
ZrO_2	Er^{3+}	Yb^{3+}	(630-720) [650] (red)	[980] (NIR) <CE>	[16 ms] R	157
Ga_2O_3	Cr^{3+}		(650-850) [713] (NIR)	[300] (UV) <ICE>	[4h] R	75, 176
ZrO_2	Ti^{3+}		(350-700) [496] (bluish-green)	[300] (UV) <ICE>	[800s] R	177

Table 5. Silicate-based long phosphorescent phosphors.

Host Materials	Activator	Co-dopant	Afterglow (band)/[peak] (color) (nm)	Excitation band/[peak] (nm)	Afterglow duration (E,M,R)	Reference
$Ba_{13}Al_{22}Si_{10}O_{66}$	Eu^{2+}		(350-700) (blue)	[365] (UV) <ICE>	[43.5 min] R	178
$Sr_3MgSi_2O_8$	Eu^{2+}	Dy^{3+}	[460] (blue)	[254] (UV) <ICE>	[10 h] R	133
$Sr_3Al_{10}SiO_{20}$	Eu^{2+}	Ho^{3+}	[465] (blue)	[365] (UV) <ICE>	[6h] M	179
$Ca_3MgSi_2O_8$	Eu^{2+}	Dy^{3+}	[470] (blue)	[standard lamp] <ICE>	[5h] M	180
$Sr_2MgSi_2O_7$	Eu^{2+}	Dy^{3+}	[470] (blue)	[254] (UV) <ICE>	[10 h] M	181
$Ba_4(Si_3O_8)_2$	Eu^{2+}	Er^{3+}	[481] (blue)	[365] (UV) <ICE>	[2500s] E	182
$Ba_4(Si_3O_8)_2$	Eu^{2+}	Dy^{3+}	(400-700) (bluish-green)	[365] (UV) <ICE>	[24 h] M	44
$Ba_4(Si_3O_8)_2$	Eu^{2+}	Ho^{3+}	[496] (green)	[390] (UV) <ICE>	[4 h] E	183
$Sr_2Al_2SiO_7$	Eu^{2+}	Dy^{3+}	[485] (blue-green)	[365] (UV) <ICE>	[2h] E	184
$Ba_2MgSi_2O_7$	Eu^{2+}	Tm^{3+}	[505] (green)	[355] (UV) <ICE>	[5 h] M	185
$BaMgSiO_4$	Eu^{2+}		[537] (green)	[310] (UV) <ICE>	[1.5 h] M	186

$Ca_2MgSi_2O_7$	Eu^{2+}		[535] (green)	[Xe lamp] <ICE>	[12 h] M	187
$CaAl_2Si_2O_8$	Eu^{2+}	Pr^{3+}	(375-600) (green)	[365] (UV) <ICE>	[2h] R	188, 189
Sr_2SiO_4	Eu^{2+}	Dy^{3+}	[570] (yellow)	[160,310] (UV) <ICE>	[60,10min] R	57, 190
Sr_3SiO_5	Eu^{2+}	Lu^{3+}	[574] (yellow)	[365] (UV) <ICE>	[20h] M	191, 192
$Ca_2ZnSi_2O_7$	Eu^{2+}	Dy^{3+}	[580] (yellow)	[460] (UV) <ICE>	[12h] E	193
$MgSiO_3$	$Eu^{2+}\rightarrow Mn^{2+}$ (ET)		[665] (Red)	Mercury lamp(UV) <ICE>	[4h] R	194
$Sr_3MgSi_2O_8$	$Eu^{2+}\rightarrow Mn^{2+}$(ET)		[457,670] (red)	[375] (UV) <ICE>	[2h] R	195
$Ca_{0.2}Zn_{0.9}Mg_{0.9}Si_2O_6$	$Eu^{2+}\rightarrow Mn^{2+}$(ET)		(600-800) (NIR)	[340] (UV) <ICE>	[1h] R	85
$CaAl_2Si_2O_8$	$Eu^{2+}\rightarrow Mn^{2+}$(ET)	Dy^{3+}	[418,580] (white)	[365] (UV) <ICE>	[1h] R	196, 197
Lu_2SiO_5	Ce^{3+}		[400,430] (blue)	[355] (UV) <ICE>	[3h] R	198
$Ca_2Al_2SiO_7$	$Ce^{3+}\rightarrow Mn^{2+}$(ET)		550 (green)	Mercury lamp(UV) <ICE>	[10h] M	199
$Sr_2Al_2SiO_7$	$Ce^{3+}\rightarrow Dy^{3+}$(ET)		[408,491,573] (white)	[343] (UV) <ICE>	[1 h] M	184
$CaMgSi_2O_6$	Dy^{3+}		[480,575,667] (white)	[343] (UV) <ICE>	[2h] R	200, 201
$Ca_xMgSi_2O_{5+x}$(x= 1,2,3)	Dy^{3+}		[475,580] (white)	[254] (UV) <ICE>	[1h] E	58, 200
$Ca_2MgSi_2O_7$	Dy^{3+}		[458,580,660,755] (white)	[254] (UV) <ICE>	[3 h] E	200, 202
Sr_2SiO_4	Dy^{3+}		[480,575,665] (white)	[254] (UV) <ICE>	[1h] M	203
$Gd_{9.33}(SiO_4)_6O_2$	Sm^{3+}		[606] (red)	[273] (UV) <ICE>	[1400s] R	204
$Sr_2ZnSi_2O_7$	Sm^{3+}		[561,598,644] (red)	[254] (UV) <ICE>	[30 min] M	205
$CdSiO_3$	Mn^{2+}	Nd^{3+}	[587] (yellow)	[254] (UV) <ICE>	[300s] R	206
$CdSiO_3$	Bi^{3+}		[360] (UV)	[221] (UV) <ICE>	[60s] R	122, 207
$CdSiO_3$	defect	Gd^{3+}	[435] (blue)	[Xe lamp] <ICE>	[5h] R	23
	defect$\rightarrow Tb^{3+}$ (ET)		[545] (green)	[Xe lamp] <ICE>	[5h] R	23
	defect$\rightarrow Sm^{3+}$(ET)		(530-680) (red)	[Xe lamp] <ICE>	[5h] R	23
	defect$\rightarrow Pr^{3+}$(ET)		(580-680) (red)	[Xe lamp] <ICE>	[5h] R	23
	defect$\rightarrow Dy^{3+}$(ET)		[480, 580] (white)	[Xe lamp] <ICE>	[5h] R	23
$CaSnSiO_5$	defect		[420] (Purple Blue)	[312] (UV) <ICE>	[200s] R	208
	defect$\rightarrow Tb^{3+}$(ET)		[486,542] (green)	[312] (UV) <ICE>	[4600s]R	208
	defect$\rightarrow Sm^{3+}$(ET)		[600] (orange)	[312] (UV) <ICE>	[700s] R	208
	defect$\rightarrow Dy^{3+}$(ET)		[482,572] (white)	[312] (UV) <ICE>	[3600s]R	208
$Ca_3SnSi_2O_9$	defect		[426] (blue)	[316] (UV) <ICE>	[700s] R	209
	defect$\rightarrow Pr^{3+}$(ET)		[488] (green)	[316] (UV) <ICE>	[1200s] R	209
	defect$\rightarrow Sm^{3+}$(ET)		[600] (orange)	[316] (UV) <ICE>	[1200s] R	209
	defect$\rightarrow Dy^{3+}$(ET)		[572] (white)	[316] (UV) <ICE>	[1200s] R	209
$Ca_2ZrSi_4O_{12}$	defect		[490] (green)	[254] (UV) <ICE>	[4800s] M	144
	defect$\rightarrow Sm^{3+}$(ET)		[616] (orange)	[254] (UV) <ICE>	[843s] M	144

Table 6. Aluminate-based long phosphorescent phosphors.

Host Materials	Activator	Co-dopant	Afterglow band/[peak] (nm)	Excitation band/[peak] (nm)	Afterglow duration (E,M,R)	Reference
$CaAl_2O_4$	Eu^{2+}	Nd^{3+}	440 (blue)	[350] (UV) <ICE>	[5h] M	124
$Sr_4Al_{14}O_{25}$	Eu^{2+}	Dy^{3+}	(490) (blue)	[365] (UV) <ICE>	[20h] R	210
$SrAl_2O_4$	Eu^{2+}	Dy^{3+}	520(green)	[365] (UV) <ICE>	[30 h] R	124
$BaAl_2O_4$	Eu^{2+}	Dy^{3+}	500(green)	[365] (UV) <ICE>	[2h] R	16

$Sr_4Al_{14}O_{25}$	Eu^{2+}→Cr^{3+}(ET)	Dy^{3+}	[495,695] (green, NIR)	[Xe lamp] <ICE>	[10h,20min] R	211
$SrAl_2O_4$	Eu^{2+}→Er^{3+}(ET)	Dy^{3+}	[525,1530] (green,NIR)	[Xe lamp] <ICE>	[100min] R	113
$SrAl_2O_4$	Eu^{2+}→Nd^{3+}(ET)	Dy^{3+}	[515,882] (green,NIR)	[370] (UV) <ICE>	[15min] R	212
$CaAl_4O_7$	Ce^{3+}		[325,420] (Purple Blue)	[254] (UV) <ICE>	[10h] M	121, 213
$CaYAl_3O_7$	Ce^{3+}		[430] (blue)	[266,355] (UV) <ICE>	[1000s] R	121, 122
$Sr_4Al_{14}O_{25}$	Ce^{3+}		[472,511] (blue-green)	[γ-ray] (HR) <HR>	[600s] E	121, 122
$Y_3Al_5O_{12}$	Ce^{3+}		[520] (green)	[460] (UV) <ICE>		214
$Y_3Al_{5-x}Ga_xO_{12}$ (x=2.5-3.5)	Ce^{3+}		[505] (green)	[460] (Blue) <ICE>	[200-1000min] R	215
$Gd_3Al_2Ga_3O_{12}$	Ce^{3+}	Cr^{3+}	[540] (yellow)	[460] (Blue) <ICE>	[120min] R	216, 217
$SrAl_2O_4$	Ce^{3+}→Mn^{2+}(ET)		[375,515] (green)	[artificial light] <ICE>	[5h] R	196, 218
$CaAl_2O_4$	Ce^{3+}→Tb^{3+}(ET)		[543] (green)	[254] (UV) <ICE>	[10h] R	219
$Y_3Al_2Ga_3O_{12}$	Ce^{3+}→Cr^{3+}(ET)		[505,700] (green)	[460] (Blue) <ICE>		41, 81
$Y_3Al_2Ga_3O_{12}$	Ce^{3+}→Nd^{3+}(ET)		[808,1064,1335](NIR)	[460] (Blue) <ICE>	[10h] R	81
$CaAl_2O_4$	Tb^{3+}		[493,543,590,621] (green)	[Mercury lamp]	[1h] M	73
$Y_3Al_5O_{12}$	Pr^{3+}		[490,610] (yellow)	[240,290] (UV) <ICE>	[600s] R	220
$CaAl_2O_4$	Dy^{3+}		[477,491,577,668] (white)	[254] (UV) <ICE>	[30min] M	221
$Y_3Al_5O_{12}$	Mn^{2+}		[580] (yellow)	[254] (UV) <ICE>	[400s] R	222
$MAlO_3$(M=La, Gd)	Mn^{4+}	Ge^{4+}	(600-800) (NIR)	(250-400) (UV-VIS) <ICE>	[20h] R	151

Table 7. Gallate-based long phosphorescent phosphors.

Host Materials	Activator	Co-dopant	Afterglow band/[peak] (nm)	Excitation band/[peak] (nm)	Afterglow duration (E,M,R)	Reference
$Y_3Sc_2Ga_3O_{12}$	Ce^{3+}		[500] (Green)	[400] (UV-VIS) <ICE>	[100min] R	32, 215
$La_3Ga_5GeO_{14}$	Cr^{3+}		(700-1300) (NIR)	[240-480] (UV) <ICE>	[8h] R	31, 77, 79, 223
$Zn_3Ga_2Ge_2O_{10}$	Cr^{3+}		(650-1000) (NIR)	(300-600) (UV-VIS) <ICE>	[360h] R	12, 80
$LiGa_5O_8$	Cr^{3+}		(600-850) (NIR)	[250-350] (UV) <ICE>	[1000h] R	139, 224, 225
$SrGa_{12}O_{19}$	Cr^{3+}		(650-950) (NIR)	[254] (UV)	[2h] R	22
$MgGa_2O_4$	Cr^{3+}		(650-770) (NIR)	[X-ray] (HR) <HR>	[1200s] R	53, 95
$Zn_3Ga_2SnO_8$	Cr^{3+}		(650-1000) (NIR)	(300-600) (UV-VIS) <ICE>	[300h] R	62
$ZnGa_2O_4$	Cr^{3+}		(600-800) (NIR)	(250-600) (UV-VIS) <ICE>	[5h] R	17, 20, 49, 147, 226-228
$Ca_3Ga_2Ge_3O_{12}$	Cr^{3+}	Yb^{3+}, Tm^{3+}	(650-850) (NIR)	(250-400) (UV-VIS) <ICE>	[7000s] R	18, 229
$ZnGa_2O_4$	Mn^{2+}		[504] (green)	[352.6] (UV) <ICE>	[15min] R	74
$Zn_3Ga_2Ge_2O_{10}$	Mn^{2+}		[520] (green)	[290] (UV) <ICE>	[8h] R	230
$ZnGa_2O_4$	Bi^{3+}		[410, 550] (yellow)	[360] (UV) <ICE>	[40min] R	231

Table 8. Phosphate-based long phosphorescent phosphors.

Host Materials	Activator	Co-dopant	Afterglow band/[peak] (nm)	Excitation band/[peak] (nm)	Afterglow duration (E,M,R)	Reference
$Sr_2P_2O_7$	Eu^{2+}	Y^{3+}	[420] (Purple Blue)	[254] (UV) <ICE>	[8h] E	232
$Ca_2P_2O_7$	Eu^{2+}	Y^{3+}	[415] (Purple Blue)	[254] (UV) <ICE>	[6h] E	233
$SrMg_2(PO_4)_2$	Eu^{2+}	Tb^{3+}	[411] (Purple Blue)	[254,365] (UV) <ICE>	[1000s] R	234
$Ca_3Mg_3(PO_4)_4$	Eu^{2+}		[433] (blue)	[254] (UV) <ICE>	[1000s] R	235
$Ca_9Bi(PO_4)_7$	Eu^{2+}	Dy^{3+}	[475] (blue)	[254] (UV) <ICE>	[5h] E	236

$Zn_2P_2O_7$	Tm^{3+}		[365, 452,478] (blue)	[254] (UV) <ICE>	[1h] M	68, 150
YPO_4	Pr^{3+}	Nd^{3+}, Er^{3+}, Ho^{3+}, Dy^{3+}	[612] (orange)	[X-ray] (HR) <HR>	[1800s] R	27
$SrMg_2(PO_4)_2$	Eu^{3+}	Zr^{4+}	[500,588] (white)	[254] (UV) <ICE>	[1.5h] R	237
$Zn_3(PO_4)_2$	Mn^{2+}	Ga^{3+}	[507,620] (green, red)	[254] (UV) <ICE>	[2h] R	238
$Ca_3(PO_4)_2$	Mn^{2+}	Dy^{3+}	[660] (red)	254] (UV) <ICE>	[1h] R	52
$Ca_{9.5}Mn(PO_4)_7$	Mn^{2+}		[645] (red)	(UV) <ICE>	[1h] R	148

Table 9. Germanate-based long phosphorescent phosphors.

Host Materials	Activator	Co-dopant	Afterglow band/[peak] (nm)	Excitation band/[peak] (nm)	Afterglow duration (E,M,R)	Reference
$CaZnGe_2O_6$	Tb^{3+}		[488,552,583] (green)	[236] (UV) <ICE>	[4h] R	122
$CaZnGe_2O_6$	Dy^{3+}		(white)	[240] (UV) <ICE>	[3h] E	239
$Na_2CaSn_2Ge_3O_{12}$	Sm^{3+}		[566,605,664] (red)	[254] (UV) <ICE>	[4.8h] E	78
$CdGeO_3$	Pr^{3+}		(470-510,580-620) (red)	[254] (UV) <ICE>	[1000s] R	240
Li_2ZnGeO_4	Mn^{2+}		[530] (green)	[254] (UV) <ICE>	[8h] R	63
Zn_2GeO_4	Mn^{2+}		[528] (green)	[254] (UV) <ICE>	[2h] R	241
$Cd_2Ge_7O_{16}$	Mn^{2+}		[585] (yellow)	[258] (UV) <ICE>	[3h] R	242
$MgGeO_3$	Mn^{2+}	Bi^{3+}	[680] (red)	[254] (UV) <ICE>	[100min] R	243
$CaZnGe_2O_6$	Mn^{2+}		[648] (red)	[250] (UV) <ICE>	[3h] E	244
Zn_2GeO_4	Bi^{3+}		[455] (blue)	[254] (UV) <ICE>	[500s] R	245

Table 10. Stannate-based long phosphorescent phosphors.

Host Materials	Activator	Co-dopant	Afterglow band/[peak] (nm)	Excitation band/[peak] (nm)	Afterglow duration (E,M,R)	Reference
Ca_2SnO_4	Sm^{3+}		[566,609,633] (red)	[252] (UV) <ICE>	[1h] E	246
Sr_2SnO_4	Sm^{3+}	Dy^{3+}	[582,624,672] (red)	[254] (UV) <ICE>	[1h] E	34
$Sr_3Sn_2O_7$	Sm^{3+}		[580,621,665,735] (red)	[267] (UV) <ICE>	[1h] E	247
Ca_2SnO_4	Tm^{3+}		[468] (blue-green)	[254] (UV) <ICE>	[5h] E	80
$CaSnO_3$	Tb^{3+}		[491,545,588,622] (green)	[264] (UV) <ICE>	[4h] E	248
Ca_2SnO_4	Tb^{3+}		[483,545] (green)	[254] (UV) <ICE>	[3h] E	249
Ca_2SnO_4	Pr^{3+}		[496, 605, 625, 658] (red)	[254] (UV) <ICE>	[20min] E	250
$CaSnO_3$	Pr^{3+}		[488,541,620,653] (white)	[254] (UV) <ICE>	[3h] M	251
Ca_2SnO_4	Eu^{3+}		[617,633] (red)	[254] (UV) <ICE>	[100min] R	252
Sr_2SnO_4	Nd^{3+}		(850-1400) (NIR)	(250-450) (UV-VIS) <ICE>	[1h] R	253
Mg_2SnO_4	Ti^{4+}		[458] (blue)	[254] (UV) <ICE>	[2h] R	254, 255
Mg_2SnO_4	Mn^{2+}		[500] (green)	[254] (UV) <ICE>	[5h] M	256
Zn_2SnO_4	Cr^{3+}		(650-1200) (NIR)	(270-420) (UV-VIS) <ICE>	[35h] R	13
$SrSnO_3$	Bi^{2+}		(700-850) (NIR)	(250-400) (UV-VIS) <ICE>	[30min] R	257
Ca_2SnO_4	defect	Gd^{3+}	[410,466] (blue)	[254] (UV) <ICE>	[3h] E	258
Mg_2SnO_4	defect		[470-550] (green)	[254] (UV) <ICE>	[5h] E	204

Table 11. Niobate/titanate/zirconate/wolframate/borate-based long phosphorescent phosphors.

Host Materials	Activator	Co-dopant	Afterglow band/[peak] (nm)	Excitation band/[peak] (nm)	Afterglow duration (E,M,R)	Reference
$SrZrO_3$	Pr^{3+}		[350,499,612] (green)	[238] (UV) <ICE>	[600s] R	259
$CaTiO_3$	Pr^{3+}		[612] (orange)	[254] (UV) <ICE>	[2h] M	260
$Ca_2Zn_4Ti_{16}O_{38}$	Pr^{3+}		[614] (orange)	[380,473] (UV-VIS) <ICE>		35
$NaNbO_3$	Pr^{3+}		[620] (red)	[350] (UV) <ICE>	[40s] R	261

$CaWO_4$	Tb^{3+}		[550] (green)	[254] (UV) <ICE>	[400s] R	262, 263
$LiSr_4(BO_3)_3$	Eu^{2+}		[630] (red)	[254] (UV) <ICE>	[20min] E	264, 265
$CaWO_4$	Eu^{2+}		[618] (orange)	[254] (UV) <ICE>	[40min] E	214
$La_2Ti_2O_7$	Sm^{3+}, Ti^{4+}		[460,570,605,660] (Blue-red-white)	[254] (UV) <ICE>	[540s] M	266
$CaWO_4$	Bi^{3+}		[440] (violet)	[254] (UV) <ICE>	[1000s] R	267, 268
$BaZrO_3$	defect	Mg^{2+}	(350-500) (blue)	[275] (UV) <ICE>	[2000s] M	269
$ZnTa_2O_6$	Pr^{3+}		(590-670) (red)	(beta-ray) (HR) <HR>	[1200s] R	270

Table 12. sulfide-based long phosphorescent phosphors.

Host Materials	Activator	Co-dopant	Afterglow band/[peak] (nm)	Excitation band/[peak] (nm)	Afterglow duration (E,M,R)	Reference
SrS	Eu^{2+}	Pr^{3+}	[611] (orange)	[440] (VIS) <ICE>	[1000min] R	83, 121
CaS	Eu^{2+}	Tm^{3+}	[650] (red)	[Xe lamp] <ICE>	[1h] E	103
Ca_2SiS_4	Eu^{2+}	Nd^{3+}	[660] (red)	[320] (UV) <ICE>	[30min] R	121
Y_2O_2S	Eu^{3+}	Mg^{2+},Ti^{4+}	[590,614,627,710] (orange-red)	[365] (UV) <ICE>	[3h] R	114, 271
Gd_2O_2S	Eu^{3+}		[627] (red)	[Xe lamp] <ICE>	[600s] R	272
Y_2O_2S	Sm^{3+}	Mg^{2+},Ti^{4+}	[570,606,659] (orange)	[269] (UV) <ICE>	[2.5h] M	114
La_2O_2S	Sm^{3+}		[605,665] (red)	[Xe lamp] <ICE>	[120s] R	273
Y_2O_2S	Dy^{3+}	Mg^{2+},Si^{4+}	[486,557] (white)	[357] (UV) <ICE>	[36min] M	274
Y_2O_2S	Tm^{3+}	Mg^{2+},Ti^{4+}	[495,545,588] (yellow)	[254] (UV) <ICE>	[1h] E	275
SrS	Yb^{2+}		(550-700) (orange)	[465] (UV) <ICE>	[450s] R	82, 276
ZnS	Cu^{+}	Co^{2+}	[525] (green)	[X-ray] (HR) <HR> [360] (UV) <ICE>	[3h] R	121
Gd_2O_2S	Ti^{3+}		[590] (yellow)	[254] (UV) <ICE>	[2h] M	277
Y_2O_2S	Ti^{3+}	Mg^{2+},Gd^{3+},Lu^{3+}	(540-594) (yellow)	[Xe lamp] <ICE>	[5h] R	278

Table 13. nitride-based long phosphorescent phosphors.

Host Materials	Activator	Co-dopant	Afterglow band/[peak] (nm)	Excitation band/[peak] (nm)	Afterglow duration (E,M,R)	Reference
$SrSi_2O_2N_2$	Eu^{2+}		[539] (green)	(250-300) (UV) <ICE>	[2.5h] M	279
$BaSi_2O_2N_2$	Eu^{2+}		[498] (green)	(250-500) (UV-VIS) <ICE>	[50min] E	280
$BaAlSi_5N_7O_2$	Eu^{2+}		(400-650) (green)	[254] (UV) <ICE>	[40min] M	281
$Ca_2Si_5N_8$	Eu^{2+}	Tm^{3+}	(500-750) [620] (orange)	[420] (VIS) <ICE>	[200min] M	37, 164, 282
$SrCaSi_5N_8$	Eu^{2+}	Tm^{3+}	[647] (red)	[Xe lamp] <ICE>	[30min] M	283
AlN	Mn^{2+}		(570-700) (red)	[254] (UV) <ICE>	[1h] M	284
C_3N_4	defect		[553] (green)	[365] (UV) <ICE>	[1.5h] R	285
BCNO	defect		[520] (green)	[365] (UV) <ICE>	[2h] R	152

Table 14. Other long phosphorescent phosphors.

Host Materials	Activator	Co-dopant	Afterglow band/[peak] (nm)	Excitation band/[peak] (nm)	Afterglow duration (E,M,R)	Reference
$Sr_5(PO_4)_3Cl$	Eu^{2+}		[467] (blue)	[254] (UV) <ICE>	[1040s] M	286
$Ba_5(PO_4)_3Cl$	Eu^{2+}	Gd^{3+}	[435] (blue)	[254] (UV) <ICE>	[1000s] M	287
$Ca_8Mg(SiO_4)_4Cl_2$	Eu^{2+}		[505] (green)	[320] (UV) <ICE>	[3h] E	288
Ca_2BO_3Cl	Eu^{2+}	Dy^{3+}	[580] (yellow)	[254] (UV) <ICE>	[48h] M	25

$Sr_3Al_2O_5Cl_2$	Eu^{2+}	Tm^{3+}	[620] (orange)	[365] (UV) <ICE>	[220min] M	[26]
$Sr_5(BO_3)_3Cl$	Eu^{2+}		[610] (orange)	[254] (UV) <ICE>	[15min] R	[289]
KY_3F_{10}	Tb^{3+}		[542] (green)	(X-ray/Cathode-ray) (HR) <HR>	[108s] E	[290]
$Sr_3Al_2O_5Cl_2$	Tb^{3+}		[544] (green)	[254] (UV) <ICE>	[1h] M	[291]
$Sr_3Al_2O_5Cl_2$	Ce^{3+}		[435] (blue)	[352] (UV) <ICE>	[3h] M	[292]
$Sr_3Al_2O_5Cl_2$	Ce^{3+}→Eu^{2+}(ET)		[435,620] (orange)	[352] (UV) <ICE>	[3h] M	[287]

5.1 Activators

In LPPs, emitters are centers capable of emitting radiation after being excited, which is responsible for the emission wavebands. A wide variety of activation ions are used as luminescent centers, but when they come to persistent luminescence, the number of known activators is relatively low. Only some of rare earth ions (Ce^{3+}, Pr^{3+}, Sm^{3+}, Eu^{2+}, Eu^{3+}, Tb^{3+}, Dy^{3+}, Tm^{3+}, Yb^{2+}, Yb^{3+}, *etc.*), transition metal ions (Cr^{3+}, Mn^{2+}, Mn^{4+}, Ti^{4+} *etc.*) and main group element (Bi^{3+} *etc.*) as well as parts of crystal defects have been reported to exhibit their characteristic phosphorescence.

5.1.1 Rare earth ions

5.1.1.1 Eu^{2+} and Ce^{3+}

Eu^{2+} ion is the most famous isolated phosphorescent center. Depending on the crystal field effect (i.e., the predominantly electrostatic effect of neighboring ions onto Eu^{2+}), emission color of Eu^{2+} ion in solid state is different. The main blue LPPs activated by Eu^{2+} include $CaAl_2O_4$: Eu^{2+}, Nd^{3+},[124] $Sr_4Al_{14}O_{25}$: Eu^{2+}, Dy^{3+},[210] $Sr_2MgSi_2O_7$: Eu^{2+}, Dy^{3+},[181] $Sr_3MgSi_2O_8$: Eu^{2+}, Dy^{3+} [133]*etc.* Other $Ba_2MgSi_2O_7$: Eu^{2+}, Tm^{3+},[185] $Ca_2MgSi_2O_7$: Eu^{2+},Dy^{3+},[187] $SrAl_2O_4$: Eu^{2+}, Dy^{3+},[124] LPPs are famous for their strong green phosphorescence. The strong crystal field is required to lower the lowest emitting level of $4f^65d^1$ electron configuration and to produce yellow, orange, to red emission. Among these potential candidates, Ca_2BO_3Cl: Eu^{2+}, Dy^{3+},[25] Sr_3SiO_5: Eu^{2+}, Lu^{3+},[191, 192] $Ca_2ZnSi_2O_7$:Eu^{2+}, Dy^{3+},[193] $Sr_3Al_2O_5Cl_2$: Eu^{2+}, Tm^{3+},[26] CaS: Eu^{2+},[103] $Ca_2Si_5N_8$: Eu^{2+}, Tm^{3+},[86, 234, 235] seems to be the most promising ones. The LPP of most of Eu^{2+}-doped oxides only could be activated by ultraviolet light, while under the irradiation of ultraviolet-visible light Eu^{2+}-doped sulfides and nitrides exhibit the red LPP. Obviously, the research of Eu^{2+}-activated LPPs mainly concentrates on the Eu^{2+}-doped aluminates and silicates, and in all the LPPs, Eu^{2+}-doped LPPs also are most.

Ce^{3+} is second important afterglow activator of lanthanide series that has $4f^1$ configuration and is, therefore, capable of producing broad emission band, due to the strong crystal field dependence of its 5d–4f transition energy.[14] The Ce^{3+}-doped Lu_2SiO_5,[198] $Ca_2Al_2SiO_7$,[199] $SrAl_2O_4$,[196, 218] $CaAl_2O_4$,[196, 218] $CaAl_4O_7$,[121, 122] $Sr_4Al_{14}O_{25}$,[121, 122] $Sr_3Al_2O_5Cl_2$,[292] *etc*. all have blue-green LPP with long persistent time >3h under the excitation of UV light. The characteristics of typical Ce^{3+}-activated LPPs are as follows: (1) the host mainly concentrates on aluminate; (2) the afterglow emission band locates at blue light region. The green-yellow LPP are shown in Ce^{3+}-doped $Y_3Sc_2Ga_3O_{12}$ (blueish green),[32, 215] $Lu_3Al_2Ga_3O_{12}$ (blueish green),[157] $Y_3Al_2Ga_3O_{12}$ (green),[41, 81] $Gd_3Al_2Ga_3O_{12}$ (yellow)[216, 217] garnet transparent ceramics. Most notably, the LPP of these materials could be activated under the excitation of 460 nm blue light along with UV light.

5.1.1.2 Eu^{3+}, Sm^{3+}, Pr^{3+}, Tb^{3+} and Dy^{3+}

The researches about Eu^{3+}, Sm^{3+}, Pr^{3+}, Tb^{3+} and Dy^{3+}-activated LPPs are not so numerous comparing to that of Eu^{2+} and Ce^{3+}-doped LPPs. Eu^{3+}-doped LPPs are studied as efficient red emitting phosphors due to the abundant transitions from the excited $^5D_0$ level to the ^7F_J (J = 0, 1, 2, 3, 4) levels of $4f^6$ configuration in the orange–red light area. Main researches about Eu^{3+}-doped LPPs focus on Eu^{3+}-doped oxysulfide, such as, Gd_2O_2S: Eu^{3+} (Gd_2O_2S: Eu^{3+}, Si^{4+}, Ti^{4+},[293] Gd_2O_2S: Eu^{3+},Mg^{2+}, Ti^{4+} [272]) and Y_2O_2S: Eu^{3+} (Y_2O_2S: Eu^{3+}, M^{2+} (M = Mg, Ca, Sr, Ba), Ti^{4+}, Y_2O_2S: Eu^{3+}, Zn^{2+}, Ti^{4+},)[114, 271] phosphors. In Y_2O_2S/Gd_2O_2S host, Eu^{3+} replaces the site of Y^{3+}/Gd^{3+} as the emission center, while Mg^{2+} and Ti^{4+} also replace the site of Y^{3+}/Gd^{3+} to form traps which store energy and gradually transfer to Eu^{3+}. In addition, many Eu^{3+}-doped oxides are also reported, such as $SrMg_2(PO_4)_2$: Eu^{3+}, Zr^{4+},[294] Lu_2O_3: Eu^{3+},[173] MO: Eu^{3+} (M=Ca, Sr, Ba)[172] and $Ba_5Gd_8Zn_4O_{21}$: Eu^{3+}.[295, 296]

Among all rare earth ions, Sm^{3+} is famous for generating intense reddish orange emitting light which is ascribed to the typical transitions between the ground state and the excited state electron configuration of

Sm^{3+}. In fact, as the important red emitting center, the LPP of Sm^{3+} has been found in various material systems from oxides (CaO: Sm^{3+},[297] $La_2Zr_2O_7$: Sm^{3+},Ti^{4+},[266] $Sr_2ZnSi_2O_7$: Sm^{3+},[205]) to oxysulfide (La_2O_2S: Sm^{3+})[273], then to fluoride (KY_3F_{10}: Sm^{3+})[290]. The systematical investigations of afterglow properties of Sm^{3+} focus on Sm^{3+}-doped stannate (Ca_2SnO_4: Sm^{3+},[246] Sr_2SnO_4: Sm^{3+},[34] and $CaSnSiO_5$: Sm^{3+},[208] *etc.*). After the ultraviolet irradiation for 5 min, $Sr_3Sn_2O_7$: Sm^{3+} phosphor emited intense reddish-orange afterglow from $4G_{5/2}$ to $6H_J$ (J = 5/2, 7/2, 9/2) transitions, and its afterglow could be seen with the naked eye in the dark clearly for more than 1 h.[247] A 4.8 h persistent duration of Sm^{3+} transition from ground state $4G_{5/2}$ level to its lower multiplets was presented in $Na_2CaSn_2Ge_3O_{12}$: Sm^{3+} red LPPs after being irradiated by 254 nm UV light.[78]

Pr^{3+} ion is another ion for generating red light because it shows an emission with chromaticity coordinates (CIE 1931) x=0.68, y=0.31 due to Pr^{3+} $^1D_2 \rightarrow {}^3H_4$, $^3P_0 \rightarrow {}^3H_6$ and $^3P_0 \rightarrow {}^3F_2$ transitions. Red afterglow of Pr^{3+} ion initially was found in Pr^{3+}-doped perovskite-type oxides with a chemical formula ABO_3 ($CaTiO_3$,[260] $NaNbO_3$,[261] and $SrZrO_3$[259] *etc.*). Afterwards, other Pr^{3+} activated LPPs are also reported to emit the red LPP, such as $CdGeO_3$: Pr^{3+},[240] $ZnTa_2O_6$: Pr^{3+},[270] $Y_3Al_5O_{12}$: Pr^{3+},[220] $La_2Ti_2O_7$: Pr^{3+},[266] $Ca_2Zn_4Ti_{16}O_{38}$: Pr^{3+},[35] $CaSnSiO_5$: Pr^{3+},[208] Ca_2SnO_4: Pr^{3+},[250] YPO_4: Pr^{3+}, Ln^{3+} (Ln = Nd, Er, Ho, Dy).[27] Tb^{3+} doped LPPs always present an efficient green LPP, due to the 4f inter-transition $^5D_4$ to ^7F_j (j = 6, 5, 4, 3) of Tb^{3+}. Joanna *et al.* pointed out the green LPP resulted from a radiative relaxation of the excited Tb^{3+} ion and the only transitions from $^5D_4$ to ^7F_J states. The cross-relaxation between two adjacent Tb^{3+} ions weakens $^5D_3 \rightarrow {}^7F_j$ transitions and enhances the $^5D_4 \rightarrow {}^7F_j$ transitions, leading to a green long afterglow of the phosphors. The reported green Tb^{3+}-doped LPPs refer to Lu_2O_3: Tb^{3+},[175] $CdSiO_3$: Tb^{3+},[23] $CaSnSiO_5$: Tb^{3+},[208] Ca_2SnO_4: Tb^{3+},[248] $CaZnGe_2O_6$: Tb^{3+},[122] Y_2O_2S: Tb^{3+}, Sr^{2+}, Zr^{4+},[298] $Sr_3Al_2O_5Cl_2$: Tb^{3+},[291] *etc.*

Due to the appropriate transitions $^4F_{9/2} \rightarrow {}^6H_{15/2}$ and $^4F_{9/2} \rightarrow {}^6H_{15/2}$ of Dy^{3+}, Dy^{3+}-doped luminescent materials are usually selected as the white-light candidate. Generally speaking, white long lasting phosphors can be obtained by combination of the currently available blue, green and red phosphors. However, it is difficult to fabricate such a phosphorescent phosphor that retains the persistent white color all the time. The reason is that different phosphors seldom have very similar decay times. Dy^{3+} offers an opportunity to achieve a white-light afterglow emitting. Two main groups of emission lines of Dy^{3+} are in the wavelength ranges of 470–500 nm (blue) and 570–600 nm (yellow), corresponding to the $^4F_{9/2} \rightarrow {}^6H_{15/2}$ and $^4F_{9/2} \rightarrow {}^6H_{15/2}$ transitions, respectively. Now, $Ca_3SnSi_2O_9$: Dy^{3+},[209] $Sr_2Al_2SiO_7$: Dy^{3+},[184] $CdSiO_3$: Dy^{3+},[23] $CaAl_2O_4$: Dy^{3+},[221] $CaMgSi_2O_6$: Dy^{3+},[200, 202] $CaSnSiO_5$:Dy^{3+},[208] Sr_2SiO_4: Dy^{3+},[57, 190] Y_2O_2S: Dy^{3+}, Mg^{2+}, Si^{4+},[274] *etc.* have shown their white afterglow by singly doping Dy^{3+} ions.

5.1.1.3 Tm^{3+}, Yb^{2+} and Yb^{3+}

There are seldom reports on the LPPs employing Tm^{3+}, Yb^{2+}, and Yb^{3+} as the phosphorescent center, due to the possible difficulty of finding a suitable host for Tm^{3+}, Yb^{2+}, and Yb^{3+} to yield the phosphorescence. Su *et al.* investigated the blue LPP in Tm^{3+}-doped $Zn_2P_2O_7$ LPPs.[68, 150] Blue afterglow emission was related to the characteristic transitions of Tm^{3+} $^1D_2 \rightarrow {}^3H_6$, $^1D_2 \rightarrow {}^3H_4$ and $^1G_4 \rightarrow {}^3H_6$. After the UV light excitation source was switched off, the bright blue LPP was observed which could last for more than 1 h (0.32mcd/m^2). The green LPP was observed in $Sr_4Al_{14}O_{25}$: Yb^{2+}, Dy^{3+},[82] and $SrAl_xO_{(1+1.5x)}$: Yb^{2+} (x=3, 4, 5)[56] phosphors, while the red LPP was presented in SrS: Yb^{2+}.[276] The afterglow-emitting should be assigned to Yb^{2+} $4f^{13}5d^1 \rightarrow 4f^{14}$ transition. Recently, Valentina Caratto *et al*. developed a series of phosphorescent Yb^{3+}-doped hexagonal II-type Gd oxycarbonate phosphors, $Gd_{2-x}Yb_xO_2CO_3$ with the persistent duration of 144h.[299] Such phosphors demonstrated a high afterglow intensity in NIR region, that was independent on the temperature and made this materials particular attractive as optical bio-labels for bio-imaging.

5.1.1.4 Briefly Discussions

Table 15. Standard reduction potentials E_{red} of rare earths

Electro-pair	*E*(V)	Electro-pair	*E*(V)
Ce^{4+}/Ce^{3+}	+1.74	Eu^{3+}/Eu^{2+}	-0.35
Tb^{4+}/Tb^{3+}	+3.1±0.2	Yb^{3+}/Yb^{2+}	-1.15
Pr^{4+}/Pr^{3+}	+3.2±0.2	Sm^{3+}/Sm^{2+}	-1.55

Nd^{4+}/Nd^{3+}	+5.0±0.4	Tm^{3+}/Tm^{2+}	-2.3±0.2
Dy^{4+}/Dy^{3+}	+5.2±0.4		

Besides the above summary, it is necessary to find the similarity of emission centers that have the ability of activating afterglow. As we know, rare earth ions, have atomic numbers that range from 57 to 71. Lanthanide elements adopt either the $[Xe]4f^n6s^2$ or $[Xe]4f^{n-1}5d^16s^2$ configuration depending on the relative energy level of these two electronic configurations. They tend to lose three electrons and exhibit a +3 valence state. According to Hund's rule, electron shells are stable when empty, full or half-full. For example, the configurations $4f^0$ (La^{3+}), $4f^7$ (Gd^{3+}), and $4f^{14}$ (Lu^{3+}) are stable. Ce^{3+}, Pr^{3+}, and Tb^{3+} have one or two more electrons than required for stable electronic configurations so they can be further oxidized to a +4 state. In contrast, Sm^{3+}, Eu^{3+}, and Yb^{3+} have one or two fewer electrons than required for a stable electronic configuration and they, therefore, tend to receive one or two electrons and undergo a reduction to a +2 state. Standard reduction potentials, $E_R^{4+}{}_{/R}{}^{3+}$ and $E_R^{3+}{}_{/R}{}^{2+}$, represent the driving force stability of the reduction state. The more positive the value of E_{red}, the greater the driving force for reduction. The standard reduction potentials of rare earths are shown in Table 15.

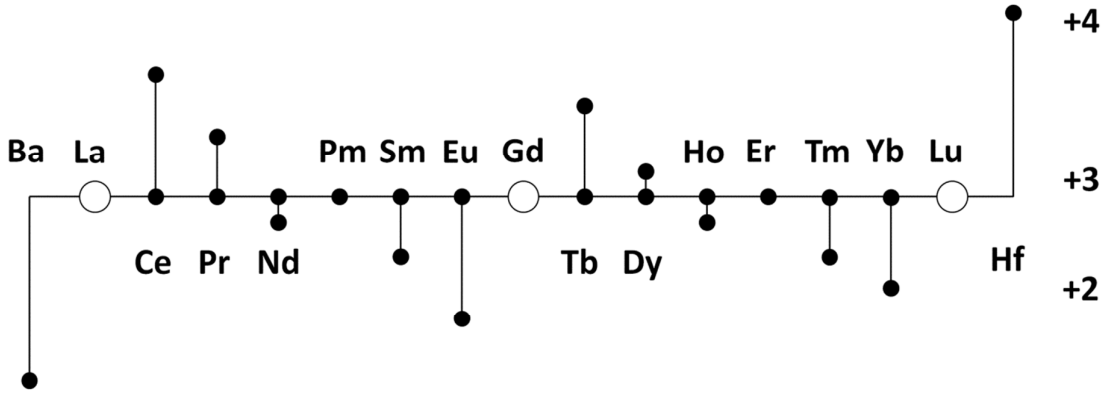

Fig. 16 Valence states of lanthanide elements.

Fig 16 visualizes the trend. The transverse axis is the atomic number and the length of the short lines along the vertical axis represents the trend of valence state variation. Coincidentally, the well-known Ce, Eu, Pr, Sm, Tb, Dy, Yb and Tm all have the strong tendency of valence state variation. Up to now, there are few reports about LLPs with Er, Nd, Pm, Ho, La, Lu and Gd as the isolated phosphorescent center.

5.1.2 Transition Metal Ions

5.1.2.1 Mn^{2+} and Mn^{4+}

Mn^{2+} has a $^3d_5$ electron configuration with a broad emission band varying from blue-green (490 nm) to far red (750 nm). The emission from Mn^{2+} transition is ascribed to the parity-forbidden 3d-3d intra-atomic transition from the lowest excited level $^4T_1$ (4G) to the ground state $^6A_1$ (6S). Tetrahedral coordinated Mn^{2+} ion gives a green emission, while octahedral coordinated Mn^{2+} ion exhibits an orange-to-red emission.[1, 285] Therefore, the emission color strongly depends on the coordination number (CN) of Mn^{2+} in hosts. A distinct sample was presented in the afterglow spectra of β-$Zn_3(PO_4)_2$: Mn^{2+}/Ga^{3+} and γ-$Zn_3(PO_4)_2$: Mn^{2+}/Ga^{3+}.[238] β-$Zn_3(PO_4)_2$: Mn^{2+}/Ga^{3+} phosphor was a good red long lasting phosphor, while γ-$Zn_3(PO_4)_2$: Mn^{2+}/Ga^{3+} phosphor presented green and red long lasting phosphorescence. The reason was that two kind of coordination number (CN=4 and 6) was observed in γ-$Zn_3(PO_4)_2$: Mn^{2+}/Ga^{3+} while only one coordination number (CN=6) was presented in β-$Zn_3(PO_4)_2$: Mn^{2+}/Ga^{3+} phosphor. In addition, Zn_2GeO_4: Mn^{2+} showed a green afterglow,[241] while $CdSiO_3$: Mn^{2+},[206] Li_2ZnGeO_4: Mn^{2+},[63] $CaZnGe_2O_6$: Mn^{2+},[244] $Ca_3(PO_4)_2$: Mn^{2+},[52] $Ca_{0.2}Zn_{0.9}Mg_{0.9}Si_2O_6$: Eu^{2+}, Dy^{3+}, Mn^{2+},[85] $CaMgSi_2O_6$: Mn^{2+},[196, 197] $MgGeO_3$:Mn^{2+},[243] *etc.* presented the orange-red LPP. Apart from Mn^{2+}-doped oxides, Mn^{2+}-activated phosphorescence is also observed in Mn^{2+}-doped glasses and glass ceramics as well as nitrides (AlN: Mn^{2+})[284].

Mn^{4+} is another highly desirable NIR doping candidate, because its $^3d_3$ electron configuration allows a stabilized NIR emission from 600 to 800 nm in different hosts, which also strongly depends on the crystal-field environment of the host lattices. Our group fabricated a series of novel Mn^{4+}-doped $MAlO_3$ (M =La, Gd) LPPs

with the emission maximum around 730 nm and long persistent duration >20h (Fig. 17d)[151].

5.1.2.2 Cr^{3+}

Cr^{3+} ion is an ideal NIR emitter in solid since its $^3d_3$ electron configuration allows a narrow-band emission (700 nm) due to the spin-forbidden $^2E \rightarrow {}^4A_2$ transition, and a broadband emission (650-1000 nm) ascribed to the spin allowed $^4T_2 \rightarrow {}^4A_2$ transition (Fig. 17a). In 2011, Bessiere *et al.* first reported the LPP peaking at 695 nm in $ZnGa_2O_4$: Cr^{3+} crystals.[168-171] In 2012, Pan *et al.* broke new ground in the field by using $Zn_3Ga_2Ge_2O_{10}$ as the host, thereby achieving a super-long NIR afterglow emission time of 360h. [168-171] Our group and Allix research group independently carried out the work of improving the afterglow properties by partially substituting Zn and Sn for Ga to form Zn-Ga-Sn-O solid solution. We demonstrated that $Zn_3Ga_2SnO_8$: 0.5 Cr^{3+} powder with bright and long persistent phosphorescence over 300 h in the NIR region permitted an enabling long-term, reproducible, real-time and reliable structural imaging of deep tissues.[62]

Interestingly, all of the known Cr^{3+}-activated LPPs are gallate compounds. In addition to $La_3Ga_5GeO_{14}$: Cr^{3+},[31, 77, 79, 223] and $LiGa_5O_8$: Cr^{3+},[59] phosphors, the afterglow properties of many other Cr^{3+}-activated gallate phosphors, such as $MgGa_2O_4$: Cr^{3+},[53, 95] $Ca_3Ga_2Ge_3O_{12}$: Cr^{3+} [18, 229] and $SrGa_{12}O_{19}$: Cr^{3+},[22] were also investigated because of the excellent ability of Cr^{3+} ions to substitute for Ga^{3+} ions in distorted octahedral coordination. The predominance of Cr^{3+}-activated gallates might suggest that only gallates can be used as the hosts in Cr^{3+}-doped NIR LPPs. But recently, our group presented a series of efficient NIR Cr^{3+}-doped non-gallate LPPs (Zn_2SnO_4: Cr and $Zn_{(2-x)}Al_{2x}Sn_{(1-x)}O_4$: Cr) and highlighted their special optical characteristics of broad emission band (650–1200 nm, peaking at 800 nm) and long afterglow time >35 h (Fig. 17c).[13]

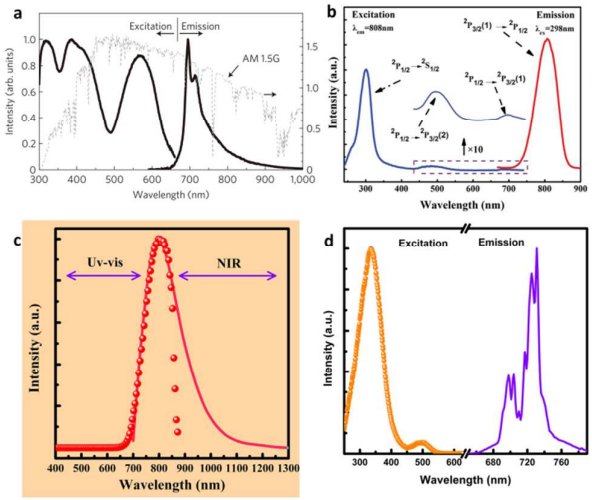

Fig. 17 (a) Normalized excitation and emission spectra of the $Zn_3Ga_2Ge_2O_{10}$: 0.5%Cr^{3+} phosphor at room temperature. (reproduced with permission from ref. 12, copyright 2012, Nature Publication Group). (b) Photoluminescence excitation and emission spectra of the $SrSnO_3$:5% Bi^{2+} phosphor at room temperature. (c) Normalized VIS-NIR long-persistence phosphorescence spectra of Zn_2SnO_4: 0.2%Cr^{3+}. (d) Photoluminescence excitation and emission spectra of the $LaAl_{0.999}O_{2.9985}$: 0.1% Mn^{4+} phosphor.

5.1.3 Main Group Elements

Several kinds of Bi^{3+}-activated crystals have been reported for their potential applications in white light emitting diodes. Though luminescent emission bands cover various wavelength regions from blue to red also depending on the coordination states of the active centers, the reported Bi^{3+}-activated LPPs including $CaWO_4$: Bi^{3+},[267, 268] $ZnGa_2O_4$: Bi^{3+},[231] Zn_2GeO_4: Bi^{3+},[245] $CdSiO_3$: Bi^{3+},[122, 207] all offered a ultraviolet-blue afterglow emission. In addition to Bi^{3+}, the luminescent behaviors of Bi^{2+} are also easily influenced by the nearby chemical environment, thus generating the visible-NIR luminescent emission. Recently, our group synthesized a new long phosphorescent phosphor $SrSnO_3$:Bi^{2+}. The phosphor showed deep red-NIR persistent luminescence with a broad emission band from 700 to 900 nm peaking at 808 nm, as well as a persistence time of >30 min (Fig. 17b).[257]

5.2 Hosts

For the activation of long persistent phosphorescence, the host serves as the trap carrier. Different hosts have the various store abilities of electrons due to the different content of traps. There are two avenues to

achieving this goal of introducing traps into the host: adding intrinsic thermal defects or extrinsic defects.

Table 16 lists the volatilization temperature and boiling point of metals and corresponding oxides. The intrinsic defects refer to the thermal defects include cation vacancies, anion vacancies and interstitial ions, which are easily generated during the high treatment. Therefore, volatilization is considerable factor. It is clear that traps can be formed in the oxides with lower melting point and high volatility, such as, ZnO, WO_3, CaO, SrO, P_2O_5, GeO_2 *etc.* In fact, another situation also needs to be considered. Traps are also produced in SnO_2, Al_2O_3, Ga_2O_3, *etc.* because the corresponding metal ion has the lower volatilization temperature comparing to the oxides, prompting the possible faster volatilization of metal ion in the oxides. The reported LPPs also mainly focused on these hosts (silicate, aluminate, phosphate, germinate, gallate, stannate, *etc*.).

Table 16. Volatilization temperature and boiling point of metals and corresponding oxides

Oxide				Metal			
Materials	Temperature (°C)	Boiling point (°C)	Volatility	Materials	Temperature (°C)	Boiling point (°C)	Volatility
CaO	1297	2580	Middle	Ca	459	1484	Middle
SrO	1517	>3000	Middle	Sr	394	1384	Middle
Lu_2O_3		2510	Low	Lu		3395	Low
SnO_2		1800	High	Sn	997	2602	Middle
ZrO_2	2077	4300	Low	Zr		4377	Low
Ga_2O_3		1900	Middle	Ga	907	2072	Middle
SiO_2		2230		Si	1337	2287	
Al_2O_3	1905	2980	Middle	Al	972	2056	Middle
P_2O_5		360	High	P	129	280	High
GeO_2		1200	High	Ge	1137	2833	Middle
TiO_2	1780	2972	Middle	Ti	1442	3287	Middle
WO_3	1079	1837	High	W	2757	5555	Low
ZnO	871	1949	High	Zn	247	906	High

In addition to synthesis condition, the generation of these defects is also closely correlated with the crystal structure and coordination geometry of activators in hosts. $ZnGa_2O_4$ (ZGO) was an AB_2O_4 compound with spinel structure and Zn^{2+} and Ga^{3+} ions occupying tetrahedral A and octahedral B sites, respectively (Fig. 18a). Although it was most widely considered as a normal spinel, it exhibited a slight inversion character, wherein a few percent of Zn^{2+} and Ga^{3+} occupied B and A sites, respectively. Such defects in the host matrix were called antisite defects and were just a Zn ion at a Ga site and a Ga ion at a Zn site in an ideal normal spinel structure type. ZGO exhibited about 3% inversion, which meant that ~3% of Zn^{2+} occupied Ga sites, and correlatively the same amount of Ga^{3+} occupied Zn sites. They further pointed out that A Ga ion in a Zn site is a positively charged defect ($Ga_{Zn}^{\cdot}$) and Zn in a Ga site is a negatively charged defect (Zn_{Ga}') in Kröger-Vink notation. Trapping of a defect pair (electron-hole) could be related to a permutation of Ga and Zn (antisite defects) close to Cr^{3+} ions (Fig. 18b).[20, 49]

Our group synthesized a series of Zn_2SnO_4: Cr phosphors. Zn_2SnO_4 was employed as a host to take advantage of its characteristic inverse spinel crystal structure, easy substitution into Zn^{2+} and Sn^{4+} sites by Cr^{3+} in distorted octahedral coordination and non-equivalent substitution (Fig. 18c). Compared with normal spinel, the inverse spinel structure featured an alternative cation arrangement. In Zn_2SnO_4, all of the Sn octahedron (Sn^{VI}) cations and half of Zn octahedron (Zn^{VI}) cations occupied octahedral sites, whereas the other half of Zn tetrahedron (Zn^{IV}) cations occupied tetrahedral sites. Based on this arrangement, in addition to the intrinsic Zn vacancies and Zn interstitials, some antisite defects (such as [Sn^{VI}] and [Zn^{VI}] cations, which can freely exchange places in octahedral sites) and non-equivalent substitutional defects (Sn_{Cr} or Zn_{Cr}) were expected to be formed.[13]

The third factor influencing the capacity of traps in hosts is the doping ions, used to provide the extrinsic defects. Modern investigations to LPPs revealed a fact that doping ions (here, the doping ions refer to

co-dopants) could influence the trap distribution, such as, increasing traps' concentration, deepening the depth of traps. One of the most remarkable examples is $SrAl_2O_4$: Eu and $SrAl_2O_4$: Eu, Dy phosphors. The weak afterglow intensity and short persistent time is exhibited in Eu-singly doped $SrAl_2O_4$ phosphor, while co-doping with Dy improves the afterglow properties. The generation of intentionally introduced defects, which come from co-dopant are not in correlation with the treatment temperature, but closely associated with the properties of dopant, i.e. atomic radius, valence state, doing content *etc.* In this mechanism, charge compensation is a key part which needs to be considered for producing traps.

In fact, the intrinsic thermal defects and extrinsic defects often work together to improve the trap distribution in most LPPs. Hosal *et al.* studied the optical properties of ZrO_2: Ti^{3+} and ZrO_2: Ti^{3+}, Lu^{3+} LPPs.[157] In these phosphors, Ti^{3+} was the luminescence center, while the introduction of Lu^{3+} obviously extended the afterglow time. Lu^{3+} ion replaced Zr^{4+} in ZrO_2: Ti^{3+}, Lu^{3+} and an oxygen vacancy (V_O) was created as a result of charge compensation. These defects influenced directly the trap distribution of ZrO_2 host, acting as traps for electrons (V_O) or holes (M_{Zr}) in the lattice. The intrinsic and extrinsic lattice defects are also found in $Sr_2MgSi_2O_7$: Eu^{2+}, R^{3+} material.[300] In this phosphor, the intrinsic defects included cation vacancies, V_M (with double negative net charge), and oxygen vacancies, V_O (double positive), as well as interstitial ions. Cation vacancies also appeared and existed due to the charge compensation when the introduced R^{3+} replaces M^{2+} (R_M). The similar trap distribution were also observed in non-doped and trivalent rare earths-doped $CdSiO_3$ LPPs, including the intrinsic defects in non-doped host (e.g. cadmium and oxide vacancies created by the evaporation of CdO) and the charge compensation defects related to the presence of R^{3+} in the Cd^{2+} sites (creating interstitial oxide ions or Cd^{2+} vacancies)[23].

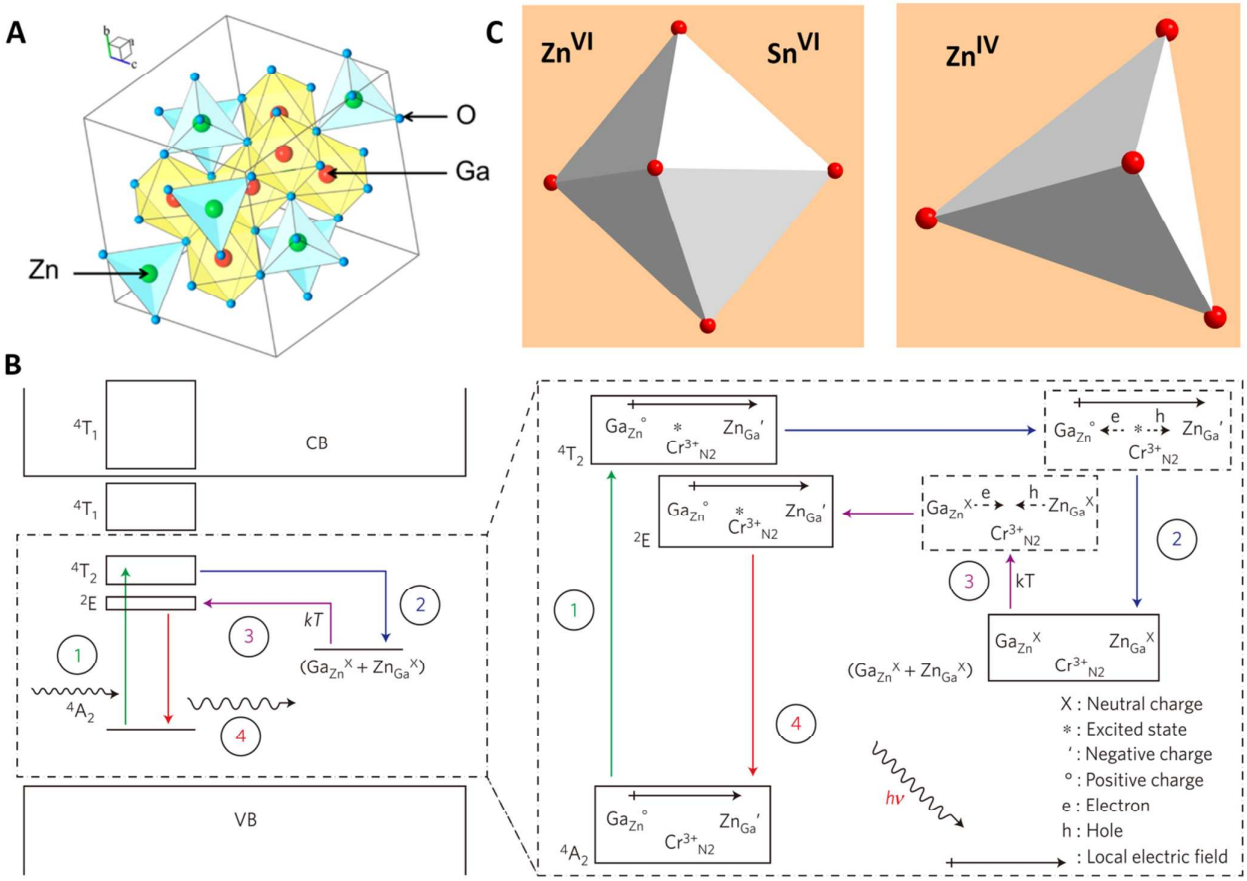

Fig. 18 (A) Cubic spinel structure of ZGO (reproduced with permission from ref. 49, copyright 2014, American Chemical Society).(B) Mechanism scheme proposed for the persistent luminescence induced by LED excitation (reproduced with permission from ref. 11, copyright 2014, Nature Publication Group). (C) Octahedral and tetrahedral geometry of Zn_2SnO_4.

5.3 Emission bands

5.3.1 Visible long persistent phosphorescence

Table 17. Afterglow color and corresponding activators

Afterglow Color	Activators	Afterglow Color	Activators
Green afterglow	Eu^{2+}, Tb^{3+}, Ce^{3+}, Mn^{2+}	Blue afterglow	Eu^{2+}, Ce^{3+}, Tm^{3+}, defects
Red afterglow	Eu^{3+}, Eu^{2+}, Yb^{2+}, Sm^{3+}, Pr^{3+}, Mn^{2+},	White afterglow	Dy^{3+}
NIR afterglow	Nd^{3+}, Bi^{2+}, Yb^{3+}, Mn^{2+}, Mn^{4+}, Cr^{3+}		

ZnS: Cu, Co was the pioneer of green long phosphorescent phosphor. In 1996, Matsuzawa *et al.* reported a $SrAl_2O_4$: Eu^{2+}, Dy^{3+} phosphor with bright green persistent phosphorescence.[124] After this report, many remarkable green LPPs having a long afterglow time >10 h doped with Eu^{2+} as a phosphorescent center were further studied, including the silicates ($Ca_2MgSi_2O_7$: Eu^{2+}, Dy^{3+},[187] $Ba_4(Si_3O_8)_2$: Eu^{2+}, Dy^{3+},[183]) and aluminates ($Sr_4Al_{14}O_{25}$: Eu^{2+}, Dy^{3+},[210])-based LPPs *etc*. In addition to Eu^{2+}, Tb^{3+}, Ce^{3+}, and Mn^{2+} ions were also selected as the common green phosphorescent activators. Blue LPP is also important for the practical applications of emergency display *etc.* The presently available commercial blue phosphor is $CaAl_2O_4$: Eu^{2+}, Nd^{3+}.[124] In fact, Ce^{3+}, Tm^{3+} and defects-activated LPPs as well as other Eu^{2+}-doped LPPs with long persistent duration > 6h were also suitable as the blue materials, such as, $Sr_2P_2O_7$: Eu^{2+}, Y^{3+},[232] $Sr_3MgSi_2O_8$: Eu^{2+}, Dy^{3+},[133] as well as $CaAl_4O_7$: Ce^{3+},[121, 213] and defect site-doped LPPs ($Ca_2ZrSi_4O_{12}$,[144] Li_2ZnGeO_4,[63] $BaZrO_3$: Mg [269]).

At present, LPPs exhibiting high brightness of blue and green phosphorescence are commercially available. However, red LPPs are in great scarcity and none of them is good enough to be applied to practical applications, since the sensitivity of human eye is lower for red light than that for blue or green light. In recent years, many researchers focused on improving the afterglow properties of red LPPs, by employing Eu^{3+}, Eu^{2+}, Yb^{2+}, Sm^{3+}, Pr^{3+}, Mn^{2+}, as the activating ions. At this stage, most of the LPPs are based on Eu^{2+} doped sulfides and nitrides (Ca_2SiS_4: Eu^{2+}, Nd^{3+},[121] $SrCaSi_5N_8$: Eu^{2+}, Tm^{3+},[87, 235, 236]) as well as Eu^{3+}-activated oxysulfides (Gd_2O_2S: Eu^{3+},[223] Y_2O_2S: Eu^{3+}, [272]), Sm^{3+}-activated oxysulfides and stannates (La_2O_2S: Sm^{3+},[273] Sr_2SnO_4: Sm^{3+},[34]), Pr^{3+}-activated stannates and perovskite-type compounds ($CaTiO_3$: Pr^{3+},[260] Ca_2SnO_4: Pr^{3+},[250] $NaNbO_3$: Pr^{3+},[261] $CdGeO_3$: Pr^{3+},[240]), Mn^{2+}-activated LPPs ($MgGeO_3$: Mn^{2+},[243] $Zn_3(PO_4)_2$: Mn^{2+}/Ga^{3+},[238] AlN: Mn^{2+},[284] $Ca_{0.2}Zn_{0.9}Mg_{0.9}Si_2O_6$: Eu^{2+}, Dy^{3+}, Mn^{2+},[85]) and Yb^{2+}-activated sulfides s (SrS: Yb^{2+} [276]).

White-color (full-color) LPPs as persistent emitting light sources would be important in many dark-environment applications. One of possible strategies is by combining three individual blue, green, and red LPPs activated by different centers. For example, Y_2O_2S: Tb^{3+}, Eu^{3+}, Sr^{2+}, Zr^{4+} phosphor offered a scheme of blue-green and orange light activated by Tb^{3+} and Eu^{3+} ions gaining the white afterglow, respectively.[301] Or, the energy transfer is considered as another effective route to realize the white-afterglow emitting. Energy transfer from Eu^{2+} to Mn^{2+} provided the blue-green and orange afterglow from Eu^{2+} and Mn^{2+} transition, respectively, making $CaAl_2Si_2O_8$: Eu^{2+}, Mn^{2+}, Dy^{3+} phosphor suitable for synthesizing a white phosphor.[196, 197] Another idea of integrating several afterglow emissions with similar decay rate in one single material seems more attractive. Dy^{3+} ion features its characteristic white photoluminescence, thus offering the possibility of white-afterglow emitting.

5.3.2 NIR long persistent phosphorescence

In the past few years, NIR afterglow activated by transition metals or rare earth ions received much attention. The research was triggered by a recently proposed *in vivo* imaging application and it might show more significance in the future. Optical imaging is a promising method to visualize biological tissues because it is radioactive material-free technique. NIR long persistent phosphor is used because of the high transmittance of these signals through biological tissues. Over the past few years, substantial strides have been made in the research and development of LPPs for NIR wavelengths, with the focus of the research being Nd^{3+}, Bi^{2+}, Yb^{3+}, Mn^{2+}, Mn^{4+} and Cr^{3+}-activated NIR LPPs (Fig. 19).

In 2007, Chermont *et al.* proposed a novel bio-imaging method using red-to-NIR persistent nanoparticles, $Ca_{0.2}Zn_{0.9}M_{g0.9}Si_2O_6$: Eu^{2+}, Dy^{3+}, Mn^{2+}, and opened a new application area for NIR LPPs.[85] In 2011, Bessiere reported the NIR persistent phosphorescence at 695 nm in Cr^{3+}-doped $ZnGa_2O_4$ crystals.[168-171] In 2012, Pan and Allix greatly improved the NIR persistent phosphorescence by partially substituting Zn^{2+} and Ge^{4+} for Ga^{3+} by to form $Zn_{1+x}Ga_{2-2x}Ge_xO_4$ solid solution.[12, 80] This breakthrough firmly established gallates as the preferred material system for the fabrication of Cr^{3+}-activated NIR LPPs and stimulated the research interests on developing new Cr^{3+}-doped NIR LPPs. Meanwhile, other NIR LPPs with different activators were also proposed.

Our group fabricated a series of Ge^{4+}/Mn^{4+}-co-doped $MAlO_3$ (M=La, Gd) LPPs and Bi^{2+}-doped $SrSnO_3$ LPPs, proposing two new afterglow activators, Mn^{4+} and Bi^{2+}.[151] In addition, rare earth doped LPPs are also right choice for NIR LPPs. Xu *et al.* recently found a Sr_2SnO_4: Nd^{3+} material, which exhibited NIR LPP ranging from 850 to 1400 nm,[253] while Valentina *et al.* synthesized Yb^{3+}-doped Gd-oxycarbonate LPPs with a NIR afterglow-emitting and long persistent duration >144h.[299]

As mentioned above, emission waveband is a critical issue, to promote the development of bio-labels. Varying the activators has been proven be an efficient strategy to realize the goal of long-wavelength emitting. Recently, our group proposed a new strategy, i.e. modulating the crystal field to tuning the emission band. We developed a kind of Cr^{3+}-doped non gallates, Zn_2SnO_4: Cr^{3+}.[13] The Zn and Sn octahedrons surrounding Cr^{3+} center presented weaker crystal field strength. As we know, the electronic configuration of Cr^{3+} was affected strongly by the arrangement of surrounding ligands. The dominant emission peak of a Cr^{3+} center produced a shift arising from the altered crystal field strength by adding Al and forming $Zn_{(2-x)}Al_{2x}Sn_{(1-x)}O_4$: Cr^{3+} solid solution. Al^{3+} ions were incorporated into the crystal phase by replacing octahedral Zn^{2+} and Sn^{4+} in the disordered ZnO_6 and SnO_6 octahedron. By shortening the Cr^{3+}-O^{2-} distances, achieved by the incorporation of Al^{3+} (53 pm) with its smaller ionic radii compared with Zn^{2+} (74 pm) and Sn^{4+} (69 pm), the crystal field strength of Cr^{3+} increased.

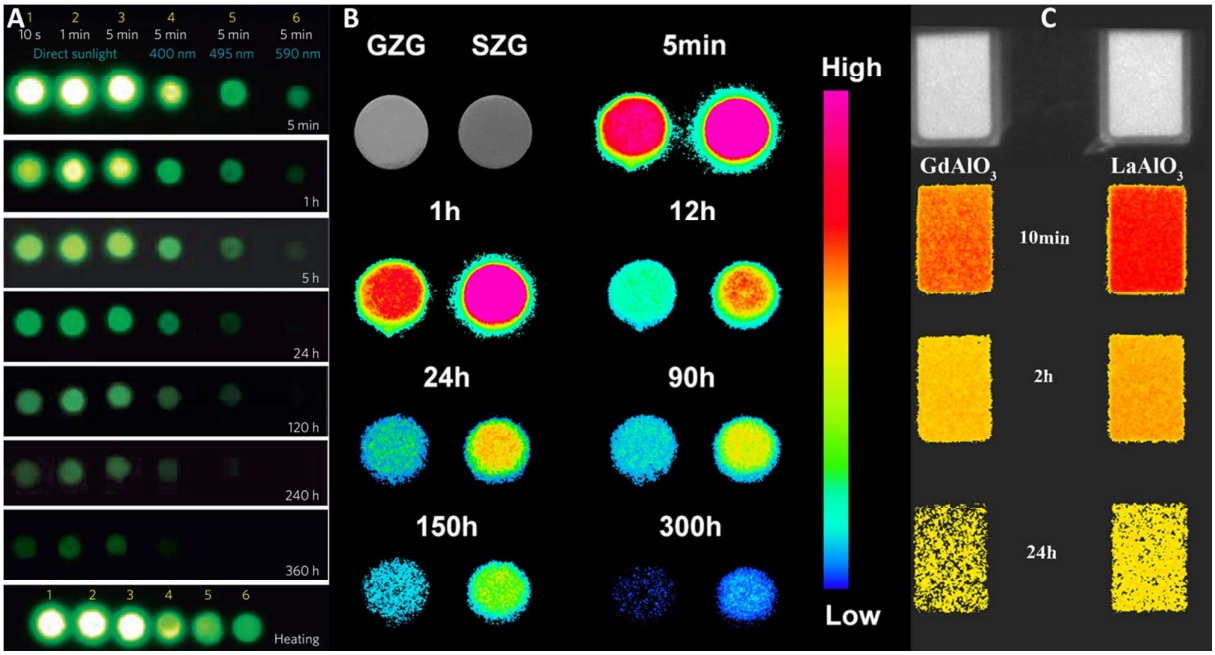

Fig. 19 (A) NIR images of $Zn_3Ga_2Ge_2O_{10}$: 0.5Cr discs taken at different afterglow times (5 min to 360 h) after irradiation by direct sunlight for 10 s, 1 min and 5 min without cutoff filters and for 5 min (reproduced with permission from ref. 12, copyright 2012, Nature Publication Group). (B) NIR images of $Zn_3Ga_2GeO_8$: 0.5Cr ,GZG (left) and $Zn_3Ga_2SnO_8$ SZG (right) powders after being pressed acquired at different time intervals (from 5 min to 300 h) after the irradiation using a xenon lamp for 30 min. (C) Long persistent luminescence imaging of samples $LaAlO_3$: Mn^{4+}, Ge^{4+} (right) and $GdAlO_3$: Mn^{4+}, Ge^{4+} (left).

In addition, the NIR LPP also could be obtained by transferring the persistent energy from one activator to another. Most reported persistent energy transfer was demonstrated in the energy transfer between rare earth ions. (a) Eu^{2+}→Nd^{3+}; Strong afterglow of $SrAl_2O_4$: Eu^{2+}, Dy^{3+}, Nd^{3+} and $CaAl_2O_4$: Eu^{2+}, Nd^{3+} LPPs at 882 nm attributed to Nd^{3+} 4f-4f transition was observed as a consequence of irradiation by ultraviolet light at 365 nm due to the persistent energy transfer from excited Eu^{2+} ions to Nd^{3+} ions.[212] (b) Ce^{3+}→Dy^{3+}; Energy transfer from Ce^{3+} to Dy^{3+} strongly supported the white light emitting in $Sr_2Al_2SiO_7$: Ce^{3+}, Dy^{3+} phosphor.[184] (c) Eu^{2+}→Er^{3+}; A near infrared LPP at 1530 nm was activated via the persistent energy transfer process from Eu^{2+} ions to Er^{3+} ions in $SrAl_2O_4$: Eu^{2+}, Dy^{3+}, Er^{3+} phosphor.[113] (d) Other energy transfer between rare earths, such as Eu^{2+}→Sm^{3+},[184] Ce^{3+}→Tb^{3+},[219] Ce^{3+}→Dy^{3+},[184] Ce^{3+}→Dy^{3+},[81] also was investigated in the hosts of silicates and aluminates.

In addition to rare earth ions, transition metal ions, involving Cr^{3+} ($Y_3Al_{5-x}Ga_xO_{12}$ [x=2.5, 3, 3.5]: Ce^{3+}, Cr^{3+}, $Sr_4Al_{14}O_{25}$: Eu^{2+}, Dy^{3+}, Cr^{3+}, $SrAl_2O_4$: Eu^{2+}, Dy^{3+}, Cr^{3+},)[41, 81] and Mn^{2+} ($Ca_{0.2}Zn_{0.9}Mg_{0.9}Si_2O_6$: Eu^{2+}, Dy^{3+}, Mn^{2+},[85] and

$CaAl_2O_4$: Ce^{3+}, Mn^{2+},[196, 218]) were also commonly selected as activators and emitted the intrinsic phosphorescence via the PET $R^{3+}\rightarrow Cr^{3+}/Mn^{2+}$. Meanwhile, the self-activated afterglow was also observed in some un-doped LPPs, such as, $CdSiO_3$,[23] $CaSnSiO_5$,[208] $Ca_3SnSi_2O_9$,[209] *etc.*, with the corresponding PET from defects to activators (Tb^{3+}, Sm^{3+}, Dy^{3+} *etc.*).

5.4 Excitation Bands and Excitation Modes

For the same activator, the photoluminescent excitation spectra may be different from the excitation spectra of LPP. The reason maybe involves the energy-level configuration of activators and band gap of hosts, The afterglow of the LPPs with relatively broad band gap is easily excited by high energy rays (x-ray or cathode-ray), such as fluorides, while high energy rays and ultraviolet light have been widely used as the excitation source to activate the afterglow of oxides-based LPPs. By analogy, the visible light could effectively activate the afterglow of sulfides (CaS: Eu^{2+}) or nitrides ($Ca_2Si_5N_8$: Eu^{2+})-based LPPs with narrow band gap, but less effectively activate the afterglow of oxides-based LPPs.[302]

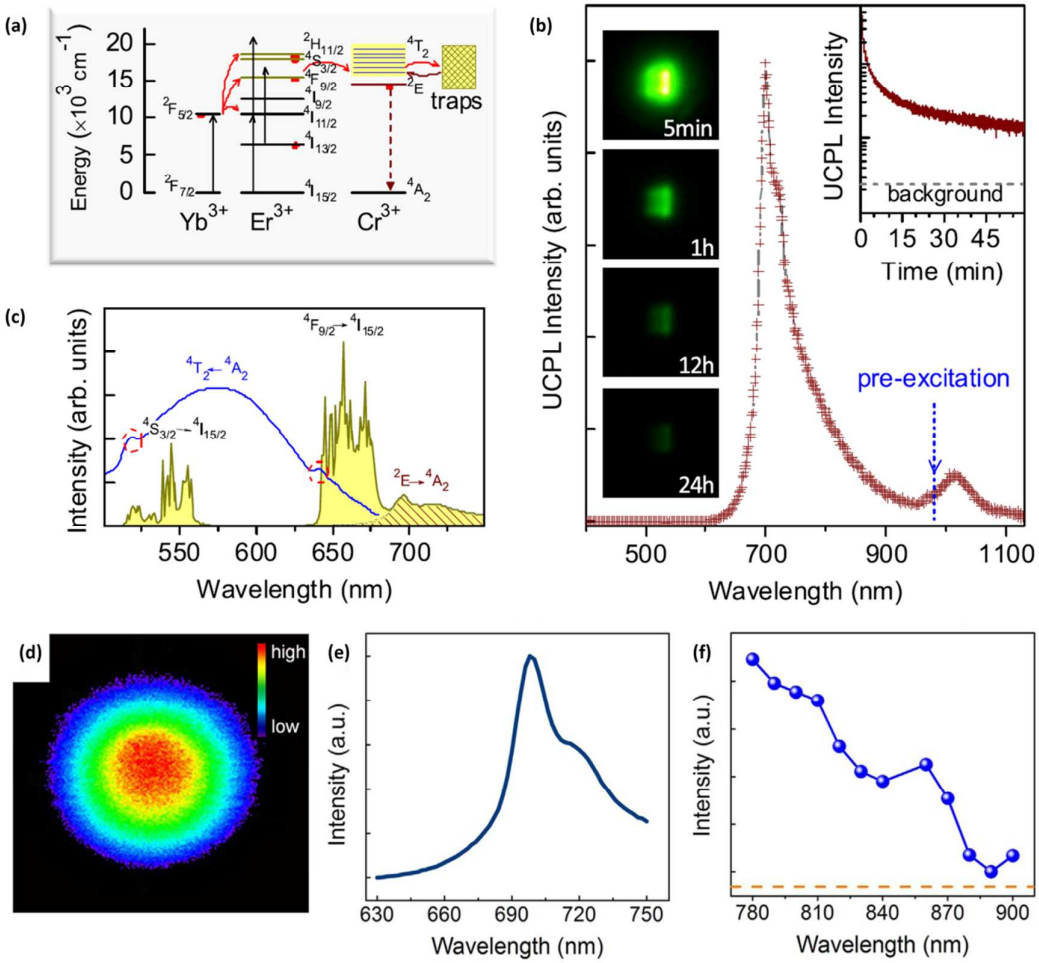

Fig. 20 (a) UCPL schematic diagram in the $Zn_3Ga_2GeO_8$: 1%Cr^{3+}, 5%Yb^{3+}, 0.5%Er^{3+} system. (b) Up-converted luminescence emission spectrum (curve with yellow shadow) under a 980 nm laser excitation and photoluminescence excitation spectrum of Cr^{3+} (blue solid-line curve) by monitoring the 700 nm emission. (c) UCPL emission spectrum of $Zn_3Ga_2GeO_8$: 1%Cr^{3+}, 5%Yb^{3+}, 0.5%Er^{3+} recorded at 5 s after the stoppage of a 980 nm laser excitation (reproduced with permission from ref. 28, copyright 2014, American Physical Society). (d) Luminescence image of $Zn_3Ga_2Ge_2O_{10}$: Cr^{3+} taken at the interval of 24 hours after charging of the sample for illumination with an incoherent LED operating at a wavelength of 800 nm. (e) Photo-stimulated luminescence spectrum under excitation at 800 nm and (f) the corresponding photo-stimulated luminescence excitation spectra monitored at 700 nm of $Zn_3Ga_2Ge_2O_{10}$: Cr^{3+}.

Experimental data confirmed that KY_3F_{10}: Tb^{3+},[290] Lu_2O_3: Pr,[169, 174] $Sr_4Al_{14}O_{25}$: Ce^{3+},[121, 122] YPO_4: Pr^{3+},[27] $MgGa_2O_4$:Cr^{3+},[53, 95] *etc.* could be excited by x-ray or beta rays. In fact, most of oxides-based LPPs could be more effectively activated by UV light (250-400nm). Only few oxides-based LPPs could be activated by visible light, mainly referring to Ce^{3+}-doped (or Ce^{3+}-Cr^{3+}, Ce^{3+}-Pr^{3+} co-doped) and Cr^{3+}-doped oxides. Su *et al*. reported the LPP of $Y_3Al_5O_{12}$: Ce^{3+} under the excitation of UV light at 254 nm.[214] But they did not find that the phosphorescence also can be excited by visible light. Tanabe *et al*. developed bright LPPs of Ce^{3+}-doped

$Y_3Al_{5-x}Ga_xO_{12}$ (x=2.5, 3, 3.5) ceramics with green luminescence (Ce^{3+}: 5d→4f) via blue-light excitation.[216, 217] The persistent luminance value 5 min after ceasing blue-light excitation was approximately many times better than that from compact $SrAl_2O_4$: Eu^{2+}-Dy^{3+} powders. Afterwards, sunlight-activated Cr^{3+}-doped zinc gallogermanate LPPs were reported, and the NIR persistent phosphorescence can be effectively achieved under ultraviolet illumination (300-400 nm), but less effectively achieved under visible light (400-630 nm). It is notable that in the afterglow excitation spectra of Eu^{2+}-doped LPPs, few Eu^{2+}-doped oxides exhibit the visible excitation band, while Eu^{2+}-doped sulfides and nitrides are easily observed the existing visible excitation band.[12]

Recently, Liu *et al.* proposed the concept of up-converted persistent luminescence (UCPL) by energy transfer (Fig. 20a-c).[28] Guided by the UCPL concept, they fabricated the $Zn_3Ga_2GeO_8$: 1%Cr^{3+}, 5%Yb^{3+}, 0.5%Er^{3+} material by incorporating an up-converting ion pair Yb^{3+}-Er^{3+} into a $Zn_3Ga_2GeO_8$: 1%Cr^{3+} near-infrared persistent phosphor. After being excited by a 980 nm laser, the phosphor emitted long-lasting (>24 h) near-infrared persistent emission peaking at 700 nm. In fact, the proposed strategy in this work involved not only a new long-wavelength excitation band (NIR region), but also a new excitation mode (incoherent excitation and coherent excitation). Coherent excitation has the advantage of large power density comparing to Xe lamp, thus offering the potential of improving the excitation efficiency of afterglow. Earlier, our group first proposed a coherent excitation mode. Our research results demonstrated that NIR photo-stimulated luminescence and phosphorescence could be repeatedly obtained under the excitation of NIR incoherent (780 to 900 nm light of Xe lamp) and coherent light (980 and 808 nm laser) in $Zn_3Ga_2Ge_2O_{10}$: Cr^{3+} and $Zn_3Ga_2GeO_8$: Cr^{3+} phosphors (Fig. 20d-f).[15]

6. Applications

6.1 Displays and safety signs

The earliest application of LPPs was luminous Pearl, a peculiar phosphorescent material emitting green phosphorescence at night. Untill now, many green LPPs have been used as the night displays and safety sign. A prototype of ZnS-type phosphors, an important class of phosphors for television tubes, was first prepared in 1866 by Theodore Sidot, a young French chemist. But now the commercial materials applied in the field of emergency signs, luminous paints in highway, airport, building and ceramics, textile printing, textile fibers, dial plate of glowing watch, warning signs and escaping route way are not sulfides, but Eu doped aluminates ($SrAl_2O_4$: Eu^{2+}, Dy^{3+} *etc.*), since they are more safe, chemically stable and no radiation. It is notable that powder-form LPPs have more advantages in these applications than bulk-form LPPs, such as mixed into the pigment or glaze coated onto ceramic surface, even though the bulk-form LPPs have larger afterglow intensity and longer persistent duration than powder-form LPPs.[3, 21]

Phosphorescent studies in Turkey have been done by Karasu and his co-workers.[303] The studies included the production of phosphorescent pigments and their applications in ceramic materials. And then, phosphorescent ceramics and glasses were produced by adding phosphorescent pigment in the producing process. Compared to the common materials, these products could glow in the dark after ceasing the excitation lights. These materials were free from radioactivity, nontoxic and harmless. The certain level bright emergency lighting can guide people evacuate orderly under emergency and reduce confusion other than energy-saving. The application of phosphorescent ceramics and glasses in the domestic houses and public buildings can not only decorate and beauty the houses and working environment, but also can bring more conveniences to residents with its glow in the dark.

6.2 Optical storage, sensor and detector

A storage phosphor is exposed to high-energy radiation, such as x-ray or ultraviolet (UV) light. A part of excitation energy will be stored in this phosphor by capturing charge carriers (electrons or holes) into traps. The stored energy can then be liberated by thermal, optical or mechanical force, resulting in stimulated emissions from the emitting centers in such phosphors. With the assistance of thermal disturbance, the captured electrons can be sequentially released from the traps, leading to long persistent phosphorescence, while a fast heating will empty the traps and exhaust the captured electrons, resulting in a

thermos-luminescence. In addition, photons and mechanical strains are also the important induction force to release the captured electrons. Thermo, photo, and mechano-stimulated storage phosphors exhibiting thermo-luminescence (TL), photo-stimulated luminescence (PSL) and mechanouminescence (ML) phenomenon can act as excellent imaging plates, temperature sensor, stress sensor, and high energy-ray detector for the important information write-in and read-out.[192, 236, 304, 305]

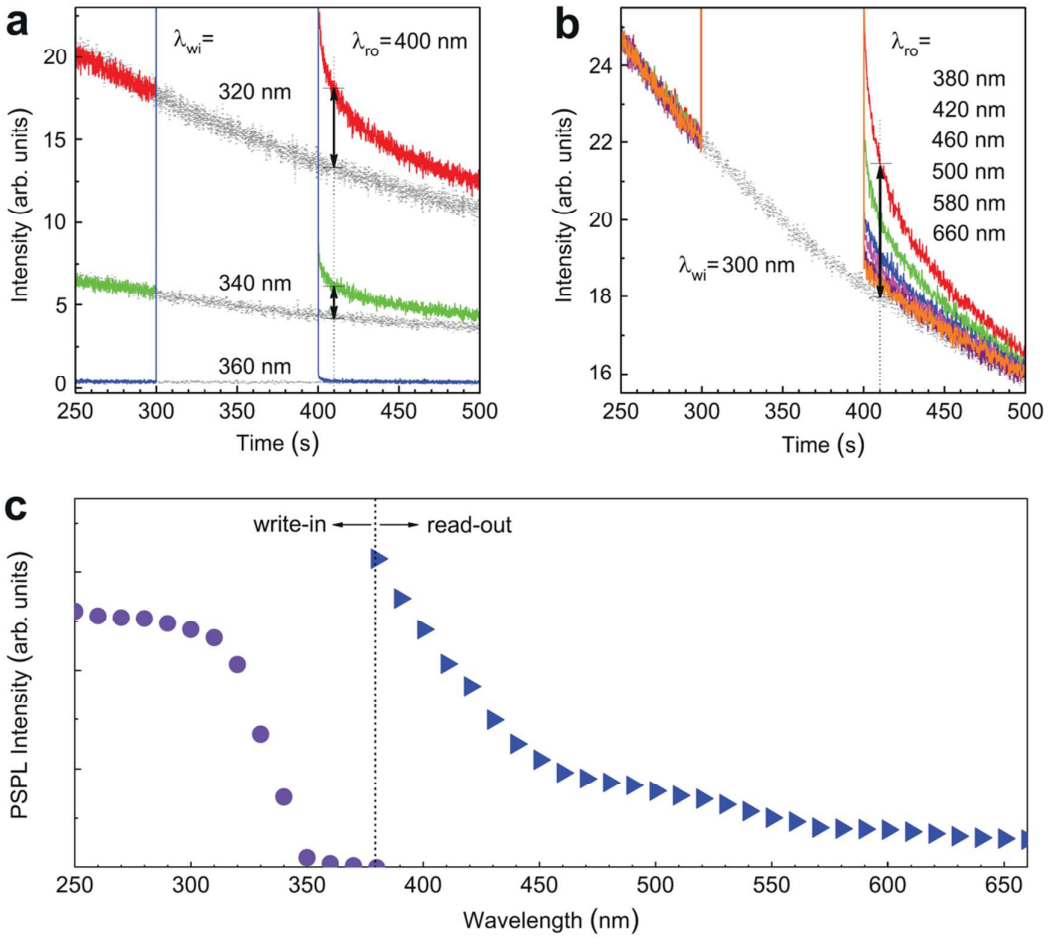

Fig. 21 Optical write-in and read-out spectra for photostimulated luminescence and phosphorescence in $LiGa_5O_8:Cr^{3+}$. (a) Persistent luminescence decay curves monitored at 716 nm with (colored solid-line curves) and without (grey dash-line curves) photo stimulation. The write-in wavelengths are 320 nm, 340 nm and 360 nm. The read-out wavelength is 400 nm. (b) Persistent luminescence decay curves monitored at 716 nm with (colored solid-line curves) and without (grey dash-line curve) photo stimulation. The write-in wavelength is 300 nm. The read-out wavelengths (vary between 380 nm and 660 nm. For the measurements in (a) and (b), the read-out process (i.e., stimulation) starts at 5 min after ceasing the write-in process (i.e., UV pre-irradiation). The vertical double arrowheads in (a) and (b) represent the PSP intensities. (c), PSP write-in spectrum (the ball curve in left panel) and read-out spectrum (the triangle curve in right panel) plotted according to the data from (a) and (b), respectively (reproduced with permission from ref. 139, copyright 2013, Nature Publication Group)

It is clear that the whole process requires the implementation of external force twice. For the application of imaging plates, the first exposure by an x-ray beam or a UV light “writes” a latent image in the form of trapped electrons on the phosphor plate. The number of trapped electrons is proportional to the amount of radiation absorbed locally and the latent image is optically readable within a certain time frame after the exposure. The second illumination with a light of appropriate wavelength, typically with an intense light with low energy, “reads” the image in the form of higher energy visible PSL signal. Most of the trapped electrons are extracted during the read-out process, and the residual electrons remaining on the phosphor plate can be erased through illumination with bright fluorescent light so that the plate can be used again. For example, Liu *et al.* reported the optical read-out phenomenon of PSL and photostimulated persistent phosphorescence (PSP) in NIR region, from a Cr^{3+}-doped $LiGa_5O_8$ NIR phosphor. An Intense signal with an emission peaking at 716 nm could be repeatedly obtained in a period of more than 1000 h when a UV light (250-360 nm) pre-irradiated $LiGa_5O_8$: Cr^{3+} phosphor was repeatedly stimulated by a light between 380-1000 nm (Fig. 21).[139]

The similar mechanism is also used in temperature and stress-sensor, high energy-ray detector *etc.* Due to the variation of the external field, the desired information can be extracted from one or several certain parameters. Therefore, these storage phosphors which exhibit the PSL, TL and ML phenomenon can be used as erasable and rewritable optical, electrical and magnetic memory, sensor and detector.

6.3 Biomedical applications

6.3.1 In vivo imaging

There is an increasing interest in the use of fluorescence in the biologically transparent window to drive the photonic bio-label for tracing the cancer cells.[7, 306] Advanced optical imaging has already become an indispensable tool in bio-science, bio-medicine and life-science over the last few decades, owing to its distinct merits of high sensitivity, portability, non-invasiveness, and time effectiveness.[2, 76] To date, various advanced fluorescent tags such as fluorescent dyes, metal nanoparticles, semiconductor quantum dots, upconversion nanoparticles and long phosphorescent phosphors have been proposed and successfully applied to in vivo bio-imaging.[307]

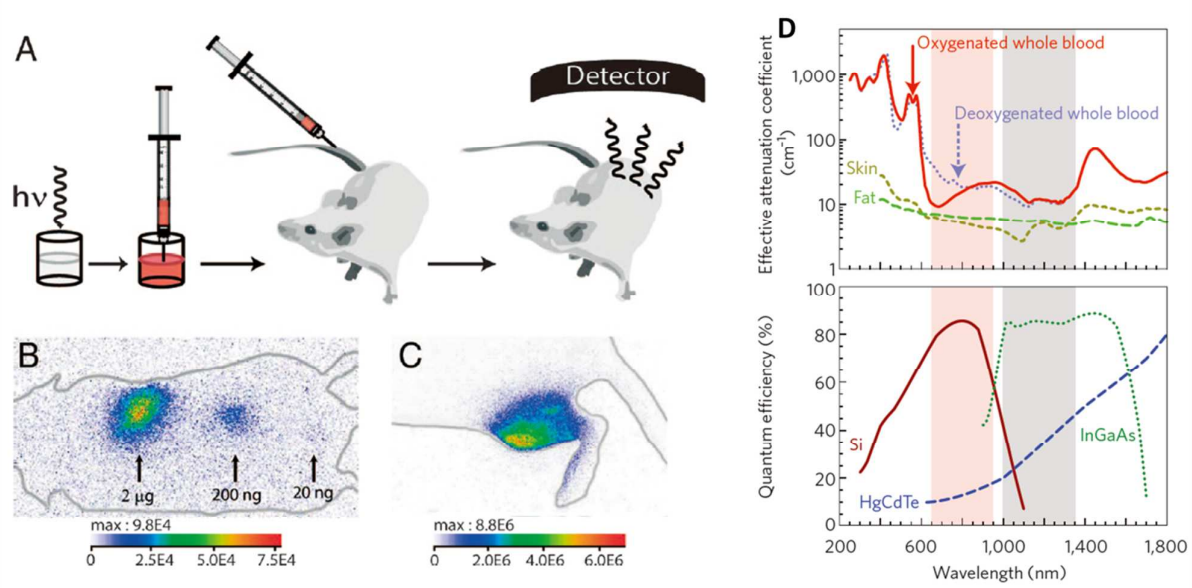

Fig. 22 (A) A suspension containing a proper amount of NPPs is excited with a 6W UV lamp and is directly injected to an anesthetized mouse. The signal is then acquired with an intensified charge-coupled device (CCD) camera. (B) Image of the injections of NPPs. The acquisition was performed during the 2 min after injection. (C) Image of an intramuscular injection corresponding to a 90s acquisition (reproduced with permission from ref. 85, copyright 2009, Proceedings of the National Academy of Sciences). (D) Optical windows in biological tissues. Top: These plots of effective attenuation coefficient (on a log scale) versus wavelength show that absorption and scattering from oxygenated blood, deoxygenated blood, skin and fatty tissue is lowest in either the first (pink shaded area) or second (grey) near-infrared window. Bottom: Sensitivity curves for typical cameras based on silicon (Si), indium gallium arsenide (InGaAs) or mercury cadmium telluride (HgCdTe) sensors. Si and InGaAs cameras are sensitive within the first and second near-infrared windows, respectively, whereas HgCdTe is most sensitive at longer wavelengths (reproduced with permission from ref. 308, copyright 2009, Nature Publication Group).

Therein, LPPs are unique and have already proven their superiority over other labels, since their emission lifetime is sufficiently long to permit late time-gated imaging.[3] Especially for the phosphorescent phosphors in the region of the biologically transparent window (650–1350 nm), they successfully avoid the challenging requirement of high-intensity illumination during the signal collection, which often leads to decreased signal-to-noise ratio and increased photon-induced deterioration of analytes.[309, 310] But now, optical imaging technique employing LPPs as labels stagnates, since the existing LPPs only have visible afterglow-emitting. Generally speaking, living tissues contain the strong UV-VIS absorbers, such as skin, fat, water, lipids oxyhemoglobin and deoxyhemoglobin that prove challenging for optical imaging. To overcome these barriers, intense researches have focused on developing highly sensitive and efficient fluorescent labels that function in first and second biologically transparent window (NIR I, 650–950 nm, and NIR II, 1050–1350 nm). NIR light in first transparency window can penetrate biological tissues more efficiently than visible light, yet the second region has even lower absorption and scattering therefore offers more efficient tissue penetration (Fig.

22D).[43, 308]

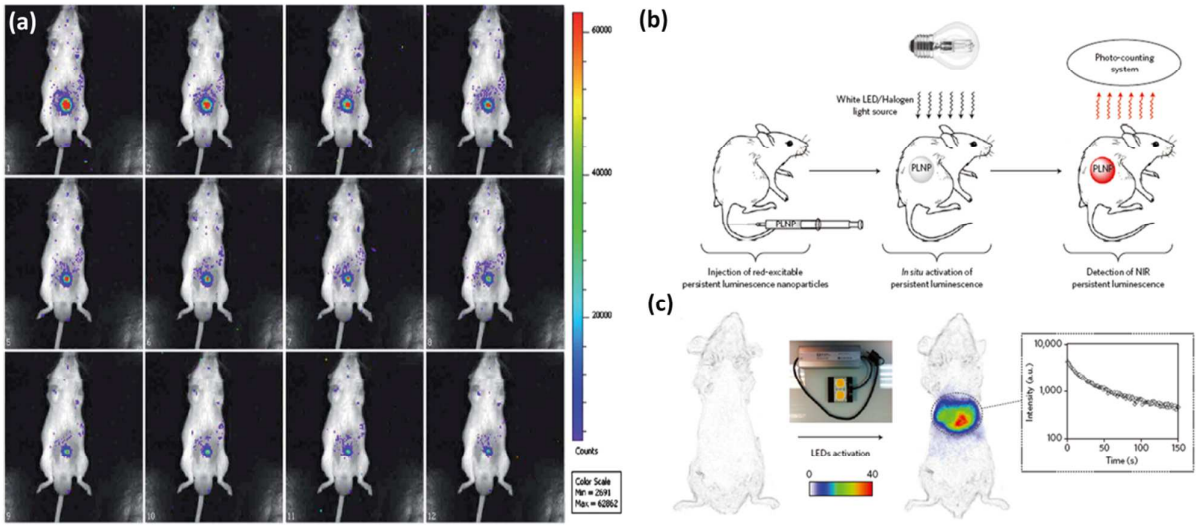

Fig. 23 (a) Optical imaging *in vivo*, 60 s acquisition at intervals of every 5 min over 1 h (reproduced with permission from ref. 42, copyright 2012, Royal Society of Chemistry). (b)-(c) *In vivo* imaging with $ZnGa_2O_4$-based NPPs (reproduced with permission from ref. 11, copyright 2014, Nature Publications Group). (b) A schematic representation of *in vivo* imaging after *in situ* activation of NPPs. (c) The detection of NPPs after *in vivo* activation.

In 2009, Quentin *et al.* first developed an alternative optical imaging technique by using persistent luminescent nanoparticles (NPPs) suitable for small animal imaging (Fig. 22A-C).[85] These nanoparticles could be excited before injection, and their *in vivo* distribution can be followed in real-time for more than 1 h without the need for any external illumination source. They also showed that these NPPs were easily amenable to chemical surface modification. This opened a whole area of potential applications for biological applications. Li *et al.* synthesized new promising long afterglow nanospheres with a narrow size distribution by using mesoporous silica nanospheres as morphology-controlling templates. The as-prepared afterglow nanospheres had a nominal composition of $SiO_2/SrMgSi_2O_6$: 1%Eu, 2%Dy. After the surface was modified with amino groups, grafted by PEG–COOH and irradiated with 365 nm UV light for 10 min, the afterglow signal could be observed in real time for more than 1 h in a live mouse after peritoneal injection (Fig. 23a).[42]

Thomas *et al.* introduced a new generation of optical nanolabels, based on chromium doped zinc gallate, whose persistent luminescence could be activated *in vivo* through living tissues using highly penetrating low energy NIR photons (Fig. 23b-c).[11] They demonstrated the signal from persistent luminescence remained largely detectable 2 h after the end of ultraviolet excitation, and gently decayed until complete extinction. After 15 h, the animals were irradiated with an orange/red LED source. Mice were then immediately placed on their back under the photon-counting system for persistent luminescence acquisition. Such a simple illumination through living tissues with visible light was sufficient to activate persistent luminescence of zinc gallate nanocrystals and retrieve an intense signal, even in deep tissues. Activation of the nanoparticles under the LED source was carried out to restore persistent luminescence signal after longer periods (4 h and 6 h post injection). A major accumulation of stealth nanoparticles within liver was observed 6 h after the injection.

Such distributed imaging with a wide view of field is not only utilized to realize the body imaging, but also can be employed to extract the information of local tissue, for instance, cell imaging, tissue imaging and targeted imaging. Our group demonstrated an efficient anti-Stokes fluorescent label with incoherent (Fig. 24d-e) or coherent (Fig. 24a-c) excitation and the clear deep tissue imaging by employing pork as the vehicle. Actually this deep tissue imaging provided important information of penetration depth as the reference to set up a new bio-imaging model.[15]

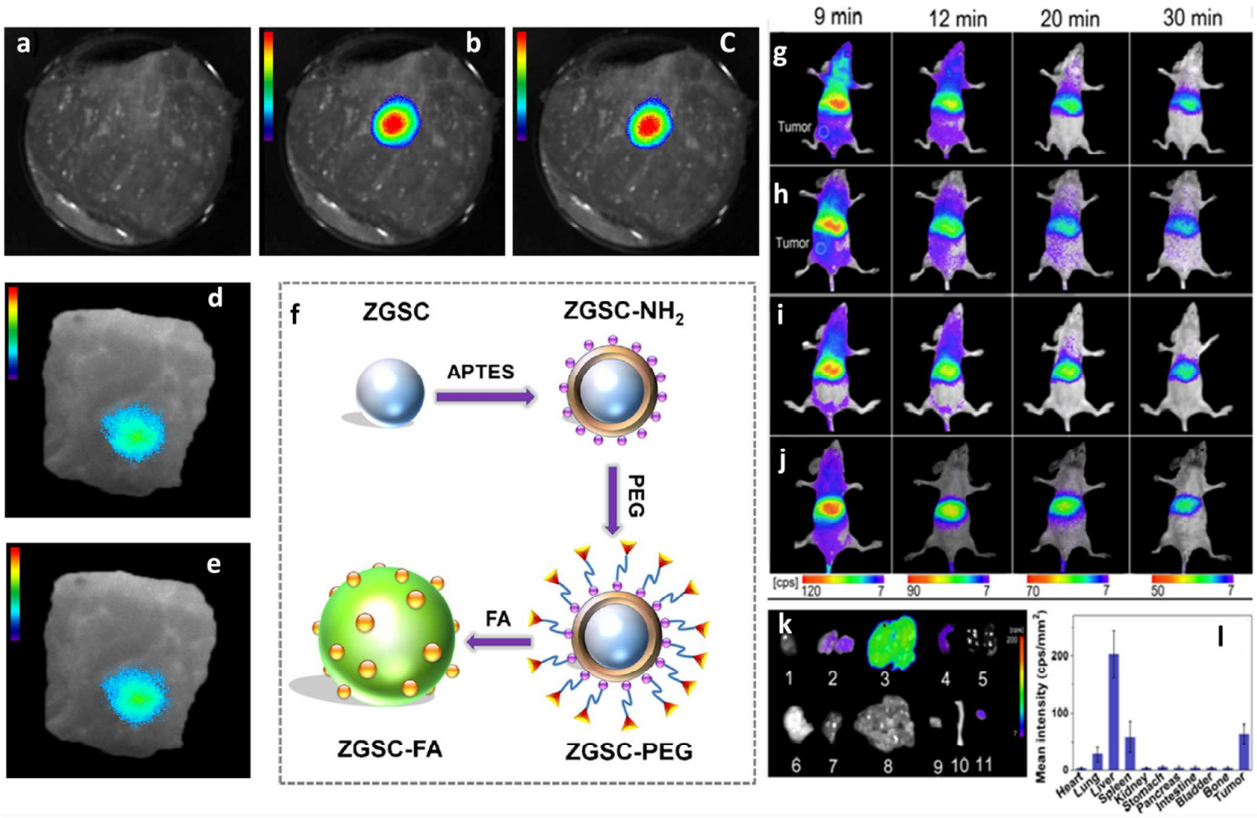

Fig. 24 (a)-(c) Long persistent phosphorescent and photo-stimulated luminescent tissues imaging of pork tissue under the excitation of 980 LD. (d)-(e) Long persistent phosphorescent and photo-stimulated luminescent tissues imaging of pork tissue under the excitation of 800 nm LED. (f) Schematic illustration for the synthesis of FA-ZGSC nanoparticles. (g)-(l) In vivo NIR images of U87MG tumor-bearing mice. (white circles locate the tumor site): (g, h) and normal mice, (i, j) after intravenous injection of PEG-NPPs (g, i) and RGD-NPPs (h, j) (0.4 mg, 10 min irradiation with a 254 nm UV lamp before injection). (k) Representative ex vivo NIR optical images of isolated organs and tumor from a U87MG tumor-bearing mouse at 6 h post-intravenous injection of RGD-NPPs (0.4 mg): (1) heart, (2) lung, (3) liver, (4) spleen, (5) kidney, (6) stomach, (7) pancreas, (8) intestine, (9) bladder, (10) bone, (11) tumor. (l) Semi-quantification of RGD-NPPs in the isolated organs and tumor of the mice, error bars represent one standard deviation of triplicate measurements from individual animals (reproduced with permission from ref. 2, copyright 2013, American Chemical Society).

Targetable bio-labels became more and more important, because the detection and trace of tumor cells at an early stage represents a most powerful weapon against cancer.[54] A typical strategy to develop tumor-specific nanolabels has focused on the synthesis of targeting ligands conjugated nanomaterials, which will efficiently bind the specific protein overexpressed on cancer cells.[33] Folic acid (FA) and RGD *etc.* have emerged as an attractive specific ligand for targeted cancer imaging. For example, folate receptors (FRs) were the highly selective tumor labels overexpressed in many of the human cancerous cells, such as, endometrial, lung, mesothelioma, brain, ovarian and breast carcinomas cell, *etc.* FRs was a kind of cysteine-rich cell-surface glycoproteins that bind FA with high affinity to mediate cellular uptake of FA.

Our group recently synthesized the FA-conjugated $Zn_{1.1}Ga_{1.8}Sn_{0.1}O_4$: Cr^{3+} (ZGSC) nanoparticles with NIR LPP for targeted optical imaging of cancer cells (Fig. 24f). These nanoparticles showed the easy dispersibility, small-size, good crystallinity, and remarkable long persistent luminescence over 10 h in the NIR region. The surface modification by coating the activated functional group of NH_2, PEG and FA, ensured the functionalized targeted imaging. The functionalized nanoparticles exhibited highly selective tumor localization, and cause an enabling long-term, real-time, reliable deep-tissues/cell/*in vivo* imaging with high resolution and signal to noise ratio.[45] Yan *et al.* synthesized the functional Pr^{3+}/Cr^{3+} co-doped NIR nanoparticles with super long lasting afterglow (>360 h) for in vivo bio-imaging (Fig. 24g-i). To evaluate the targeting capability of RGD-conjugated functionalized phosphorescent nanoparticles, they performed the targeted cell imaging and *in vivo* tumor imaging. The results indicated the conjugated polypeptide with the function of navigation offered the opportunity to accurately trace the cancer cell due to the high affinity of RGD-conjugated functionalized phosphorescent nanoparticles to integrin $\alpha_v\beta_3$ on tumor vasculature.[2]

6.3.2 *Bio-detection*

LPP is not only chosen as the optical label to trace the cancer cells, but also as the bio-probe to monitor and identify the variation of biotic habitat.[311] Ascorbic acid (AA) is an essential micronutrient required for numerous physiological and biochemical functions in the human body and is a potent water-soluble antioxidant capable of readily scavenging a number of reactive species and effectively protecting other biomolecules from oxidative damage. The oxidative damage to lipids, DNA, and proteins are implicated in many chronic diseases, such as cardiovascular disease, cancer, and cataracts. In addition, a variety of epidemiologic studies and clinical trials show that AA is associated with a reduction in the incidence of chronic disease and mortality. A nanoprobe was successfully applied for imaging reactive species *in vivo* without external excitation. Tang *et al.* developed a novel nanoprobe for determination and screening of ascorbic acid (AA) in living cells and *in vivo* by using CoOOH-modified persistent luminescence nanoparticles. Based on the specific reaction of CoOOH and AA, that could detect and image AA in living cells and *in vivo*. NPPs were employed as the optical unit, and CoOOH nanoflakes were used as the quencher. Because the emission spectrum of NPPs overlaped with the absorption spectrum of CoOOH nanoflakes, the afterglow of the NPPs could be efficiently quenched by CoOOH via Forster resonance energy transfer (FRET). In the presence of AA, the CoOOH nanoflakes on the surface of the PLNPs were reduced to Co^{2+} and the phosphorescence of PLNPs was restored with the relative amounts of AA. The details of this strategy were described in Figure 25. Moreover, detection and imaging of AA in living cells and *in vivo* without external excitation could be achieved because of the long-lasting afterglow nature, which allowed the removal of autofluorescence and scattering of light from biological matrixes produced by in situ excitation.[50]

α-fetoprotein (AFP) is the serum biomarker of hepatocellular carcinoma (HCC), which is the sixth most common cancer worldwide in terms of numbers of cases and has almost the lowest survival rates because of its very poor prognosis. Serum levels of AFP often increase under conditions such as periods of rapid liver cancer cell growth, cirrhosis, and chronic active hepatitis as well as carbon tetrachloride intoxication. Therefore, detection of serum levels of AFP can lead to early diagnosis of HCC. To probe AFP with high selectivity and sensitivity, Yan *et al.* designed a fluorescence resonance energy transfer (FRET) inhibition assay for AFP excreted during cancer cell growth using water-soluble functionalized NPPs based on Eu^{2+} and Dy^{3+}-doped $Ca_{1.86}Mg_{0.14}ZnSi_2O_7$. Polyethyleneimine-coated NPPs were conjugated with AFP antibody-coated gold nanoparticles as a sensitive and specific persistent photoluminescence probe for detection of AFP in serum samples and imaging of AFP excreted during cancer cell growth.[4]

Recently, they also reported a novel multimodal nanoprobe based on the gadolinium complexes functionalized PLNPs (Gd(III)-NPPs) for in vivo MRI and NIR luminescence imaging. The Gd(III)-NPPs not only exhibit a relatively higher longitudinal relaxivity over the commercial Gd(III)-diethylenetriamine pentaacetic acid complexes but also keep the super long persistent luminescence. The prepared Gd(III)-PLNPs multimodal nanoprobe offers great potential for MRI/optical imaging in vivo.[46]

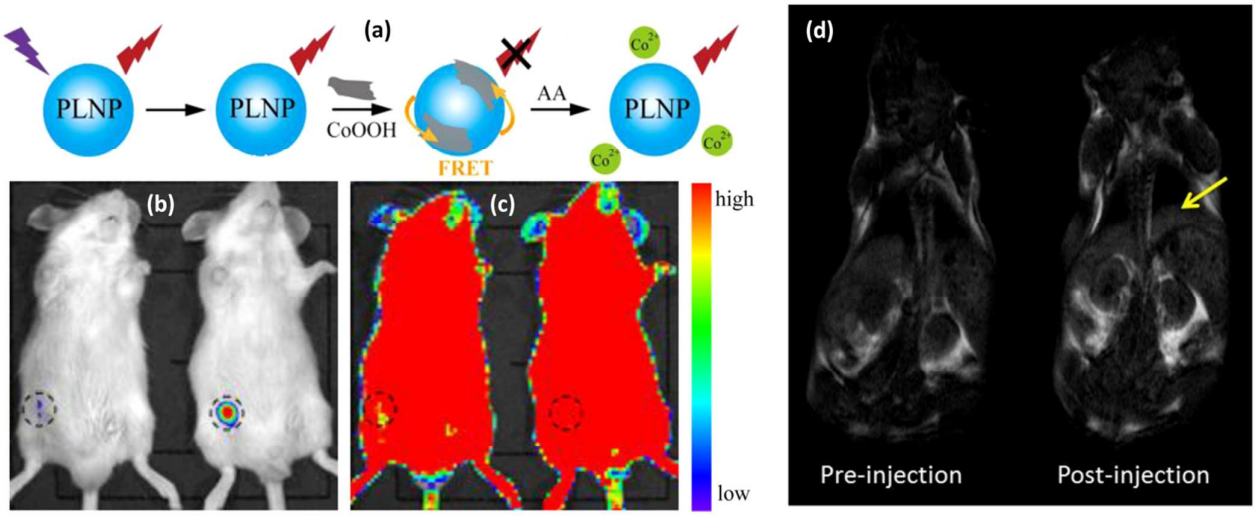

Fig. 25 (a) Schematic illustration of the design for AA detection using CoOOH-modified NPPs. (b) Optical image of the mouse treated with 0.1 mL of normal saline and the nanoprobe (left) and the mouse treated with 0.1 mL of AA (0.1 mol/L) and the nanoprobe (right) without excitation. (c) Optical image of the same mice in (A) using 420 nm excitation. The concentration of the nanoprobe was 1 mg/mL. The Optical signals were collected at 520±20 nm. The center of the black dashed circle is the injection site. The color change from purple to red for the intensity bar represents the increase in the luminescence intensity (reproduced with permission from ref. 50, copyright 2014, American Chemical Society). (d) In vivo T_1-weighted MR images of the mouse before and after intravenous injection of Gd(III)-NPPs (0.3 mg); the yellow arrow indicates the liver (reproduced with permission from ref. 46, copyright 2014, American Chemical Society)

6.4 Photocatalysis

Extensive researches show TiO_2 is an intriguing material for photocatalytic environmental purification under ultraviolet illumination. One of the most significant environmental applications of TiO_2 is to decompose volatile organic compounds to clear the air. However, the photocatalytic degradation efficiency on the surface of TiO_2 particles is still low, which is due to the fast recombination rate of photo-generated electron-hole pairs and the finity of the light source. TiO_2 could only absorb the light only in the near-UV region, which was about 3% of the solar spectrum. In order to slow down the electron-hole pairs, broaden the photo-response of TiO_2 and enhance interfacial charge-transfer efficiency, several approaches have been proposed, including transition metals doping, coupled semiconductor systems, noble metals deposition, and rare earth ions doping.[19]

Li *et al.* proposed an approach to improve the photocatalytic efficiency of TiO_2, which attempted to synthesize composed TiO_2 catalysts using long phosphorescent phosphor as material support. In this case, the goal was achieved by associating an afterglow-emitting center to support the continuous photocatalytic reaction after turning off the light (Fig. 26a). The coupling of the LPPs with photocatalysts was a conceptually simple and promising approach to improve the performance of photocatalytic reactions. $CaAl_2O_4$: Eu, Nd @TiO_2 photocatalyst, which generated the luminescence with the short wavelength of 440 nm and long emission lifetime >10h, was beneficial for the gaseous photocatalytic reaction and complete degradation of acetaldehyde and NO pollutants. To date, the reported afterglow-assisted TiO_2 photocatalysts mainly consisted of Eu^{2+}-doped LPPs, such as $CaAl_2O_4$: (Eu, Nd)/ $TiO_{2-x}N_y$, $SrAl_2O_4$: Eu, Dy/$TiO_{2-x}N_y$, $Sr_4Al_{14}O_{25}$: (Eu, Dy)/$TiO_{2-x}N_y$ composites, $CaAl_2O_4$: (Eu, Nd)/TiO_2/Fe_2O_3, and $Sr_2MgSi_2O_7$: Eu, Dy/$TiO_{2-x}N_y$.[19, 312-316]

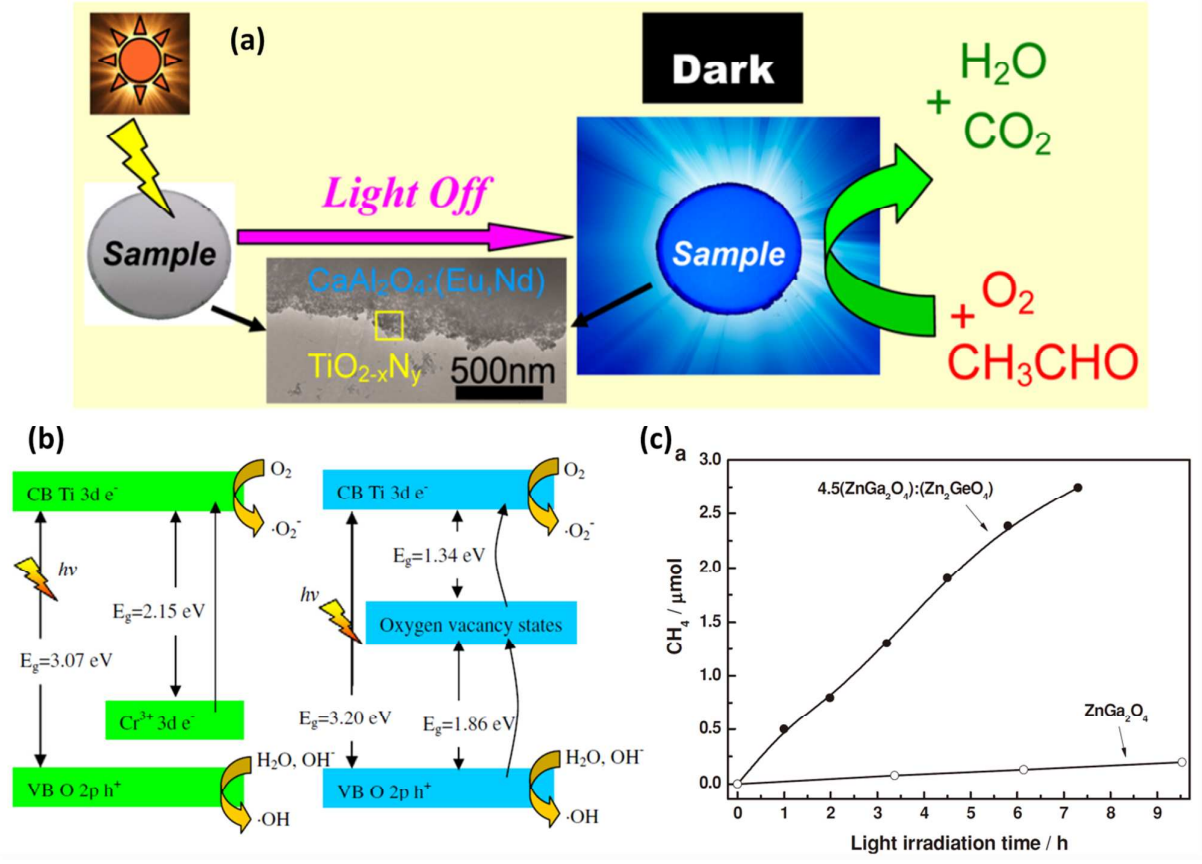

Fig. 26 (a) Schematic illustration of setup for the photocatalytic experiment (reproduced with permission from ref. 316, copyright 2012, American Chemical Society). (b) Schematic band structures of (left) Cr-doped $SrTiO_3$ and (right) nonstoichiometric $SrTiO_3$ (Sr/Ti=1.67) (reproduced with permission from ref. 19, copyright 2013, Elsevier). (c) Gaseous product generation over the zinc gallogermanate solid solution and $ZnGa_2O_4$ as a function of irradiation time: CH_4 (reproduced with permission from ref. 6, copyright 2013, Wiley).

In addition to the composed catalysts, some nanoparticles with long persistent phosphorescence or the host of LPPs were directly proposed as the photocatalysts. The related materials used to degrade gaseous acetaldehyde pollutants in air were $BaZrO_3$: Mg^{2+},[269] $ZnxGa_2O_3(0.8<x<1)$,[226] Ga_2O_3: Cr^{3+},[75] Zn^{2+}, $SrTiO_3$: Cr,[313] nonstoichiometric $SrTiO_3$ (Sr/Ti=1.67) and zinc gallogermanate solid solution[6] *etc.* One of the most famous was zinc gallogermanate solid solution, which is the host of super long NIR persistent phosphor $Zn_3Ga_2Ge_2O_{10}$: Cr^{3+} (Fig. 26c).[6] It was widely acceptable that constructing a solid-solution photocatalyst was beneficial to enhance the photocatalytic activity of a given semiconductor photocatalyst. The solid solutions would exhibit better performance than the single components. A series of solid-solution photocatalysts, such as $AgGa_{1-x}Al_xO_2$, $(AgIn)_xZn_{2(1-x)}S_2$, $Zn_{1-x}Cu_xS$ *etc.* have been developed and successfully applied in photocatalytic water splitting and pollutant degradation. Zinc gallogermanate solid solution had a light-hole effective mass band gap narrowing, which was beneficial to improving hole mobility, and thus enhancing the ability of photocatalyst in water oxidation to provide protons for CO_2 photoreduction, i.e. converting CO_2 and H_2O into CH_4 and O_2.

6.5 Solar cell

He *et al.* described a CdS sensitized solar cells (DSSC) device assisted by $SrAl_2O_4$: Eu^{2+}, Dy^{3+} LPPs. $SrAl_2O_4$: Eu^{2+}, Dy^{3+} phosphors can convert near ultraviolet light from 250 to 400 nm with lower sensitivity to the solar cell to green light at which matched the peak absorption region of the most common dye N719 (Fig. 27a). TiO_2 nanoparticle-based DSSCs were modified by depositing a layer of $SrAl_2O_4$: Eu^{2+}, Dy^{3+} on top of the TiO_2 nanoparticle layer to prepare working electrodes of the DSSCs. $SrAl_2O_4$: Eu^{2+}, Dy^{3+} red-shifted the short UV wavelengths into the main absorption range of the dye commonly used in DSSCs. $SrAl_2O_4$: Eu^{2+}, Dy^{3+} layer acted as a light-scattering layer to reduce the loss of visible light. The open-circuit voltage was found to be higher in the modified DSSCs. The performance of modified DSSC device was improved compared with the cell using a working electrode without this phosphor layer. An overall 13% improvement in conversion efficiency of modified DSSCs was achieved due to the presence of the phosphor layer.[35, 38, 61]

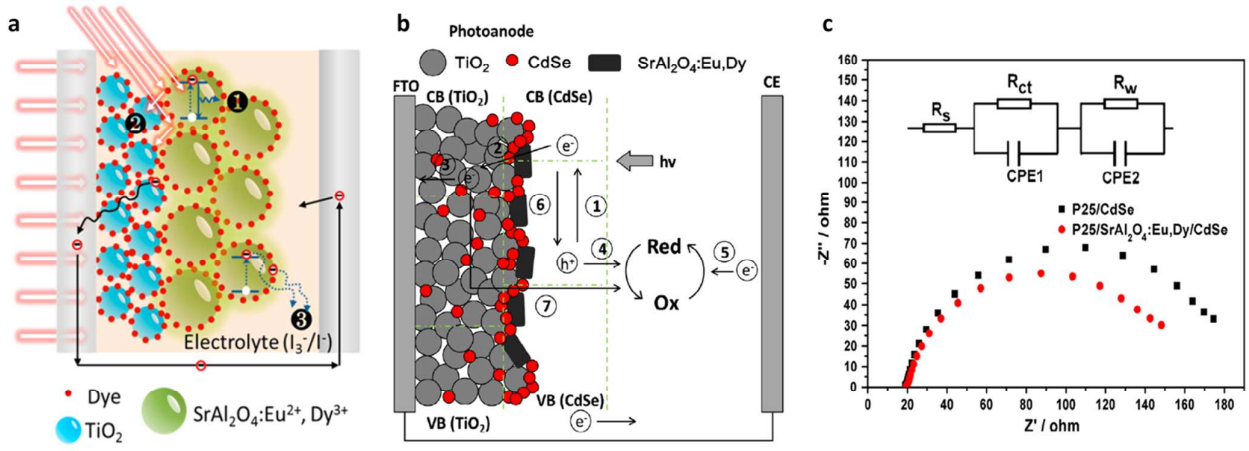

Fig. 27 (a) Working mechanism of the DSSC with FTO/TiO_2/phosphor multilayered electrode. Three functions of $SrAl_2O_4$: Eu^{2+}, Dy^{3+} in the working process of a DSSC: (1) down-converting of UV light to green light, (2) scattering of light, and (3)recombination centers (reproduced with permission from ref. 38, copyright 2013, American Chemical Society). (b) Schematic diagram of the structure and working mechanism of QDSSCs with P25/$SrAl_2O_4$: Eu, Dy/CdSe electrode (reproduced with permission from ref. 317, copyright 2014, Elsevier). (c) Electrochemical impedance spectra of the cells with P25/CdSe and P25/$SrAl_2O_4$: Eu, Dy/CdSe electrodes. (reproduced with permission from ref. 317, copyright 2014, Elsevier).

Sun *et al.* fabricated an efficient bifunctional structured layer composed of LPPs $SrAl_2O_4$: Eu, Dy on top of a transparent layer of nanocrystalline TiO_2 and CdSe solar cells.[318] The photovoltaic performances showed that higher power conversion efficiency was achieved for the cell with $SrAl_2O_4$: Eu, Dy at one sun illumination (AM 1.5G, 100mWcm^{-2}), which was an increase of 48% compared to the cell without $SrAl_2O_4$: Eu, Dy. After one sun

illumination for 1 min and subsequent turned off of the light source, the cell with $SrAl_2O_4$: Eu, Dy still showed an weak conversion efficiency under dark condition due to the irradiation by the long persistent light. In addition, they also introduced $Sr_4Al_{14}O_{25}$: Eu, Dy LPPs into the TiO_2 photoanode of CdS quantum dot-sensitized solar cells (QDSSCs) as both scattering and down converting layer (Fig. 27b).[317] The results showed that the cell with $Sr_4Al_{14}O_{25}$: Eu, Dy achieved an increase of 38% power conversion efficiency compared to the cell without $Sr_4Al_{14}O_{25}$: Eu, Dy. The similar strategy was also found to increase the conversion efficiency of a crystalline silicon photovoltaic module by using $SrAl_2O_4$: Eu^{2+}, Dy^{3+}/SiO_2 composite films as spectral down-shifting shifter instead of the bare glass substrate.

7. Prospective and conclusions

In this work, we provided a full-scale review of LPPs from fundamental aspects to all possible scientific application. The main objective of this contribution is to present the very recently-made advances in the field of synthesis techniques, characterizations, afterglow mechanisms, applications and materials of LPPs. Although substantial and rapid progress has been made in these fields, there are still many areas that need additional work, including but not limited to: (a) achieving the control of new-wavelength emission and excitation band; (b) tailoring luminous efficacy, initial afterglow intensity and persistent duration; (c) exploring new activators and matrix; (d) structuring the standard afterglow model; (e) developing the new technology of synthesizing nanocrystals; (f) Opening up the novel multi-functional application fields.

(1) Synthesizing route: It is fundamentally important to develop general and economic protocols for the synthesis, surface modification and bio-conjugation of high-quality phosphorescent nano-biolabels, which are optimized for bio-applications without any concerns of biocompatibility, stability and long-term toxicity. The reported methods are, in our opinion, not the most perfect and suitable for the production of afterglow nanoparticles, because they still don't completely get away from universal crystal nucleus aggregation and growth under a higher synthesized temperature. As shown above, all of the reported routes cannot simultaneously well control the shape, morphology and homogeneity of nanoparticles as well as the long persistent duration. The involved process just partly improves the properties of afterglow nanophosphors.

(2) Characterization and mechanism analysis: Another big problem lies in the potential of data modeling of afterglow mechanism by developing the advanced characterization technique. The investigations and analysis towards the species, concentration and depth of traps as well as the probability and rate of electrons being captured and released should be conducted as a whole by means of multiple measurement methods. For a fundamental physical and chemical insight into the afterglow mechanism, much detailed information needs to be revealed and extracted, i.e. what are the species of defects, how to assess and then precisely control the trap concentration, how do the defects work in the matrix and what is the process of electrons being captured and released. The energy level diagram model proposed by Dorenbos can successfully explain and predict some of the observed phenomena especially in rare-earth doped phosphor systems. It is still necessary to study how defects involve in the long persistent phosphorescence process.

(3) Application: Long persistent phosphorescence should be given some more considerations in advanced scientific applications. One key area will be the integration of long persistent phosphorescence with other peculiarities or special characteristics (such as magnetization, photo-thermal response) to open the door to novel multifunctional applications, i.e. tracing and therapy, or tracing and monitoring cancer cell in the field of bio-medicine and life science. If possible, it is highly desirable to develop a NIR phosphorescent bioprobes, monitoring the level of toxin or nutrient substance in the living body. On the other hand, LPPs over a wide range of wavelengths and long persistent time offers more possibilities for incorporation in solar photovoltaic, optical information storage and displays, environmental sensor and monitor, photocatalysis on flexible platforms.

(4) Material design: Firstly, the emission waveband of NIR LPPs should be further improved and extended to the second transparency window in order to increase their detection sensitivity for diverse disease biomarkers. The considerable strategies of extending waveband to long-wavelength region are altering the emission center, tailoring the crystal field surrounding the activator as well as transferring the persistent

energy of sensitizers to acceptors. Secondly, although NIR LPPs have been extensively investigated, more basic studies of activators' species (transition metal or rare earth ions) should be carried out because the known numbers of NIR phosphorescent centers are very low. Thirdly, for NIR LPPs, Cr^{3+} and gallate are commonly used as the optimized emission center and host. The predominance of Cr^{3+}-activated gallates might suggest that only gallates can be used as the hosts in Cr^{3+}-doped NIR LPPs. Such dependence would result in the trapping and de-trapping processes being closely associated with the crystalline structure or energy band structure of gallates. It is challenging to identify the nature of defects and it is difficult to predict the actual effectiveness and impact of intrinsic and substituted defects in gallates because comparison with Cr^{3+}-doped non-gallate phosphors is missing. In addition, can we expect the discovery of new and even better persistent luminescent matrix, apart from the gallates, aluminates and the silicates, *etc.*? Fourthly, some UV-VIS light-excitation LPPs are available, but there is still plenty of room for the improvement of excitation waveband, since red-NIR light offers much higher excitation efficiency *in vivo* due to the lower absorbance of biological tissue and higher depth of penetration. Though Pan et al ever proposed a kind of LPPs which can be excited under the visible light, it is obvious that the dominant afterglow excitation peak in the afterglow excitation spectrum still locates at ultraviolet region, approximately matching the absorption around interband transition. For major oxide-LPPs, the dominant afterglow excitation band all follows this rule. Thus, it is very necessary to develop the phosphors with narrow energy band gap, which can be excited by long-wavelength light. (Oxy) sulfides and (oxy) nitrides may be considered as the effective VIS-NIR-excitation LPPs because of the relatively narrow energy band gap.

(5) In order to be able to compare experimental results obtained by different research groups on identical or different phosphor compositions, there is an urgent need for a more standardized way of measuring and defining LPPs properties. The existing definition of 0.32 mcd/m^2, is not applicable for UV or NIR-emitting persistent phosphors, where the luminous emission is zero by default and no clear definition exists for the afterglow duration. Therefore, a uniform standard is needed for quantifying the performance of UV-NIR emitters. A possible suggestion is looking for one device which has the stable response from ultraviolet to NIR region.

In brief, a great number of new concepts and novel materials are still in the research stage. Some of them may lead to much better afterglow properties in the coming decades. In our opinion, a long way is still ahead in achieving the goal from a "top-down" strategy, which is a concept of guiding the materials design based on a clear mechanism and model. Energy band structure of host and activators, valence and redox ability of dopants, crystal structure of host, even the volatility of raw materials have been proposed as the important and considerable factors in such strategy. The prospects of reaching this goal have been found to be satisfactory and more interesting in the back drop of emergence of different and new promising materials and concepts.

8. Acknowledgements

The authors thank Dr. Lakshmi Narayana for the English check. This work is financially supported by National Natural Science Foundation of China (Grant Nos. 51132004, 51072754, 51472091), Guangdong Natural Science Foundation (Grant Nos. S2011030001349, 2014A030310444), National Basic Research Program of China (Grant Nos. 2011CB808100), China Postdoctoral Science Foundation (Grant Nos. 2015M570707) and Fundamental Research Funds for the Central Universities (Grant Nos. 2013ZM0001, 2015ZM089). This work is also supported by the Open Fund of the State Key Laboratory of High Field Laser Physics (Shanghai Institute of Optics and Fine Mechanics).

9. References

1. H. Terraschke and C. Wickleder, *Chem. Rev.*, 2015, 115, 11352-11378.
2. A. Abdukayum, J. T. Chen, Q. Zhao and X. P. Yan, *J. Am. Chem. Soc.*, 2013, 135, 14125-14133.
3. T. Maldiney, A. Lecointre, B. Viana, A. Bessiere, M. Bessodes, D. Gourier, C. Richard and D. Scherman, *J. Am. Chem. Soc.*, 2011, 133, 11810-11815.

4. B. Y. Wu, H. F. Wang, J. T. Chen and X. P. Yan, *J. Am. Chem. Soc.*, 2011, 133, 686-688.
5. S. Hirata, K. Totani, J. X. Zhang, T. Yamashita, H. Kaji, S. R. Marder, T. Watanabe and C. Adachi, *Adv. Funct. Mater.*, 2013, 23, 3386-3397.
6. S. C. Yan, J. J. Wang, H. L. Gao, N. Y. Wang, H. Yu, Z. S. Li, Y. Zhou and Z. G. Zou, *Adv. Funct. Mater.*, 2013, 23, 1839-1845.
7. Z. G. Yi, X. L. Li, Z. L. Xue, X. Liang, W. Lu, H. Peng, H. R. Liu, S. J. Zeng and J. H. Hao, *Adv. Funct. Mater.*, 2015, 25, 7119-7129.
8. Y. Y. Gong, G. Chen, Q. Peng, W. Z. Yuan, Y. J. Xie, S. H. Li, Y. M. Zhang and B. Z. Tang, *Adv. Mater.*, 2015, 27, 6195-6201.
9. M. Palner, K. Y. Pu, S. Shao and J. H. Rao, *Angew. Chem. Int. Edit.*, 2015, 54, 11477-11480.
10. Z. M. Tao, G. S. Hong, C. Shinji, C. X. Chen, S. Diao, A. L. Antaris, B. Zhang, Y. P. Zou and H. J. Dai, *Angew. Chem. Int. Edit.*, 2013, 52, 13002-13006.
11. T. Maldiney, A. Bessiere, J. Seguin, E. Teston, S. K. Sharma, B. Viana, A. J. J. Bos, P. Dorenbos, M. Bessodes, D. Gourier, D. Scherman and C. Richard, *Nat. Mater.*, 2014, 13, 418-426.
12. Z. W. Pan, Y. Y. Lu and F. Liu, *Nat. Mater.*, 2012, 11, 58-63.
13. Y. Li, Y. Y. Li, R. C. Chen, K. Sharafudeen, S. F. Zhou, M. Gecevicius, H. H. Wang, G. P. Dong, Y. L. Wu, X. X. Qin and J. R. Qiu, *NPG. Asia. Mate.r*, 2015, 7, e180.
14. H. Lin, J. Xu, Q. M. Huang, B. Wang, H. Chen, Z. B. Lin and Y. S. Wang, *Acs Appl. Mater. Inter.*, 2015, 7, 21835-21843.
15. Y. Li, S. F. Zhou, G. P. Dong, M. Y. Peng, L. Wondraczek and J. R. Qiu, *Sci. Rep.*, 2014, 4, 04059.
16. B. C. Cheng, L. T. Fang, Z. D. Zhang, Y. H. Xiao and S. J. Lei, *J. Phys. Chem. C*, 2011, 115, 1708-1713.
17. Y. X. Zhuang, J. Ueda, S. Tanabe and P. Dorenbos, *J. Mater. Chem. C*, 2014, 2, 5502-5509.
18. D. Q. Chen, Y. Chen, H. W. Lu and Z. G. Ji, *Inorg. Chem.*, 2014, 53, 8638-8645.
19. H. H. Li, S. Yin, Y. H. Wang and T. Sato, *Rsc. Adv.*, 2012, 2, 3234-3236.
20. M. Allix, S. Chenu, E. Veron, T. Poumeyrol, E. A. Kouadri-Boudjelthia, S. Alahrache, F. Porcher, D. Massiot and F. Fayon, *Chem. Mater.*, 2013, 25, 1600-1606.
21. H. J. Guo, Y. H. Wang, W. B. Chen, W. Zeng, S. C. Han, G. Li and Y. Y. Li, *J. Mater. Chem. C*, 2015, 3, 11212-11218.
22. J. Xu, D. Q. Chen, Y. L. Yu, W. J. Zhu, J. C. Zhou and Y. S. Wang, *Chem-Asian. J*, 2014, 9, 1020-1025.
23. L. C. V. Rodrigues, J. Holsa, M. Lastusaari, M. C. F. C. Felinto and H. F. Brito, *J. Mater. Chem. C*, 2014, 2, 1612-1618.
24. B. Wang, H. Lin, J. Xu, H. Chen, Z. B. Lin, F. Huang and Y. S. Wang, *Inorg. Chem.*, 2015, 54, 11299-11306.
25. W. Zeng, Y. H. Wang, S. C. Han, W. B. Chen, G. Li, Y. Z. Wang and Y. Wen, *J. Mater. Chem. C*, 2013, 1, 3004-3011.
26. Y. Q. Li, Y. H. Wang, Y. Gong, X. H. Xu and M. J. Zhou, *Opt. Express*, 2010, 18, 24853-24858.
27. A. Lecointre, A. Bessiere, A. J. J. Bos, P. Dorenbos, B. Viana and S. Jacquart, *J. Phys. Chem. C*, 2011, 115, 4217-4227.
28. F. Liu, Y. J. Liang and Z. W. Pan, *Phys. Rev. Lett.*, 2014, 113. 177401 (1)-(5).
29. Z. Li, Y. Zhang, X. Wu, L. Huang, D. Li, W. Fan and G. Han, *J. Am. Chem. Soc.*, 2015, 137, 5304-5307.
30. L. C. V. Rodrigues, H. F. Brito, J. Holsa, R. Stefani, M. C. F. C. Felinto, M. Lastusaari, T. Laamanen and L. A. O. Nunes, *J. Phys. Chem. C*, 2012, 116, 11232-11240.
31. Y. L. Wu, Y. Li, X. X. Qin, R. C. Chen, D. K. Wu, S. J. Liu and J. R. Qiu, *J. Alloy. Compd.*, 2015, 649, 62-66.
32. Y. Luo and Z. G. Xia, *J. Phys. Chem. C*, 2014, 118, 23297-23305.
33. T. Maldiney, C. Richard, J. Seguin, N. Wattier, M. Bessodes and D. Scherman, *Acs Nano.*, 2011, 5, 854-862.
34. X. H. Xu, Y. H. Wang, Y. Gong, W. Zeng and Y. Q. Li, *Opt. Express*, 2010, 18, 16989-16994.
35. S. X. Lian, Y. Qi, C. Y. Rong, L. P. Yu, A. L. Zhu, D. L. Yin and S. B. Liu, *J. Phys. Chem. C*, 2010, 114, 7196-7204.
36. X. D. Shi, L. Sho, M. Z. Li, J. Hou, L. F. Chen, C. Q. Ye, W. Z. Shen, L. Jiang and Y. L. Song, *Acs Appl. Mater. Inter.*, 2014, 6, 6317-6321.
37. J. Wang, H. R. Zhang, B. F. Lei, Z. G. Xia, H. W. Dong, Y. L. Liu, M. T. Zheng and Y. Xiao, *J. Mater. Chem. C*, 2015, 3, 4445-4451.
38. W. He, T. S. Atabaev, H. K. Kim and Y. H. Hwang, *J. Phys. Chem. C*, 2013, 117, 17894-17900.
39. E. J. Guidelli, O. Baffa and D. R. Clarke, *Sci. Rep.*, 2015, 5, 14004.
40. T. Z. Zhan, C. N. Xu, H. Yamada, Y. Terasawa, L. Zhang, H. Iwase and M. Kawai, *Rsc. Adv.*, 2012, 2, 328-332.
41. J. Xu, J. Ueda, K. Kuroishi and S. Tanabe, *Scripta. Mater*, 2015, 102, 47-50.
42. Z. J. Li, H. W. Zhang, M. Shi, J. S. Sheng and H. X. Hu, *J. Mater. Chem.*, 2012, 22, 24713-24720.
43. B. H. Dong, C. Y. Li, G. C. Chen, Y. J. Zhang, Y. Zhang, M. J. Deng and Q. B. Wang, *Chem. Mater.*, 2013, 25, 2503-2509.
44. Y. Gong, Y. H. Wang, Y. Q. Li, X. H. Xu and W. Zeng, *Opt. Express*, 2011, 19, 4310-4315.

45. Y. Li, R. C. Chen, Y. Y. Li, K. Sharafudeen, S. J. Liu, D. K. Wu, Y. L. Wu, X. X. Qin and J. R. Qiu, *Microchim. Acta*, 2015, 182, 1827-1834.
46. A. Abdukayum, C. X. Yang, Q. Zhao, J. T. Chen, L. X. Dong and X. P. Yan, *Anal. Chem.*, 2014, 86, 4096-4101.
47. H. H. Li, S. Yin, Y. H. Wang, T. Sekino, S. W. Lee and T. Sato, *J. Mater. Chem. A*, 2013, 1, 1123-1126.
48. D. A. Hammer, M. Therien, I. Dmochowski, N. Kamat and G. Robbins, *Abstr. Pap. Am. Chem. S.*, 2010, 239, 374.
49. A. Bessiere, S. K. Sharma, N. Basavaraju, K. R. Priolkar, L. Binet, B. Viana, A. J. J. Bos, T. Maldiney, C. Richard, D. Scherman and D. Gourier, *Chem. Mater.*, 2014, 26, 1365-1373.
50. N. Li, Y. H. Li, Y. Y. Han, W. Pan, T. T. Zhang and B. Tang, *Anal. Chem.*, 2014, 86, 3924-3930.
51. Z. H. Zou, J. Wu, H. Xu, J. C. Zhang, Z. P. Ci and Y. H. Wang, *J. Mater. Chem. C*, 2015, 3, 8030-8038.
52. A. Bessiere, A. Lecointre, R. A. Benhamou, E. Suard, G. Wallez and B. Viana, *J. Mater. Chem. C*, 2013, 1, 1252-1259.
53. N. Basavaraju, K. R. Priolkar, D. Gourier, S. K. Sharma, A. Bessiere and B. Viana, *Phys. Chem. Chem. Phys.*, 2015, 17, 1790-1799.
54. T. Maldiney, M. U. Kaikkonen, J. Seguin, Q. L. de Chermont, M. Bessodes, K. J. Airenne, S. Yla-Herttuala, D. Scherman and C. Richard, *Bioconjugate. Chem.*, 2012, 23, 472-478.
55. G. S. Hong, J. T. Robinson, Y. J. Zhang, S. Diao, A. L. Antaris, Q. B. Wang and H. J. Dai, *Angew. Chem. Int. Edit.*, 2012, 51, 9818-9821.
56. Z. Li, Y. Zhang, X. Wu, X. Wu, R. Maudgal, H. Zhang and G. Han, *Adv. Sci.*, 2015, 2, 1500001.
57. K. Szczodrowski, A. Chruscinska, J. Barzowska, K. Przegietka, K. Anders, R. Piramidowicz and M. Grinberg, *Rsc. Adv.*, 2015, 5, 65236-65244.
58. C. Rosticher, B. Viana, G. Laurent, P. Le Griel and C. Chaneac, *Eur. J. Inorg. Chem.*, 2015, 3681-3687.
59. S. K. Kandpal, B. Goundie, J. Wright, R. A. Pollock, M. D. Mason and R. W. Meulenberg, *Acs Appl. Mater. Inter.*, 2011, 3, 3482-3486.
60. H. F. Li, W. Z. Sun, Y. L. Jia, T. F. Ma, J. P. Fu, D. Li, S. Zhang, L. H. Jiang, R. Pang and C. Y. Li, *Chem-Asian. J*, 2015, 10, 2361-2367.
61. H. C. Sun, L. K. Pan, G. Zhu, X. Q. Piao, L. Zhang and Z. Sun, *Dalton. T.*, 2014, 43, 14936-14941.
62. Y. Li, S. F. Zhou, Y. Y. Li, K. Sharafudeen, Z. J. Ma, G. P. Dong, M. Y. Peng and J. R. Qiu, *J. Mater. Chem. C*, 2014, 2, 2657-2663.
63. Y. H. Jin, Y. H. Hu, H. Duan, L. Chen and X. J. Wang, *Rsc. Adv.*, 2014, 4, 11360-11366.
64. Y. Li, X. Du, K. Sharafudeen, C. X. Liao and J. R. Qiu, *Spectrochim. Acta. A*, 2014, 123, 7-11.
65. S. Chenu, E. Veron, C. Genevois, A. Garcia, G. Matzen and M. Allix, *J. Mater. Chem. C*, 2014, 2, 10002-10010.
66. K. Korthout, K. Van den Eeckhout, J. Botterman, S. Nikitenko, D. Poelman and P. F. Smet, *Phys. Rev. B*, 2011, 84, 085140.
67. G. Li, Y. H. Wang, W. Zeng, W. B. Chen, S. C. Han, H. J. Guo and X. C. Wang, *Dalton. T.*, 2015, 44, 17572-17578.
68. R. Pang, W. Z. Sun, J. P. Fu, H. F. Li, Y. L. Jia, D. Li, L. H. Jiang, S. Zhang and C. Y. Li, *Rsc. Adv.*, 2015, 5, 82704-82710.
69. S. A. Zhang, Y. H. Hu, L. Chen, G. F. Ju, T. Wang and Z. H. Wang, *Rsc. Adv.*, 2015, 5, 37172-37179.
70. J. P. Shi, H. X. Fu, X. Sun, J. S. Shen and H. W. Zhang, *J. Mater. Chem. B*, 2015, 3, 635-641.
71. D. Kulesza and E. Zych, *J. Phys. Chem. C*, 2013, 117, 26921-26928.
72. X. L. Wang and H. Riesen, *Rsc. Adv.*, 2015, 5, 85506-85510.
73. K. K. Satapathy, G. C. Mishra, R. S. Kher and S. J. Dhoble, *Rsc. Adv.*, 2015, 5, 79391-79396.
74. Y. X. Zhuang, J. Ueda and S. Tanabe, *Appl. Phys. Lett.*, 2014, 105. 191904 (1)-(4).
75. X. S. Wang, W. S. Li, J. Q. Situ, X. Y. Ying, H. Chen, Y. Jin and Y. Z. Du, *Rsc. Adv.*, 2015, 5, 12886-12889.
76. J. P. Shi, X. Sun, J. L. Li, H. Z. Man, J. S. Shen, Y. K. Yu and H. W. Zhang, *Biomaterials*, 2015, 37, 260-270.
77. X. Yi, Z. T. Chen, S. Ye, Y. Li, E. H. Song and Q. Y. Zhang, *Rsc. Adv.*, 2015, 5, 49680-49687.
78. J. Xu, Z. H. Ju, X. P. Gao, Y. Q. An, X. L. Tang and W. S. Liu, *Inorg. Chem.*, 2013, 52, 13875-13881.
79. W. Z. Yan, F. Liu, Y. Y. Lu, X. J. Wang, M. Yin and Z. W. Pan, *Opt. Express*, 2010, 18, 20215-20221.
80. Y. L. Wu, Y. Li, X. X. Qin, R. C. Chen, D. K. Wu, S. J. Liu and J. R. Qiu, *Spectrochim. Acta. A*, 2015, 151, 385-389.
81. J. Xu, S. Tanabe, A. D. Sontakke and J. Ueda, *Appl. Phys. Lett.*, 2015, 107, 081903 (1)-(4).
82. H. Kanno, K. Noda and K. Matsui, *Chem. Phys. Lett.*, 2013, 580, 103-107.
83. H. D. Luo, A. J. J. Bos, A. Dobrowolska and P. Dorenbos, *Phys Chem Chem Phys*, 2015, 17, 15419-15427.
84. Z. G. Xia, Q. Li, G. W. Li, M. Xiong and L. B. Liao, *J Cryst Growth*, 2011, 318, 958-961
85. Q. le Masne de Chermont, C. Chaneac, J. Seguin, F. Pelle, S. Maitrejean, J. P. Jolivet, D. Gourier, M. Bessodes and D.

Scherman, *U. S. A. PNAS*, 2007, 104, 9266-9271.

86. Y. Teng, J. J. Zhou, S. N. Khisro, S. F. Zhou and J. R. Qiu, *Mater. Chem. Phys.*, 2014, 147, 772-776.
87. B. C. Cheng, Z. D. Zhang, Z. H. Han, Y. H. Xiao and S. J. Lei, *Crystengcomm*, 2011, 13, 3545-3550.
88. C. Hou, Y. Wang, H. Zhu and L. C. Zhou, *J Mater Chem B*, 2015, 3, 2883-2891.
89. G. P. Dong, X. D. Xiao, L. L. Zhang, Z. J. Ma, X. Bao, M. Y. Peng, Q. Y. Zhang and J. R. Qiu, *J. Mater. Chem.*, 2011, 21, 2194-2203.
90. F. Yoshimura, K. Nakamura, F. Wakai, M. Hara, M. Yoshimoto, O. Odawara and H. Wada, *Appl. Surf. Sci.*, 2011, 257, 2170-2175.
91. P. F. Smet, N. Avci, K. Van den Eeckhout and D. Poelman, *Opt. Mater. Express*, 2012, 2, 1306-1313.
92. J. H. Lim, B. N. Kim, Y. Kim, S. Kang, R. J. Xie, I. S. Chong, K. Morita, H. Yoshida and K. Hiraga, *Appl. Phys. Lett.*, 2013, 102, 031104 (1)-(4).
93. L. Jin, H. Y. Zhang, R. Q. Pan, P. Xu, J. C. Han, X. H. Zhang, Q. Yuan, Z. H. Zhang, X. J. Wang, Y. Wang and B. Song, *Nano. Lett.*, 2015, 15, 6575-6581.
94. P. Gluchowski, W. Strek, M. Lastusaari and J. Holsa, *Phys. Chem. Chem. Phys.*, 2015, 17, 17246-17252.
95. N. Basavaraju, K. R. Priolkar, D. Gourier, A. Bessiere and B. Viana, *Phys. Chem. Chem. Phys.*, 2015, 17, 10993-10999.
96. M. Milde, S. Dembski, A. Osvet, M. Batentschuk, A. Winnacker and G. Sextl, *Mater. Chem. Phys.*, 2014, 148, 1055-1063.
97. A. Bessière, A. Lecointre, K. R. Priolkar and D. Gourier, *J. Mater. Chem.*, 2012, 22, 19039-19046.
98. D. Wei, L. Qin, Y. Huang and H. J. Seo, *Ceram. Int.*, 2013, 39, 2383-2387.
99. Y.Y. Lu, F. Liu, Z. Gu and Z. Pan, *J. Lumin.*, 2011, 131, 2784-2787.
100. X. Fu, C. Liu, J. Shi, H. Man, J. Xu and H. Zhang, *Opt. Mater.*, 2014, 36, 1792-1797.
101. Y. Tian, P. Zhang, Z. Zheng and Y. Chai, *Mater. Lett.*, 2012, 73, 157-160.
102. P. Huang, Q. Zhang, C.-e. Cui and J. Li, *Opt. Mater.*, 2011, 33, 1252-1257.
103. D. C. Rodriguez Burbano, S. K. Sharma, P. Dorenbos, B. Viana and J. A. Capobianco, *Adv. Opt. Mater.*, 2015, 3, 551-557.
104. J. T. Kong, W. Zheng, Y. S. Liu, R. F. Li, E. Ma, H. M. Zhu and X. Y. Chen, *Nanoscale*, 2015, 7, 11048-11054.
105. Y.F. Xu, D. K. Ma, M.L. Guan, X.A. Chen, Q.Q. Pan and S.M. Huang, *J. Alloy. Compd.*, 2010, 502, 38-42.
106. D. Liu, C. e. Cui, P. Huang, L. Wang and G. Jiang, *J. Alloy. Compd.*, 2014, 583, 530-534.
107. S. Y. Xin, Y. H. Wang, P. Y. Dong, W. Zeng and J. Zhang, *J. Mater. Chem. C*, 2013, 1, 8156-8160.
108. Z. Li, J. Shi, H. Zhang and M. Sun, *Opt. Express*, 2014, 22, 10509-10518.
109. Z. K. Xu, G. T. Duan, H. W. Zhang, Y. Y. Wang, L. Xu and W. P. Cai, *Nanoscale*, 2015, 7, 14264-14271.
110. Z. J. Li, Y. J. Zhang, H. W. Zhang and H. X. Fu, *Micropor. Mesopor. Mat.*, 2013, 176, 48-54.
111. Y. Liu, S.-x. Liu, M.-w. Wang, W.-j. Li, T. Zhang and X. Zhang, *Int. J. Min. Met. Mater.*, 2010, 17, 347-352.
112. B. Cheng, H. Liu, M. Fang, Y. Xiao, S. Lei and L. Zhang, *Chem. Commun.*, 2009, 8, 944-946.
113. N. Y. Yu, F. Liu, X. F. Li and Z. W. Pan, *Appl. Phys. Lett.*, 2009, 95, 231110 (1)-(3).
114. Y. J. Li, M. W. Wang, L. D. Zhang, D. Gao and S. X. Liu, *Int. J. Min. Met. Mater.*, 2013, 20, 972-977.
115. H. H. Li, S. Yin and T. Sato, *Res. Chem. Intermediat.*, 2013, 39, 1501-1507.
116. M. Elsagh, M. Rajabi and E. Amini, *J. Mater. Sci-Mater. El*, 2014, 25, 1612-1619.
117. L. Yang, P. W. May, L. Yin, R. Brown and T. B. Scott, *Chem. Mater.*, 2006, 18, 5058-5064.
118. T. Maldiney, G. Sraiki, B. Viana, D. Gourier, C. Richard, D. Scherman, M. Bessodes, K. Van den Eeckhout, D. Poelman and P. F. Smet, *Opt. Mater. Express*, 2012, 2, 261-268.
119. L. L. Noto, O. M. Ntwaeaborwa, J. J. Terblans and H. C. Swart, *Powder. Technol.*, 2014, 256, 477-481.
120. T. Z. Zhan, C. N. Xu, H. Yamada, Y. Terasawa, L. Zhang, H. Iwase and M. Kawai, *Aip. Adv.*, 2012, 2.
121. K. Van den Eeckhout, P. F. Smet and D. Poelman, *Materials*, 2010, 3, 2536-2566.
122. K. Van den Eeckhout, D. Poelman and P. F. Smet, *Materials*, 2013, 6, 2789-2818.
123. J. Botterman and P. F. Smet, *Opt. Express*, 2015, 23, A868-A881.
124. H. Yamamoto and T. Matsuzawa, *J. Lumin.*, 1997, 72-4, 287-289.
125. T. Nakamura, K. Kaiya, N. Takahashi, T. Matsuzawa, C. C. Rowlands, V. Beltran-Lopez, G. M. Smith and P. C. Riedi, *J. Mater. Chem.*, 2000, 10, 2566-2569.
126. T. Aitasalo, P. Deren, J. Holsa, H. Jungner, J. C. Krupa, M. Lastusaari, J. Legendziewicz, J. Niittykoski and W. Strek, *J. Solid. State. Chem.*, 2003, 171, 114-122.

127. J. Holsa, T. Aitasalo, H. Jungner, M. Lastusaari, J. Niittykoski and G. Spano, *J. Alloy. Compd.*, 2004, 374, 56-59.
128. F. Clabau, X. Rocquefelte, S. Jobic, P. Deniard, M. H. Whangbo, A. Garcia and T. Le Mercier, *Chem. Mater.*, 2005, 17, 3904-3912.
129. P. Dorenbos, *J. Lumin.*, 2003, 104, 239-260.
130. P. Dorenbos, *J. Lumin.*,2005, 111, 89-104.
131. F. T. You, A. J. J. Bos, Q. F. Shi, S. H. Huang and P. Dorenbos, *Phys. Rev. B*, 2012, 85, 115101 (1)-(7).
132. L. C. V. Rodrigues, H. F. Brito, J. Holsa and M. Lastusaari, *Opt. Mater. Express*, 2012, 2, 382-390.
133. M. Lastusaari, A. J. J. Bos, P. Dorenbos, T. Laamanen, M. Malkamaki, L. C. V. Rodrigues and J. Holsa, *J. Therm. Anal. Calorim.*, 2015, 121, 29-35.
134. V. Kale, M. Lastusaari, J. Holsa and T. Soukka, *Rsc. Adv.*, 2015, 5, 35858-35865.
135. L. U. Khan, H. F. Brito, J. Holsa, K. R. Pirota, D. Muraca, M. C. F. C. Felinto, E. E. S. Teotonio and O. L. Malta, *Inorg. Chem.*, 2014, 53, 12902-12910.
136. A. J. J. Bos, N. R. J. Poolton, J. Wallinga, A. Bessiere and P. Dorenbos, *Radiat. Meas.*, 2010, 45, 343-346.
137. K. Ota, K. Hamada, R. Takemura, M. Ohmaki, T. Machi, K. Tanabe, M. Suzuki, A. Maeda and H. Kitano, *Phys. Rev. B*, 2009, 79, 134505 (1)-(11).
138. S. Tanabe, S. Watanabe, F. Saif and M. Matsuzawa, *Phys. Rev. A*, 2002, 65, 033420 (1)-(7).
139. F. Liu, W. Z. Yan, Y. J. Chuang, Z. P. Zhen, J. Xie and Z. W. Pan, *Sci. Rep.*, 2013, 3, 01554 (1)-(9).
140. J. H. Si, K. Kitaoka, J. R. Qiu, T. Mitsuyu and K. Hirao, *Opt. Lett.*, 1999, 24, 911-913.
141. J. R. Qiu, K. Kojima, K. Miura, T. Mitsuyu and K. Hirao, *Opt. Lett.*, 1999, 24, 786-788.
142. Y. Shimotsuma, P. G. Kazansky, J. R. Qiu and K. Hirao, *Phys. Rev. Lett.*, 2003, 91, 247405 (1)-(4).
143. J. R. Qiu, X. W. Jiang, C. S. Zhu, M. Shirai, J. Si, N. Jiang and K. Hirao, *Angew. Chem. Int. Edit.*, 2004, 43, 2230-2234.
144. P. F. Feng, J. C. Zhang, C. Q. Wu, X. Liu and Y. H. Wang, *Mater. Chem. Phys.*, 2013, 141, 495-501.
145. T. Wang, J. Gou, X. H. Xu, D. C. Zhou, J. B. Qiu and X. Yu, *Opt. Express*, 2015, 23, 12595-12604.
146. M. Yamaga, Y. Ohsumi and N. Kodama, *J. Ceram. Process. Res.*, 2013, 14, S52-S56.
147. D. Gourier, A. Bessiere, S. K. Sharma, L. Binet, B. Viana, N. Basavaraju and K. R. Priolkar, *J. Phys. Chem. Solids*, 2014, 75, 826-837.
148. A. Lecointre, R. Ait Benhamou, A. Bessiére, G. Wallez, M. Elaatmani and B. Viana, *Opt. Mater.*, 2011, 34, 376-380.
149. A. Bessiere, A. Lecointre, K. R. Priolkar and D. Gourier, *J. Mater. Chem.*, 2012, 22, 19039-19046.
150. R. Pang, Y. L. Jia, R. Zhao, H. F. Li, J. P. Fu, W. Z. Sun, L. H. Jiang, S. Zhang, C. Y. Li and Q. Su, *Dalton. T.*, 2014, 43, 9661-9668.
151. Y. Li, Y. Y. Li, K. Sharafudeen, G. P. Dong, S. F. Zhou, Z. J. Ma, M. Y. Peng and J. R. Qiu, *J. Mater. Chem. C*, 2014, 2, 2019-2027.
152. X. F. Liu, Y. B. Qiao, G. P. Dong, S. Ye, B. Zhu, Y. X. Zhuang and J. R. Qiu, *J. Electrochem. Soc.*, 2009, 156, P81-P84.
153. L. Zhang, C. Y. Li, S. B. Wang and Q. Su, *J. Lumin.*, 2007, 126, 551-555.
154. T. Nakanishi, Y. Katayama, J. Ueda, T. Honma, S. Tanabe and T. Komatsu, *J. Ceram. Soc. Jpn.*, 2011, 119, 609-615.
155. Y. Katayama, J. Ueda and S. Tanabe, *J. Lumin.*, 2014, 148, 290-295.
156. T. Nakanishi, K. Watanabe, J. Ueda, K. Fushimi, S. Tanabe and Y. Hasegawa, *J. Am. Ceram. Soc.*, 2015, 98, 423-429.
157. L. Pihlgren, T. Laihinen, L. C. V. Rodrigues, S. Carlson, K. O. Eskola, A. Kotlov, M. Lastusaari, T. Soukka, H. F. Brito and J. Holsa, *Opt. Mater.*, 2014, 36, 1698-1704.
158. M. Lastusaari, H. F. Brito, S. Carlson, J. Holsa, T. Laamanen, L. C. V. Rodrigues and E. Welter, *Phys. Scripta.*, 2014, 89, 044004 (1)-(3).
159. L. C. V. Rodrigues, R. Stefani, H. F. Brito, M. C. F. C. Felinto, J. Holsa, M. Lastusaari, T. Laamanen and M. Malkamaki, *J. Solid. State. Chem.*, 2010, 183, 2365-2371.
160. P. J. Wang, X. H. Xu, D. C. Zhou, X. Yu and J. B. Qiu, *Inorg. Chem.*, 2015, 54, 1690-1697.
161. J. C. Zhang, X. L. Ma, Q. S. Qin, L. R. Shi, J. Y. Sun, M. J. Zhou, B. T. Liu and Y. H. Wang, *Mater. Chem. Phys.*, 2012, 136, 320-324.
162. A. J. J. Bos, R. M. van Duijvenvoorde, E. van der Kolk, W. Drozdowski and P. Dorenbos, *J. Lumin.*, 2011, 131, 1465-1471.
163. F. T. You, A. J. J. Bos, Q. F. Shi, S. H. Huang and P. Dorenbos, *J. Phys-Condens. Mat.*, 2011, 23, 215502 (1)-(6).
164. P. F. Smet, K. Van den Eeckhout, A. J. J. Bos, E. van der Kolk and P. Dorenbos, *J. Lumin.*, 2012, 132, 682-689.
165. J. Botterman, K. Van den Eeckhout, A. J. J. Bos, P. Dorenbos and P. F. Smet, *Opt. Mater. Express*, 2012, 2, 341-349.
166. K. Van den Eeckhout, A. J. J. Bos, D. Poelman and P. F. Smet, *Phys. Rev. B*, 2013, 87, 045126 (1)-(11).

167. J. Fleniken, J. Wang, J. Grimm, M. J. Weber and U. Happek, *J. Lumin.*, 2001, 94, 465-469.
168. T. Katsumata, H. Kubo, S. Komuro and H. Aizawa, *J. Am. Ceram. Soc.*, 2014, 97, 1704-1707.
169. A. Wiatrowska and E. Zych, *J. Phys. Chem. C*, 2013, 117, 11449-11458.
170. T. Wang, W. J. Bian, D. C. Zhou, J. B. Qiu, X. Yu and X. H. Xu, *J. Phys. Chem. C*, 2015, 119, 14047-14055.
171. H. F. Brito, M. C. F. C. Felinto, J. Holsa, T. Laamanen, M. Lastusaari, M. Malkamaki, P. Novak, L. C. V. Rodrigues and R. Stefani, *Opt. Mater. Express*, 2012, 2, 420-431.
172. H. L. Li, Y. H. Wang, W. X. Zhang, X. S. Wang and H. Zhao, *Acta. Phys. Sin-Ch. Ed.*, 2012, 61 1823.
173. J. Trojan-Piegza and E. Zych, *J. Phys. Chem. C*, 2010, 114, 4215-4220.
174. A. Wiatrowska and E. Zych, *Materials*, 2014, 7, 157-169.
175. J. Trojan-Piegza, J. Niittykoski, J. Holsa and E. Zych, *Chem. Mater.*, 2008, 20, 2252-2261.
176. Y. Y. Lu, F. Liu, Z. J. Gu and Z. W. Pan, *J. Lumin.*, 2011, 131, 2784-2787.
177. B. P. Chandra, *J. Lumin.*, 2010, 130, 2218-2222.
178. W. H. Shen, X. H. Xu, B. H. Zhang, T. Wang, J. B. Qiu and X. Yu, *Ecs Solid State Lett.*, 2015, 4, R31-R33.
179. J. Y. Kuang, Y. L. Liu and J. X. Zhang, *J. Mater. Sci.*, 2006, 41, 5500-5503.
180. Y. H. Lin, Z. T. Zhang, Z. L. Tang, X. X. Wang, J. Y. Zhang and Z. S. Zheng, *J. Eur. Ceram. Soc.*, 2001, 21, 683-685.
181. M. Zheng, X. Chen, B. Lei, Y. Xiao, R. Liu, H. Zhang, H. Dong, Y. Liu and X. Liu, *Ecs Solid State Lett.*, 2013, 2, R19-R22.
182. Y. H. Wang, Y. Gong, X. H. Xu and Y. Q. Li, *J. Lumin.*, 2013, 133, 25-29.
183. Z. F. Yang, Y. H. Hu, L. Chen and X. J. Wang, *Opt. Mater.*, 2013, 35, 1264-1267.
184. Y. Gong, Y. H. Wang, Y. Q. Li and X. H. Xu, *J. Electrochem. Soc.*, 2010, 157, J208-J211.
185. J. Yan, L. X. Ning, Y. C. Huang, C. M. Liu, D. J. Hou, B. B. Zhang, Y. Huang, Y. Tao and H. B. Liang, *J. Mater. Chem. C*, 2014, 2, 8328-8332.
186. Y. Li, Y. Wang, Y. Gong, X. Xu and F. Zhang, *Acta Mater.*, 2011, 59, 3174-3183.
187. H. He, R. L. Fu, X. F. Song, R. Li, Z. W. Pan, X. R. Zhao, Z. H. Deng and Y. G. Cao, *J. Electrochem. Soc.*, 2010, 157, J69-J73.
188. G. F. Ju, Y. H. Hu, L. Chen, X. J. Wang and Z. F. Mu, *J. Lumin.*, 2014, 146, 102-108.
189. W. B. Dai, M. Zhou, Z. Y. Xian and L. K. Zeng, *Rsc. Adv.*, 2014, 4, 25470-25478.
190. A. Madej and E. Zych, *Rsc. Adv.*, 2015, 5, 104441-104450.
191. Y. Li, B. H. Li, C. C. Ni, S. X. Yuan, J. Wang, Q. Tang and Q. Su, *Chem-Asian. J*, 2014, 9, 494-499.
192. X. Liu, J. H. Zhang, X. Zhang, Z. D. Hao, J. Qiao and X. L. Dong, *Opt. Lett.*, 2013, 38, 148-150.
193. L. L. Jiang, S. G. Xiao, X. L. Yang, X. A. Zhang, X. H. Liu, B. Y. Zhou and X. L. Jin, *Mater. Sci. Eng. B-Adv*, 2013, 178, 123-126.
194. L. Lin, C. S. Shi, Z. F. Wang, W. P. Zhang and M. Yin, *J. Alloy. Compd.*, 2008, 466, 546-550.
195. Y. Gong, Y. H. Wang, X. H. Xu, Y. Q. Li, S. Y. Xin and L. R. Shi, *Opt. Mater.*, 2011, 33, 1781-1785.
196. W. B. Dai, *Rsc. Adv.*, 2014, 4, 11206-11215.
197. J. S. Zhang, B. J. Chen, J. S. Sun, X. P. Li, L. H. Cheng and H. Y. Zhong, *J Phys D Appl Phys*, 2012, 45, 1632-1637.
198. M. Yamaga, Y. Ohsumi, T. Nakayama and T. P. J. Han, *Opt. Mater. Express*, 2012, 2, 413-419.
199. X. J. Wang, D. D. Jia and W. M. Yen, *J. Lumin.*, 2003, 102, 34-37.
200. Y. H. Chen, X. R. Cheng, M. Liu, Z. M. Qi and C. S. Shi, *J. Lumin.*, 2009, 129, 531-535.
201. I. P. Sahu, P. Chandrakar, R. N. Baghel, D. P. Bisen, N. Brahme and R. K. Tamrakar, *J. Alloy. Compd.*, 2015, 649, 1329-1338.
202. X. Wei, M. K. Lei, X. X. Luo and Z. G. Xiao, *Spectrosc. Spect. Anal.*, 2008, 28, 41-46.
203. M. A. Tshabalala, F. B. Dejene, S. S. Pitale, H. C. Swart and O. M. Ntwaeaborwa, *Physica B*, 2014, 439, 126-129.
204. G. Li, Y. H. Wang, S. C. Han, W. Zeng, W. B. Chen and Y. Gong, *Ecs J. Solid State Sc.*, 2013, 2, R161-R164.
205. Y. Y. Zhang, R. Pang, C. Y. Li, C. Y. Zang and Q. A. Su, *J. Rare. Earth.*, 2010, 28, 705-708.
206. X. F. Qu, L. X. Cao, W. Liu, G. Su, P. P. Wang and I. Schultz, *Mater. Res. Bull.*, 2012, 47, 1598-1603.
207. S. F. Lai, Z. W. Yang, H. J. Wu, J. Y. Liao, J. B. Qiu, Z. G. Song, Y. Yang and D. C. Zhou, *Optoelectron Adv. Mat.*, 2015, 9, 48-52.
208. X. H. Xu, J. B. Qiu and Y. Xue, *Ecs Solid State Lett.*, 2013, 2, R9-R11.
209. X. Xu, Y. H. Wang, W. Zeng, Y. Gong and B. T. Liu, *J. Am. Ceram. Soc.*, 2011, 94, 3632-3635.
210. C. K. Chang and D. L. Mao, *Thin Solid Films*, 2004, 460, 48-52.
211. R. X. Zhong, J. H. Zhang, X. Zhang, S. Z. Lu and X. J. Wang, *Appl. Phys. Lett.*, 2006, 88, 201916.
212. Y. Teng, J. J. Zhou, Z. J. Ma, M. M. Smedskjaer and J. R. Qiu, *J. Electrochem. Soc.*, 2011, 158, K17-K19.
213. D. D. Jia, X. J. Wang and W. M. Yen, *Phys. Rev. B*, 2004, 69, 235113 (1)-(5).

214. Z. F. Mu, Y. H. Wang, Y. H. Hu, H. Y. Wu, L. Y. Deng, W. Xie, C. J. Fu and C. X. Liao, *Acta. Phys. Sin-Ch. Ed.*, 2011, 60.
215. J. Ueda, K. Aishima, S. Nishiura and S. Tanabe, *Appl. Phys. Express.*, 2011, 4, 042602 (1)-(3).
216. J. Xu, J. Ueda, Y. X. Zhuang, B. Viana and S. Tanabe, *Appl. Phys. Express.*, 2015, 8, 042602.
217. J. Ueda, K. Kuroishi and S. Tanabe, *Appl. Phys. Express.*, 2014, 7, 062201 (1)-(3).
218. X. H. Xu, Y. H. Wang, X. Yu, Y. Q. Li and Y. Gong, *J. Am. Ceram. Soc.*, 2011, 94, 24-27.
219. D. Jia, R. S. Meltzer, W. M. Yen, W. Jia and X. Wang, *Appl. Phys. Lett.*, 2002, 80, 1535-1537.
220. S. Zhang, C. Y. Li, R. Pang, L. H. Jiang, L. L. Shi and Q. Su, *J. Lumin.*, 2011, 131, 2730-2734.
221. B. Liu, C. S. Shi and Z. M. Qi, *Appl. Phys. Lett.*, 2005, 86, 191111.
222. Z. F. Mu, Y. H. Hu, Y. H. Wang, H. Y. Wu, C. J. Fu and F. W. Kang, *J. Lumin.*, 2011, 131, 676-681.
223. D. Jia, L. A. Lewis and X. J. Wang, *Electrochem Solid St.*, 2010, 13, J32-J34.
224. Y. J. Chuang, Z. P. Zhen, F. Zhang, F. Liu, J. P. Mishra, W. Tang, H. M. Chen, X. L. Huang, L. C. Wang, X. Y. Chen, J. Xie and Z. W. Pan, *Theranostics*, 2014, 4, 1112-1122.
225. D. Q. Chen, *J. Eur. Ceram. Soc.*, 2014, 34, 4069-4075.
226. D. R. Li, Y. H. Wang, K. Xu, H. Zhao and Z. F. Hu, *Rsc. Adv.*, 2015, 5, 20972-20975.
227. Y. X. Zhuang, J. Ueda and S. Tanabe, *J. Mater. Chem. C*, 2013, 1, 7849-7855.
228. A. Bessiere, S. Jacquart, K. Priolkar, A. Lecointre, B. Viana and D. Gourier, *Opt. Express*, 2011, 19, 10131-10137.
229. C. Y. Liu, Z. G. Xia, M. S. Molokeev and Q. L. Liu, *J. Am. Ceram. Soc.*, 2015, 98, 1870-1876.
230. X. Q. Xu, J. Ren, G. R. Chen, D. S. Kong, C. J. Gu, C. M. Chen and L. R. Kong, *Opt. Mater. Express*, 2013, 3, 1727-1732.
231. Y. X. Zhuang, J. Ueda and S. Tanabe, *Opt. Mater. Express*, 2012, 2, 1378-1383.
232. R. Pang, C. Y. Li, L. L. Shi and Q. Su, *J. Phys. Chem. Solids*, 2009, 70, 303-306.
233. R. Pang, C. Y. Li, S. Zhang and Q. Su, *Mater. Chem. Phys.*, 2009, 113, 215-218.
234. G. F. Ju, Y. H. Hu, L. Chen, X. J. Wang and L. H. Hung, *Appl. Phys. A-Mater.*, 2014, 114, 867-874.
235. G. F. Ju, Y. H. Hu, L. Chen, X. J. Wang and Z. F. Mu, *Opt. Mater.*, 2014, 36, 1183-1188.
236. K. Li, M. M. Shang, Y. Zhang, J. Fan, H. Z. Lian and J. Lin, *J. Mater. Chem. C*, 2015, 3, 7096-7104.
237. X. G. Wang, F. P. Du, D. L. Wei, Y. L. Huang and H. J. Seo, *Sensor. Actuat. B-Chem.*, 2011, 158, 171-175.
238. Z. R. Liu and R. X. Zhong, *J. Alloy. Compd.*, 2013, 556, 6-11.
239. G. B. Che, C. B. Liu, Q. W. Wang and Z. L. Xu, *Chem. Lett.*, 2008, 37, 136-137.
240. Y. H. Jin, Y. H. Hu, L. Chen, Y. R. Fu, Z. F. Mu, T. Wang and J. Lin, *J. Alloy. Compd.*, 2014, 616, 159-165.
241. Y. Takahashi, M. Ando, R. Ihara and T. Fujiwara, *Opt. Mater. Express*, 2011, 1, 372-378.
242. G. B. Che, X. Y. Li, C. B. Liu, H. Wang, Y. Liu and Z. L. Xu, *Phys. Status. Solidi. A*, 2008, 205, 194-198.
243. Y. X. Zhuang, Y. Katayama, J. Ueda and S. Tanabe, *Opt. Mater.*, 2014, 36, 1907-1912.
244. G. B. Che, C. B. Liu, X. Y. Li, Z. L. Xu, Y. Liu and H. Wang, *J. Phys. Chem. Solids*, 2008, 69, 2091-2095.
245. L. Zhang, X. F. Cao, X. T. Chen and Z. L. Xue, *J. Colloid. Interf. Sci.*, 2011, 354, 630-636.
246. Z. H. Ju, R. P. Wei, J. R. Zheng, X. P. Gao, S. H. Zhang and W. S. Liu, *Appl. Phys. Lett.*, 2011, 98, 1906.
247. B. F. Lei, S. Q. Man, Y. L. Du and S. Yue, *Mater. Chem. Phys.*, 2010, 124, 912-915.
248. Z. W. Liu and Y. L. Liu, *Mater. Chem. Phys.*, 2005, 93, 129-132.
249. Y. H. Jin, Y. H. Hu, L. Chen, X. J. Wang, G. F. Ju and Z. F. Mu, *J. Lumin.*, 2013, 138, 83-88.
250. Y. H. Jin, Y. H. Hu, L. Chen, X. J. Wang and G. F. Ju, *Opt. Mater.*, 2013, 35, 1378-1384.
251. T. Nakamura, M. Shima, M. Yasukawa and K. Ueda, *J. Sol-Gel. Sci. Techn.*, 2012, 61, 362-366.
252. X. P. Gao, Z. Y. Zhang, C. Wang, J. Xu, Z. H. Ju, Y. Q. An and W. S. Liu, *J. Electrochem. Soc.*, 2011, 158, J405-J408.
253. S. Kamimura, C. N. Xu, H. Yamada, N. Terasaki and M. Fujihala, *Jpn. J. Appl. Phys.*, 2014, 53.
254. J. C. Zhang, Q. S. Qin, M. H. Yu, M. J. Zhou and Y. H. Wang, *J. Lumin.*, 2012, 132, 23-26.
255. J. C. Zhang, M. H. Yu, Q. S. Qin, H. L. Zhou, M. J. Zhou, X. H. Xu and Y. H. Wang, *J. Appl. Phys.*, 2010, 108.
256. B. F. Lei, B. Li, X. J. Wang and W. Li, *J. Lumin.*, 2006, 118, 173-178.
257. X. X. Qin, Y. Li, D. K. Wu, Y. L. Wu, R. C. Chen, Z. J. Ma, S. J. Liu and J. R. Qiu, *Rsc. Adv.*, 2015, 5, 101347-101352.
258. M. M. Shi, D. Y. Zhang and C. K. Chang, *J. Alloy. Compd.*, 2015, 639, 168-172.
259. Y. H. Jin, Y. H. Hu, L. Chen, X. J. Wang, G. F. Ju and Z. F. Mou, *J. Am. Ceram. Soc.*, 2013, 96, 3821-3827.
260. L. L. Noto, S. S. Pitale, M. A. Gusowki, J. J. Terblans, O. M. Ntwaeaborwa and H. C. Swart, *Powder. Technol.*, 2013, 237, 141-146.

261. P. Boutinaud, L. Sarakha and R. Mahiou, *J. Phys-Condens. Mat.*, 2009, 21, 025901 (1)-(6).
262. Y. H. Jin, Y. H. Hu, L. Chen, X. J. Wang, G. F. Ju and Z. F. Mu, *Radiat. Meas.*, 2013, 51-52, 18-24.
263. Y. G. Su, L. P. Li and G. S. Li, *Chem. Mater.*, 2008, 20, 6060-6067.
264. X. G. Zhang, L. Y. Zhou and M. L. Gong, *Luminescence*, 2014, 29, 104-108.
265. L. Wu, X. L. Chen, H. Li, M. He, Y. P. Xu and X. Z. Li, *Inorg. Chem.*, 2005, 44, 6409-6414.
266. Z. M. Shao, S. Saitzek, P. Roussel and R. Desfeux, *J. Mater. Chem.*, 2012, 22, 24894-24901.
267. M. Kubus, A. M. Klonkowski, A. Lotnyk and L. Kienle, *Mater. Chem. Phys.*, 2015, 149, 424-429.
268. F. W. Kang and M. Y. Peng, *Dalton. T.*, 2014, 43, 277-284.
269. X. L. Ma, J. C. Zhang, H. H. Li, B. C. Duan, L. N. Guo, M. D. Que and Y. H. Wang, *J. Alloy. Compd.*, 2013, 580, 564-569.
270. L. L. Noto, M. L. Chitambo, O. M. Ntwaeaborwa and H. C. Swart, *Powder. Technol.*, 2013, 247, 147-150.
271. C. E. Cui, G. W. Jiang, P. Huang, L. Wang and D. Liu, *J. Lumin.*, 2014, 145, 665-668.
272. T. Hang, Q. Liu, D. L. Mao and C. K. Chang, *Mater. Chem. Phys.*, 2008, 107, 142-147.
273. G. D. Liu, Q. H. Zhang, H. Z. Wang and Y. G. Li, *Mater. Sci. Eng. B-Adv*, 2012, 177, 316-320.
274. P. Huang, X. Q. He, C. Cui and L. Wang, *Ceram. Int.*, 2014, 40, 2663-2668.
275. B. F. Lei, Y. L. Liu, G. B. Tang, Z. R. Ye and C. S. Shib, *Electrochem Solid St.*, 2004, 7, G225-G227.
276. Y. M. Yang, X. D. Li, X. Y. Su, Z. Q. Li, L. L. Liu, Y. Z. Liu, J. Zhang, C. Mi and F. Yu, *Opt. Mater.*, 2014, 36, 1822-1825.
277. J. W. Zhang, Y. L. Liu, J. X. Zhang, D. S. Yuan, J. H. Rong and L. H. Huang, *Rare. Metal. Mat. Eng.*, 2006, 35, 766-769.
278. L. X. Wang, L. Zhang, Y. D. Huang, D. Z. Jia and J. J. Lu, *J. Lumin.*, 2009, 129, 1032-1035.
279. H. R. Zhang, B. F. Lei, J. L. Qin, J. F. Li, Y. L. Liu, X. T. Liu, M. T. Zheng, Y. Xiao and H. W. Dong, *J. Am. Ceram. Soc.*, 2013, 96, 1810-1814.
280. J. L. Qin, H. R. Zhang, B. F. Lei, C. F. Hu, J. F. Li, Y. L. Liu, J. X. Meng, J. Wang, M. T. Zheng and Y. Xiao, *J. Am. Ceram. Soc.*, 2013, 96, 3149-3154.
281. H. R. Zhang, M. T. Zheng, B. F. Lei, Y. Xiao, H. W. Dong, Y. L. Liu, X. T. Liu, J. J. Deng, J. W. Deng and Z. L. Huang, *Ecs Solid State Lett.*, 2013, 2, R16-R18.
282. P. F. Smet, J. Botterman, K. Van den Eeckhout, K. Korthout and D. Poelman, *Opt. Mater.*, 2014, 36, 1913-1919.
283. J. Wang, H. R. Zhang, B. F. Lei, H. W. Dong, H. M. Zhang, Y. L. Liu, N. L. Lai, Y. Fang and Z. J. Chen, *Opt. Mater.*, 2014, 36, 1855-1858.
284. H. R. Zhang, M. T. Zheng, B. F. Lei, Y. L. Liu, Y. Xiao, H. W. Dong, Y. C. Zhang and S. P. Ye, *Ecs J. Solid State Sc.*, 2013, 2, R117-R120.
285. Y. R. Tang, H. J. Song, Y. Y. Su and Y. Lv, *Anal. Chem.*, 2013, 85, 11876-11884.
286. C. Q. Wu, J. C. Zhang, P. F. Feng, Y. M. Duan, Z. Y. Zhang and Y. H. Wang, *J. Lumin.*, 2014, 147, 229-234.
287. G. F. Ju, Y. H. Hu, L. Chen and X. J. Wang, *J. Appl. Phys.*, 2012, 111.
288. B. F. Lei, L. Sha, H. R. Zhang, Y. L. Liu, S. Q. Man and S. Yue, *Solid State Sci*, 2010, 12, 2177-2181.
289. Y. H. Jin, Y. H. Hu, L. Chen and X. J. Wang, *J. Am. Ceram. Soc.*, 2014, 97, 2573-2579.
290. C. Cao, S. L. Guo, B. K. Moon, B. C. Choi and J. H. Jeong, *Mater. Chem. Phys.*, 2013, 139, 609-615.
291. X. M. Zhang, N. Choi, K. Park and J. Kim, *Solid State Commun*, 2009, 149, 1017-1020.
292. L. X. Ning, C. C. Zhou, W. P. Chen, Y. C. Huang, C. K. Duan, P. Dorenbos, Y. Tao and H. B. Liang, *J. Phys. Chem. C*, 2015, 119, 6785-6792.
293. F. Wang, B. Yang, D. C. Liu, W. H. Ma, X. M. Chen and Y. N. Dai, *Spectrochim. Acta. A*, 2014, 126, 46-52.
294. H. Y. Wu, Y. H. Hu, L. Chen and X. J. Wang, *Acta. Phys-Chim. Sin.*, 2011, 27, 1201-1206.
295. H. Suo, C. F. Guo, Z. Yang, S. S. Zhou, C. K. Duan and M. Yin, *J. Mater. Chem. C*, 2015, 3, 7379-7385.
296. Y. M. Yang, Z. Q. Li, Z. Q. Li, F. Y. Jiao, X. Y. Su and D. Y. Ge, *J. Alloy. Compd.*, 2013, 577, 170-173.
297. Y. H. Jin, Y. H. Hu, L. Chen, X. J. Wang, G. F. Ju, Z. F. Mou and F. Liang, *Opt. Commun.*, 2014, 311, 266-269.
298. B. Liu, C. S. Shi and Z. M. Qi, *J. Phys. Chem. Solids*, 2006, 67, 1674-1677.
299. V. Caratto, F. Locardi, G. A. Costa, R. Masini, M. Fasoli, L. Panzeri, M. Martini, E. Bottinelli, E. Gianotti and I. Miletto, *Acs Appl. Mater. Inter.*, 2014, 6, 17346-17351.
300. M. Lastusaari, H. Jungner, A. Kotlov, T. Laamanen, L. C. V. Rodrigues, H. F. Brito and J. Holsa, *Z. Naturforsch. B*, 2014, 69, 171-182.
301. P. Huang, F. Yang, C. E. Cui, L. Wang and X. Lei, *Ceram. Int.*, 2013, 39, 5615-5621.

302. L. Ma, X. J. Zou, B. Bui, W. Chen, K. H. Song and T. Solberg, *Appl. Phys. Lett.*, 2014, 105.
303. S. Y. Kaya, E. Karacaoglu and B. Karasu, *Ceram. Int.*, 2012, 38, 3701-3706.
304. P. C. Ricci, C. M. Carbonaro, D. Chiriu and A. Anedda, *J. Mater. Chem.*, 2011, 21, 18425-18430.
305. H. J. Guo, W. B. Chen, W. Zeng, G. Li, Y. H. Wang, Y. Y. Li, Y. Li and X. Ding, *J. Mater. Chem. C*, 2015, 3, 5844-5850.
306. F. Luo, G. M. Sun, A. M. Zheng, S. X. Lian, Y. L. Liu, X. F. Feng and Y. Y. Chu, *Dalton. T.*, 2012, 41, 13280-13283.
307. Y. Tsukasaki, M. Morimatsu, G. Nishimura, T. Sakata, H. Yasuda, A. Komatsuzaki, T. M. Watanabe and T. Jin, *Rsc. Adv.*, 2014, 4, 41164-41171.
308. A. M. Smith, M. C. Mancini and S. M. Nie, *Nat. Nanotechnol*, 2009, 4, 710-711.
309. G. S. Hong, S. O. Diao, A. L. Antaris and H. J. Dai, *Chem. Rev.*, 2015, 115, 10816-10906.
310. B. Zhang, J. Yang, Y. P. Zou, M. Gong, H. Chen, G. S. Hong, A. L. Antaris, X. Y. Li, C. L. Liu, C. X. Chen and H. J. Dai, *Chem. Sci.*, 2014, 5, 4070-4075.
311. J. Y. Niu, X. Wang, J. Z. Lv, Y. Li and B. Tang, *Trac-Trend Anal. Chem.*, 2014, 58, 112-119.
312. H. H. Li and Y. H. Wang, *Res. Chem. Intermediat.*, 2010, 36, 51-59.
313. H. H. Li, S. Yin, Y. H. Wang, M. Kobayashi, S. Tezuka, M. Kakihana and T. Sato, *Res. Chem. Intermediat.*, 2013, 39, 1615-1621.
314. H. H. Li, S. Yin, Y. H. Wang, T. Sekino, S. W. Lee and T. Sato, *J Catal.*, 2013, 297, 65-69.
315. H. H. Li, S. Yin, Y. H. Wang and T. Sato, *Appl. Catal. B-Environ.*, 2013, 132, 487-492.
316. H. H. Li, S. Yin, Y. H. Wang and T. Sato, *Environ. Sci. Technol.*, 2012, 46, 7741-7745.
317. H. C. Sun, L. K. Pan, X. Q. Piao and Z. Sun, *J. Colloid. Interf. Sci.*, 2014, 416, 81-85.
318. C. B. Wang, T. T. Xuan, J. Q. Liu, H. L. Li and Z. Sun, *Int. J. Appl. Ceram. Tec.*, 2015, 12, 722-727.